Purification of Graphite Concentrate by Leaching with Phosphorus Chemistry

Hak Jun Oh
Department of Mining and Materials Engineering, McGill University, Montreal

July, 2022

A thesis submitted to McGill University in partial fulfillment of the requirements of the degree of Masters of Science.

Abstract

Graphite is a common anode material for electric vehicle lithium-ion batteries (EV LIBs). Among the types of graphite, flake graphite is a suitable feedstock for EV LIB anode production due to its abundant reserves and high graphitization degree. EV LIB production requires eleven times the mass of graphite than lithium, and high purity flake graphite is required for anode production. Raw flake graphite can be concentrated by flotation up to 95%, but further removal of impurities, such as iron sulphide and silicate, by thermal and/or chemical-processing is required for electrical applications.

Phosphoric acid is an unconventional lixiviant, as hydrofluoric acid, sulfuric acid, and hydrochloric acid are more common graphite impurity leaching agents. Design of experiment was applied to evaluate and optimize atmospheric pressure leaching with phosphoric acid ([1 – 5] M), condensed sodium phosphate ([0 – 250] g $NaPO_3$/L), leaching times ([60 – 300] min), liquid to solid ratios ([3:1 – 7:1] mL:g), and temperatures ([RT – 100] $^{\circ}$C), as well as the interaction between the factors, on impurity removal efficiency.

The impurity leaching efficiency was evaluated with X-ray diffraction (XRD), energy dispersive spectroscopy (EDS), and scanning electron microscopy (SEM). Microwave plasma atomic emission spectroscopy (MP-AES) was used to measure dissolved silicate as silicon, aluminum, potassium, calcium, and iron in the pregnant leach solutions. Kaolinite, muscovite, and illite were identified as major aluminosilicate impurities. Dissolution mechanisms for natural kaolinite were studied with nuclear magnetic resonance. Kaolinite dissolution is proposed to be a combination of ligand exchange between protonated hydroxyl groups associated with aluminum and phosphorus compounds. Aluminum dissolves via chelation by phosphorus compounds and silicates dissolve via proton-assisted dissolution. Using two different leaching steps that targeted aluminum, then silicon, dissolution at 100 °C leached 100% Fe after the first leaching stage, and a total of 85 ± 5.5% Al %, and 38 ± 14% Si after both stages.

Résumé

Le graphite est un matériau d'anode courant pour les batteries lithium-ion des véhicules électriques (BLI VE). Parmi les types de graphite, le graphite en flocons est une matière première appropriée pour la production d'anodes BLI VE en raison de ses réserves abondantes et de son degré de graphitisation élevé. La production de BLI VE nécessite 11 fois plus de graphite que le lithium, et du graphite en flocons de haute pureté est nécessaire pour la production d'anodes. Le graphite en flocons brut peut être concentré par flottation jusqu'à 95 %, mais une élimination supplémentaire des impuretés, telles que le sulfure de fer et le silicate, par thermo/hydrotraitement est nécessaire pour les applications électriques.

L'acide phosphorique est un lixiviant non conventionnel, car l'acide fluorhydrique, l'acide sulfurique et l'acide chlorhydrique sont des agents de lixiviation des impuretés de graphite plus courants. La conception de l'expérience (Design of Experiments, DOE) a été appliquée pour évaluer et optimiser l'effet des concentrations d'acide phosphorique ([1 – 5] M), phosphate condensé ([0 – 250] g $NaPO_3$/L), du temps de lixiviation ([60 – 300] min), du rapport liquide sur solide ([3:1 – 7:1] mL:g), et de la température ([RT – 100] $^{\circ}$C), ainsi que de l'interaction entre les facteurs, sur l'efficacité d'élimination des impuretés.

L'efficacité de la lixiviation des impuretés a été évaluée par diffraction des rayons X (XRD), spectroscopie à dispersion d'énergie (EDS) et microscopie électronique à balayage (SEM). La spectroscopie d'émission atomique à plasma micro-ondes (MP-AES) a été utilisée pour mesurer le silicate dissous sous forme de silicium, d'aluminium, de potassium, de calcium et de fer dans les solutions de lixiviation. La kaolinite, la muscovite et l'illite ont été identifiées comme les principales impuretés d'aluminosilicate. Les mécanismes de dissolution de la kaolinite naturelle ont été étudiés par résonance magnétique nucléaire. La dissolution de la kaolinite est proposée comme étant une combinaison d'échange de ligands entre les groupes hydroxyles protonés associés aux composés d'aluminium et les composés de phosphore. L'aluminium se dissout par chélation par des composés phosphorés et les silicates se dissolvent par dissolution assistée par protons. En utilisant deux étapes de lixivation différentes ciblant l'auminium, puis le silicium, la dissolution à 100 °C lessivé 100% Fe après une étape, 85 ± 5.5% Al %, and 38 ± 14% Si après les deux étapes.

Acknowledgements

This thesis would not have been possible without the support of my family and friends, who were always there to listen to my adventures in the lab. I would like to present my gratitude to my two dogs, Bingo and Manel, for their unconditional love.

I am very grateful to have meet Tian Zhao and Bailee Johnson who supported me on numerous occasions throughout my graduate study.

I would like to thank Lori Manoukian for being a great lab buddy and providing mental support throughout my study during COVID pandemic.

I would also acknowledge the skills from Aleksandra Djuric for training in the Analytical laboratory and her insight on acid digestion.

I am sincerely lucky to have met Ozan Kökkılıç who introduced me to invaluable DoE skill. It's a skillset that I shall never forget, and I will forever thank Ozan for enlightening me with such asset. I would also like to thank other people that I met on the 2nd floor of Wong building.

I am truly blessed and grateful to have met my supervisor Dr. Sidney Omelon who supported me and my project unconditionally throughout my graduate study. Without your enthusiasm for science and knowledge, my experience as a master's student would not have been the same. I would also like to express my gratitude for your supports, despite the slow environment caused by COVID pandemic and numerous deadlines. Thank you for being my supervisor.

I would like to acknowledge NSERC and SRG Graphite for their financial support.

Table of Contents

Table of Figures

Table of Tables

1 Graphite & Its State-of-the-Art Purification Techniques

This introduction to graphite explains its uses, and by extension, its markets. The trends in the graphite market explain the current interest in its concentration and purification (beneficiation) processes for these expanding graphite uses. Commercial graphite is characterized and valued according to its flake size and grade. Physical and chemical graphite beneficiation processes are explored in the following chapters to improve grade while minimizing flake size. Phosphoric acid is proposed as a novel lixiviant for graphite purification and is its potential is explored in this thesis.

Table 1-1. Author Statement

Conceptualization. Writing (Review & Editing)	Hak Jun Oh Associate Professor Sidney Omelon
Investigation, Writing (Original Draft)	Hak Jun Oh
Writing – Review & Editing	Hak Jun Oh Associate Professor Sidney Omelon

1.1 Graphite Description & Market Trend

Graphite is a naturally occurring allotrope of crystalline carbon, which is composed of coplanar sheets of carbon atoms (Figure 1-1) [1, 2].

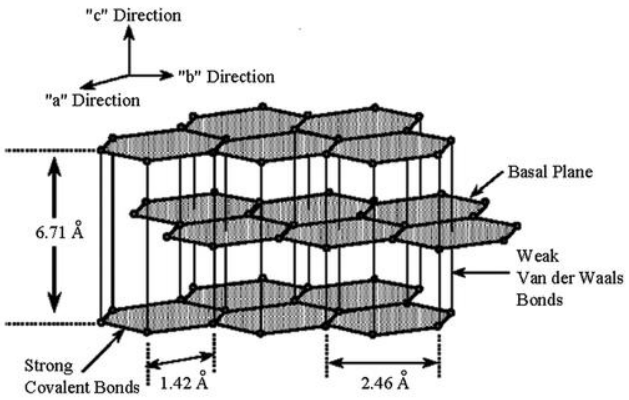

Figure 1-1. Schematic of the crystalline graphite structure [3]

Natural graphite is categorized into three forms based on shape, size, grade, and crystallinity. Graphite is categorized as: flake, vein (lump), and amorphous [1, 4]. Flake graphite is defined by its flat, plate-like crystals, with angular or irregular edges. Flake and vein graphite are in the "macro-graphite" family, which is further subcategorized by size. Flake graphite exists as coarse

(> 150 μm) and fine (< 150 μm) flakes, whereas vein graphite is defined by its larger size (> 4 cm) [5]. So-called amorphous graphite, also known as microcrystalline graphite, is in the "micro-graphite" family that is defined by its relatively smaller crystal size (< 70 μm) [1].

Graphite is formed by the metamorphic conversion of organic matter in sediments [1]. The four different graphite formation processes are: regional metamorphism, coal seam metamorphism, hydrothermal vein-type graphite, and tiny-particle graphite in igneous settings [2]. Flake graphite is usually hosted in quartz-mica schist, feldspathic or micaceous quartzite, and gneiss [1]. Impurities often include minerals that are commonly found in metasediments. These impurities include quartz, feldspar, mica, amphibole, garnet, calcite, pyrrhotite, pyrite, and magnetite [1]. Vein graphite is commonly disseminated in igneous and metamorphic rocks, and is found as less common aggregates of coarse and/or microcrystalline platy or acicular (needle-shaped) graphite [1]. Amorphous graphite, commonly found in quartzites and conglomerates, is composed of clusters of fine graphite crystals that provide the characteristics of softness and earthiness [1].

Graphite has a hardness of 0.5-1 on the Mohs scale, and its density ranges between 2.09 – 2.26 g/cm^3 [1]. It decomposes at 600 $^\circ$C in oxidizing conditions, and melts at 3,550 $^\circ$C in non-oxidizing conditions. The vaporization of the carbonaceous material occurs at 4,500°C. Graphite has good thermal and electrical conductivity, chemical inertness, greasy texture, hydrophobicity due to adsorption of hydrocarbon, and low thermal expansion [1, 5, 6]. The properties of graphite are presented in Table 1-2.

Table 1-2. Properties of the element carbon adapted from [7]

Name:	Carbon
Symbol:	C
Atomic Number:	6
Atomic Mass:	12.0107 amu
Number of protons/electrons:	6
Number of neutrons:	6, 7, 8
Classification:	Non-metal
Crystal structure:	Hexagonal, Cubic
Density @ 293K	Graphite - 2.26 g/cm^3
Color:	Black, gray

1.2 Graphite Markets & Trends

Graphite has shown its practicality in a wide range of applications such as anodic material for energy storage in lithium ion batteries, refractory, and others (Figure 1-2) [4].

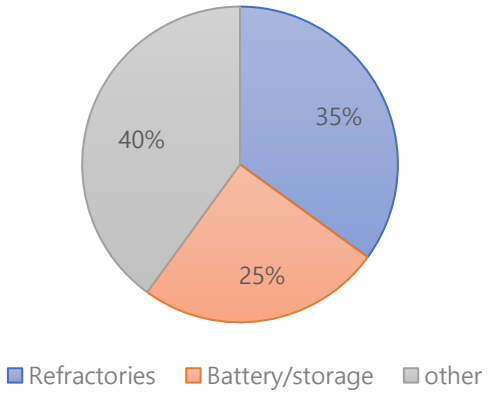

Figure 1-2. Common applications of graphite adapted from [4]

The market demand for graphite is growing as an upward trend was reported for global graphite consumption [1, 2].

Vein graphite has the highest crystallinity and purity of all the graphite forms. Vein graphite occurrences are rare; it is mined only in Sri Lanka [2]. Therefore, it is more practical to produce graphite products from flake graphite or amorphous graphite. Flake graphite accounts for 49 % of the total natural graphite market [2]. The most abundant form of natural graphite is amorphous graphite, which contains 20 – 40% in graphite content before refining [2]. For energy storage applications, the graphite purity needs to be above 99.5% with a d_{002} spacing near 0.3354 nm (d_{002} of ideal graphite) [8, 9]. The d_{002} spacing is important to estimate the graphitization degree of the carbon material [10].

Amorphous graphite is expected to substitute flake graphite for lithium ion battery anode fabrication, as its characteristic microcrystalline structure mitigates the deformation energy during battery cycling. This structural stability through cyclic battery use results in improved battery performance and life [11]. The amorphous graphite performance as an lithium ion battery anode has sparked the interest of the mining industry; the demand for high-purity microcrystalline graphite is projected to be driven even higher in the future [12]. Though to meet the industry standard for graphite quality that requires coarse (> 200 µm) and pure (> 98 wt% carbon) graphite,

amorphous graphite requires further purification to qualify for high performance applications such as battery anodes [13].

1.3 Graphite Beneficiation Techniques

Graphite purity is defined by the carbon content. A common method to determine the carbon content is by ash analysis [1, 5, 14, 15]. The ASTM standard for graphite ash analysis is C561-16 [16]. Ash analysis reports the noncombustible, elemental ash composition. The ash composition indicates the impurity types for graphite purification. The carbon content, or fixed carbon content, is the percentage of organic matter in a given organic mass without the noncombustible and volatile contents [1, 5, 14, 15].

In the following sections, current physical and chemical natural graphite purification techniques are overviewed.

1.4 Common Graphite Impurities

Graphite impurities have been reported to be located between the graphite layers, in stacks, or clusters during graphite mineral formation [4, 17]. Scanning electron microscopy (SEM) analysis conducted by Kim et al. identified and classified four different inclusion states or "Types" of impurities in the graphite (Figure 1-3) [17]. This study focused on expanding the graphite structure with a strong oxidizer (HNO_3) and heat to study the impurities in the graphite.

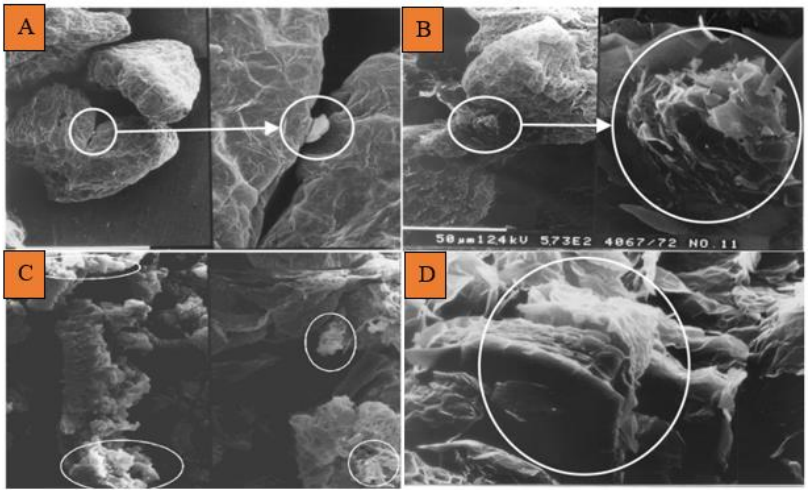

Figure 1-3. Four different inclusion cases of impurities in the graphite. A) Type 1: simply held between graphite clusters. B) Type 2: simply lying between clusters and strongly bound to surfaces. C) Type 3: adhering and tangling strongly and widely onto cluster surfaces. D) Type 4: sandwiched between the stacks within a cluster [17]

According to energy-dispersive x-ray analysis (EDXA), impurity Types 2 – 4 includes typical clay minerals containing Si, Al, Fe, Mg, Ca, and Na [17]. It is likely that they coalesced during graphite formation. The effect of these impurities on graphite crystallinity depends on their degree of dissemination. Impurity Types 1 and 2 have been observed to have more crystalline structures than Types 3 and 4 [17].

1.5 Mineral Beneficiation

Graphite purity can be increased via physical methods to segregate and separate impurities, and/or chemical methods to dissolve and remove impurities [4]. The physical methods commonly consist of reducing the graphite ore particle size by grinding. The smaller particles, with the expectation that some particles will contain less impurities than other particles, are then separated by flotation. Flotation uses small rising air bubbles to separate more hydrophobic, graphite-rich particles, which bind to rising air bubbles, from particles with a higher impurity content that are more dense and less hydrophobic.

Mechanical beneficiation methods require careful assessments and procedures to reduce or avoid adversely changing the graphite structure or size, or the purified graphite recovery rate. The graphite value directly correlates to the graphite size, hence larger graphite size is always preferred from the economical standpoint [1].

Grinding graphite can uniquely cover impurity particle surfaces with soft graphite, in the same way that a graphite pencil easily leaves a dark mark on paper. This characteristic is due to the weak van der Waals force that binds graphite layers and is susceptible to failure at low shearing forces [1, 13, 18]. Flotation selectivity can be reduced by the formation of a thin layer of smeared graphite on gangue (impurity) materials – this increases the hydrophobicity of gangue minerals, and causes them to float with the more pure graphite particles [18]. This unique characteristic adversely affects purified graphite recovery, and consequently, the flotation method selectivity efficiency. Consequently, the physically achievable maximum carbon content in the graphite concentrate was reported to be in the range of 90-95% [1, 3, 12, 15, 18, 19]. Given this limitation, chemical beneficiation is required to achieve a higher degree of graphite purity.

1.6 Chemical Beneficiation

Chemical purification is a commonly employed technique to further increase the degree of graphite purity after mineral beneficiation/processing [1, 12, 20].

1.6.1 Leaching Impurities from Concentrated Graphite

Selective leaching is the process of exposing minerals to a lixiviant (an aqueous solution that may be acidic or basic, reducing or oxidizing) that selectively leaches out desired or undesired ore components. Graphite leaching targets the dissolution of impurities with acids, such as hydrochloric acid (HCl), sulfuric acid (H_2SO_4), nitric acid (HNO_3), fluoric acid (HF), or a combination of these acids, or alkaline (NaOH) solutions [2, 4]. After the target minerals dissolve in the lixiviant, it is called a "pregnant leach solution" (PLS). The soluble compounds in the PLS can be removed by increasing the solution pH with alkaline chemical addition to neutralize and form insoluble precipitates [2].

Acid leaching of natural graphite impurities is common due to its low-investment requirement, high accessibility, and broad spectrum of applications [2]. Acid leaching is commonly applied to impurity minerals with increased solubility with decreased pH. Silicate and sulphide impurities do not dissolve in acidic conditions. Alkali roasting and alkali leaching are required to dissolve the sulfides and silicates from graphite concentrates [4]. Depending on the targeted gangue material, these processes can be the only process, or be paired with acid leaching to yield a higher graphite purity [4].

1.6.1.1 Hydrofluoric Acid Leaching

Hydrofluoric acid (HF) is reported as an effective lixiviant for the unique acidic dissolution of silica and other inorganic impurities in graphite ore [2, 4, 14]. Some of the proposed silica dissolution reactions are described in Eq.1 and 2 [14]:

$$4HF + 2SiO_2 \rightarrow SiF_4 + 2H_2O \quad (1)$$

$$SiF_4 + 2HF \rightarrow H_2SiF_6 \quad (2)$$

Although useful for its ability to dissolve inorganic metal oxides and silicates, HF is not a sustainable choice for worker safety, and complicates the graphite purification process. Concentrated HF exposure can cause extensive dermal burns upon physical contact and seriously damage the respiratory system when the HF vapor is inhaled [21]. HF lixiviants can form water-

insoluble fluoride compounds, such as calcium fluoride (CaF_2), through the dissolution of calcite or gypsum. Dissolving calcium and other insoluble fluorides requires a supplementary leaching step with sulfuric acid [14, 22, 23]. HF is reported to be ineffective for pyrite dissolution, while pyrite is a common impurity in graphite ores [22, 24].

To achieve both sustainability and efficacy in the leaching process, some research has explored the alternatives to minimize the use of HF and to deviate from using solely one type of acid. To avoid HF use, silicates can be removed by sulfuric, hydrochloric, or mixed acid leaching. Acid leaching preceded by an alkali roasting pre-treatment improves the impurity leaching performance of acids other than HF [20, 22, 25].

1.6.1.2 Sulfuric Acid Leaching

Sulfuric acid (H_2SO_4) is a low-risk candidate lixiviant for graphite leaching. From an economic standpoint, the choice of H_2SO_4 as a lixiviant is undeniably advantageous owing to its low cost, and its wide use as a lixiviant in extractive metallurgical processes [5, 25]. Researchers have generated a significant graphic purification literature that compares H_2SO_4 leaching to HCl leaching.

1.6.1.3 Hydrochloric Acid Leaching

Hydrochloric acid (HCl) differs from sulfuric acid both in its materials compatibility and its higher vapour pressure. HCl has been investigated for its graphite purification potential.. HCl is known to react with hydroxide compounds to form chloride compounds that remain soluble in solution [12]. Various reactions between inorganic solids, and hydrochloric acid are shown in Eqs.3 - 10 [12, 14, 22]:

$$CaO_{(s)} + 2HCl_{(aq)} \rightarrow CaCl_{2(aq)} + H_2O_{(l)} \quad (3)$$

$$CaSO_4 \cdot 2H_2O_{(s)} + 2HCl_{(aq)} \rightarrow CaCl_{2(aq)} + H_2SO_{4(aq)} + 2H_2O_{(l)} \quad (4)$$

$$CaCO_{3(s)} + 2HCl_{(aq)} \rightarrow CaCl_{2(aq)} + CO_{2(g)} + H_2O_{(l)} \quad (5)$$

$$MgO_{(s)} + 2HCl_{(aq)} \rightarrow MgCl_{2(aq)} + H_2O_{(l)} \quad (6)$$

$$Fe_2O_{3(s)} + 6HCl_{(aq)} \rightarrow 2FeCl_{3(aq)} + 3H_2O_{(l)} \quad (7)$$

$$Fe(OH)_{3(s)} + 3HCl_{(aq)} \rightarrow FeCl_{3(aq)} + 3H_2O_{(l)} \quad (8)$$

$$FeS_{(s)} + 2HCl_{(aq)} \rightarrow FeCl_{2(aq)} + H_2S_{(l)} \quad (9)$$

$$Al(OH)_{3(s)} + 3HCl_{(aq)} \rightarrow AlCl_{3(aq)} + 3H_2O_{(l)} \quad (10)$$

The carbon content increased as the concentration of HCl was increased up to 0.75 mol/L HCl. At higher concentrations, the carbon content in the leached graphite sample was not significantly increased [3, 12]. A comparative study was conducted for leaching with H_2SO_4 or HCl; the results showed an insignificant difference [25]. However, Kaya and Canbazoğlu demonstrated that HCl outperformed H_2SO_4 with an increase in acid concentration. This difference was correlated to the superior reactivity of HCl in dissolving clay-group gangue materials, such as kaolinite ($Al_4(Si_4O_{10})(OH)_8$) and muscovite ($KAl_2(AlSi_3O_{10})(OH)_2$) [22]. Despite this result, it is suggested that a higher HCl concentration does not necessarily guarantee a greater graphite purity, due to a higher dissolution of organic materials and the formation of insoluble compounds [26]. Moreover, Xu et al. suggested that a longer leaching time is detrimental to the leaching process, as leached ions can potentially re-absorb onto graphite [27].

In practice, HCl is combined with other types of acid and an alkali roasting method to further enhance the carbon content [12, 14, 20]. Acid-leaching with HCl followed by an alkali roasting was studied by Wang et al.; they reported successful removal of impurities that existed as hydroxide compounds [12].

1.6.1.4 Alkali Roasting As a Pretreatment to Leaching

Alkali roasting is reported to leach silicate and sulfide impurities effectively [12, 20]. It is commonly conducted between 500 – 900 °C, with sodium hydroxide [20]. Sodium hydroxide is preferred over calcium-containing alkaline compounds to avoid the formation of insoluble calcium silicate [28].

Alkaline roasting improves the effectiveness of acid leaching, dissolving a wide spectrum of natural graphite impurities [12, 14, 20]. Heating an alkaline slurry of concentrated graphite causes silicates and oxides, such as SiO_2, Al_2O_3, Fe, CaO, and MgO, to transition from an ordered structure to a disordered structure. This disordered structure has a higher activity [12]. This results in gangue products that more susceptible to react with acids, leading to the dissolution of gangue minerals. Some of the possible reactions are listed in Eqs. 11 – 16 [12, 14]:

$$SiO_{2(s)} + 2NaOH_{(s)} \rightarrow Na_2SiO_{3(s)} + H_2O_{(l)} \quad (11)$$

$$Al_2O_{3(s)} + 2NaOH_{(s)} \rightarrow 2NaAlO_{2(s)} + H_2O_{(l)} \quad (12)$$

$$FeS_{(s)} + 2NaOH_{(s)} + 3O_{2(g)} \rightarrow FeO_{(s)} + Na_2SO_{4(s)} + H_2O_{(l)} \quad (13)$$

$$Fe_2O_{3(s)} + 6NaOH_{(s)} \rightarrow 2Fe(OH)_{3(s)} + 3\,Na_2O_{(s)} \quad (14)$$

$$P_2O_{5(s)} + 6NaOH_{(s)} \rightarrow 2\,Na_3PO_{4(s)} + 3\,H_2O_{(l)} \quad (15)$$

$$TiO_{2(s)} + 2NaOH_{(s)} \rightarrow Na_2TiO_{3(s)} + H_2O_{(l)} \quad (16)$$

The effects of alkali roasting pre-treatment and its parameters were investigated by Wang et al. [12]. The roasting temperature, roasting time, and mass ratio of alkali to graphite concentration were studied, with the goal of maximizing graphite purity while minimizing carbon mass loss. The author noted that lower calcination temperature and time would reduce the carbon loss caused by carbon oxidation and volatilization [12]. Followed by a pre-treatment with roasting, the graphite sample was washed with HCl to dissolve hydroxides, yielding 99% pure microcrystalline graphite [12].

An unconventional low-temperature graphite roasting method was studied by Lu *et al.* [20]. It demonstrated that the 0.6% initial sulfide impurities could be minimized to below 0.05% [20]. Moreover, the roasting temperature could be as low as 150 $^{\circ}$C, but improved leaching could be achieved between 250 – 350 $^{\circ}$C [20]. After roasting the graphite sample with NaOH, the samples were washed and leached with H_2SO_4, obtaining a final carbon content of 99.4% [20]. Alkali roasting at 300 $^{\circ}$C was reported by Jara *et al*. This lower roasting temperature was sufficient for reactions between NaOH and impurities; additional thermal energy did not improve the carbon content [5].

Rao et al. investigated the effect of quenching hot graphite ore in a NaOH solution [14]. The graphite sample was then washed and leached in dilute HCl. The result was comparable to the previously described alkali roasting processes, as the quenching process attained 98% graphite purity. Furthermore, it was suggested that the induction of thermal shock by the quenching method promoted the release of quartz impurities. Despite the positive results, the economic sustainability of the alkali quenching method is questionable due to the substantial quantity requirement of sodium hydroxide solution [14]. Moreover, the use of caustic soda, such as NaOH on a large scale has been reported to generate alkaline wastewater that requires additional treatment before releasing into the environment [29]. Therefore, further process improvements are required to leverage the use of alkaline chemicals for sustainable graphite purification.

1.6.1.5 Acid Mixtures & the Role of Oxidizing Agents HNO_3 & H_2O_2

Investigators have assessed the effect of acid mixtures and the inclusion of oxidizers during graphite or leaching. Kaya and Canbazoğlu accessed the effect of a mixed HCl and HF lixiviant. The study concluded that a lixiviant with 20% HCl and 4% HF led to the highest final total carbon content in the graphite sample [22]. This lixiviant formula successfully increased the carbon content between 17-28 % [22].

Wei *et al*. investigated the indirect use of HF by combining HCl and sodium fluoride (NaF) as the lixiviant [15]. Consequently, HF formed as the by-product of the primary reaction between HCl and NaF (Eq.17). This unique approach demonstrated effective removal of impurities including calcite and complex silicates, and some of the reactions between natural impurities and indirectly form HF are described in Eqs 18-22 [15]:

$$NaF_{(s)} + HCl_{(aq)} \rightarrow HF_{(aq)} + NaCl_{(s)} \quad (17)$$

$$2H^+ + CaCO_{3_{(s)}} \rightarrow Ca^{2+} + CO_{2_{(g)}} + H_2O_{(l)} \quad (18)$$

$$Al_2Si_2O_5(OH)_{4_{(s)}} + 12HF_{(aq)} + 2H^+ \rightarrow 2AlF_2{}^+ + 2SiF_{4_{(g)}} + 9H_2O_{(l)} \quad (19)$$

$$KAl_2(AlSi_3O_{10})(OH)_{2_{(s)}} + 12HF_{(aq)} + 10H^+ \rightarrow 3Al^{3+} + 2AlF_2{}^+ + 3SiF_{4_{(g)}} + K^+ + 12H_2O_{(l)} \quad (20)$$

$$2Na^+ + SiF_{4_{(g)}} + 2HF_{(aq)} \rightarrow H_2SiF_{6\ (s)} + 2H^+ \quad (21)$$

$$6NaF_{(s)} + 4H^+ + SiO_{2_{(s)}} \rightarrow H_2SiF_{6\ (s)} + 2H^+ \quad (22)$$

Despite the excellent impurity removal, the formation of insoluble compounds, such as Na_2SiF_6, was inevitable due HF. Therefore, multiple stages of washing were required to reduce the final solid fluoride content [15].

A mixture of unspecified concentrations of weakly oxidizing H_2SO_4 and strongly oxidizing nitric acid (HNO_3) was investigated by Kim et al. [17]. The result was an increase in the final carbon content, from 93% to 99.9% [17]. Kim explored the option of removing impurities deposited between graphite layers by expanding the graphite structure with a strong oxidizing agent and a thermal treatment. The expansion was theorized to be caused by the H_2SO_4 and HNO_3 molecules penetrating between the graphite layers, stacks, or clusters, then gasifying under high temperature, resulting in an expanded graphite lattice, as shown in Figure 1-4 [17].

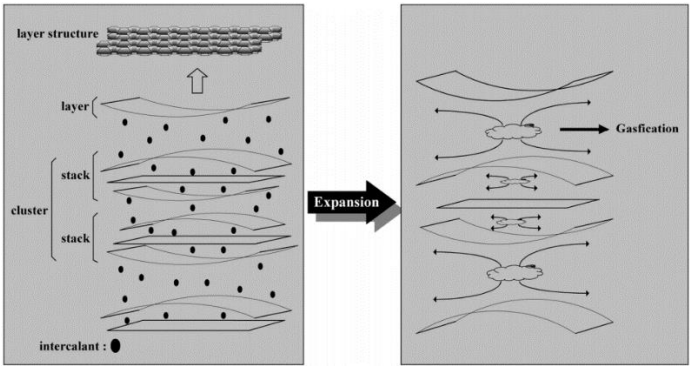

Figure 1-4. Formation of expanded graphite. Raw form (left) and expanded form (right) [17]

As a result, the leached graphite particle sizes were approximately 50 times the initial particle size [17].

This expanding crystal lattice phenomenon was also observed with hydrogen peroxide (H_2O_2) addition to the lixiviant. According to Rao, the role of H_2O_2 was crucial in the graphite exfoliation process because H_2O_2 provides highly nucleophilic ${O_2}^{2-}$ ions by reacting with OH^- ions [30].

$$NaOH \rightarrow Na^+ + OH^- \quad (23)$$

$$H_2O_2 + 2OH^- \rightarrow {O_2}^{2-} + 2H_2O \quad (24)$$

These radicals then oxidize the graphite edge planes, opening the pathway for the intercalation of HO^- ions and O_2^{2-} ions between the graphite layers [30]. The intercalated radicals then promote depolarization of the graphite layers, weakening the van der Waals forces that exist between graphite layers, and leading to graphite layer expansion [30].

Considering these studies, strongly oxidizing agents, such as HNO_3 and H_2O_2, have the potential to promote the liberation of impurities by increasing the distance between the graphite crystal lattice planes. H_2O_2 was paired with an acid in a few graphite refining studies. A three-step (acid-alkali-acid leaching) purification method studied by Jara used a mixture of H_2O_2 and H_2SO_4 in the first leaching stage of their purification process [5]. This process was deemed highly successful as the final purity was improved to 99.68%. However, the leaching capability of H_2SO_4 reduced at acid concentrations above 25% (weight % assumed). While the reaction of H_2SO_4 and silica is proposed in Eq. 25 [5],

$$SiO_{2(s)} + 2H_2SO_{4(aq)} \rightarrow 2H_2O_{(l)} + Si(SO_4)_{2(aq)} \quad (25)$$

the author noted that H_2SO_4 could be detrimental to silica impurity separation from graphite. This is because of the possible sulphate adsorption on silica surfaces, and formation of insoluble impurity complexes that are difficult to separate.

In a battery recycling study by Ma et al., H_2O_2 was tested as a graphite impurity lixiviant. A mixture of H_2SO_4 and H_2O_2 was used to purify the spent battery anode graphite [31]. The resulting graphite purity was adequate for reuse, as it was similar to the commercial-grade graphite for battery applications. The graphite sample was leached repeatedly until the impurity concentration was reduced to a desired concentration, followed by a heat treatment to restore the graphite crystalline structure. This heat treatment process is also known as "re-graphitization" [31]. The author confirmed the effectiveness of their purification methodology by underlining the insignificant change in the final morphology of graphite particles [31].

Though H_2O_2 brings advantages to leaching impurities from graphite, its usage is discouraged in some cases because of the significant expense of commercially available H_2O_2, and the high concentration requirement due to spontaneous H_2O_2 decomposition [32-34].

Various leaching methods with lixiviants composed of different acids and mixtures of acids and oxidizing agents have been overviewed in the previous sections. These methods have been summarized in Table 1-3 and Table 1-4

Table 1-3. Leaching conditions in previous graphite purification studies

Reference	Lixiviant	Liquid to solid ratio	Temp. (°C)	Reaction time (h)	Fixed carbon content treated (%)[initial %]
Wei Xie [15]	HCl (37%) + NaF (98%)	3 to 1	70	2.5	98.37 [83.08]
Hao Wang [12]	HCl (1mol/L)+ alkali roasting	30 to 1	-	-	99.0 [90.2]
Hien Tran Thi [25]	H_2SO_4 (10%C) +alkali roasting	5 to 1	20	2	98 [92.6]
Allah D. Jara [5]	H_2SO_4 (10%) + H_2O_2 (30%) + NaOH roasting (Path A) + HCl (18%) (path B) + HF (5%) (path C)	5 to 1 & 6 to 1 (w/w)	70	at least 100min (175-250min sufficient)	99.68 [94.71]
R. Bhima Rao [14]	Preheating the concentrate @500C + boiling in 12.5M NaOH solution + washing with HCl (0.88M)	-	-	-	89.3 [85]
X.J. Lu [20]	H_2SO_4 + alkali roasting	4 to 1 (w/w)	20	-	99.4 [87.7]
Byoung G. Kim [17]	H_2SO_4 + HNO_3	-	100	5.5 min	99.9 [92.9]
N. Patnaik [35]	HCl	4 to 1	40	20 min	83 [73]
O. Kaya [22]	HCl (20%), H_2SO_4 (20%), HF (4%), or HCl (20%) + HF (4%)	10 to 1 (w/v)	85	1	Variable

Table 1-4. Contents of the graphite sample before purification (expressed in wt%)

Author	C	SiO_2	Al_2O_3	Fe_2O_3	CaO	MgO	TiO_2	Na_2O	Ka_2O	MnO_2	K_2O	TFe	V	MnO	P_2O_5
Wei Xie [15]	83.08	5.95	3.39	0.44	0.4	0.3	0.043	0.26	0.41	0.0097	-	-	-	-	-
Hao Wang [12]	90.2	2.7	2.93	-	1.4	0.38	-	0.04	-	-	0.06	1.98	-	-	-
Hien Tran Thi [25]	92.6	2.44	1.53	1.08	0.25	0.27	-	-	-	-	-	-	1.26	-	-
Allah D. Jara [5]	94.71	1.35	0.45	0.25	0.02	0.09	0.01	0.01	-	-	0.01	-	-	-	-
X.J. Lu [20]	87.7	5.25	2.93	1.65	0.35	0.55	0.13	0.06	-	-	0.65	-	-	0.02	0.01
Byoung G. Kim [17]	92.9	3.4	1.5	0.78	-	0.21	0.07	-	-	-	0.28	-	-	-	-

1.6.1.6 Alkali leaching

Alkali leaching was studied by Wang et al. to overcome the disadvantages related to the alkaline roasting/acid leaching technique [3]. These are namely the risk of graphite oxidation under an uncontrolled atmospheric environment, and the high energy requirement to dry the wet graphite sample after a flotation stage, because alkali roasting requires high temperature processing. The alkali leaching process was performed in a laboratory autoclave, which served the purposed of mixing the NaOH solution and the graphite concentrate and controlled the temperature between 150-170 °C [3]. The results improved the carbon content with an increase in alkali leaching time and alkali concentration [3].

Wang et al. described the dissolution sequence of insoluble silicate minerals in alkaline conditions (Eqs. 26 - 28) [3]. The insoluble silicate minerals are first converted into soluble $(OH)_4^-$ $Al(OH)_4$, $SiO_2(OH)_3^-$, and $H_2SiO_4^{2-}$:

$$KAl_2(AlSi_3O_{10})(OH)_{2(s)} + 11OH^- + 4H_2O_{(l)} \rightarrow 3Al(OH)_4^- + K^+ + 3SiO_2(OH)_3^- \quad (26)$$

$$Al_2O_3 \cdot 2SiO_2 \cdot 2H_2O_{(s)} + 2OH^- + 5H_2O_{(l)} \rightarrow 2Al(OH)_4^- + 2H_4SiO_{4(aq)} \quad (27)$$

$$SiO_{2(s)} + 2OH^- \rightarrow 2H_2SiO_4^{2-} \quad (28)$$

The soluble silicate ions and aluminate ions react, producing insoluble hydrated sodium aluminosilicate in the form of a Na_2O-Al_2O_3-SiO_2-H_2O gel or zeolite (Eq. 29) [3].

$$8Na^+ + 6Al(OH)_4^- + 6SiO_3^{2-} + 2X \rightarrow Na_6[AlSiO_4]_6 2NaX \cdot nH_2O + (6-n)H_2O + 12OH^- \quad (29)$$

Where X can be $\frac{1}{2}CO_3^{2-}$, $\frac{1}{2}SO_4^{2-}$, Cl^-, or OH^-. After alkali leaching, the carbon content was increased from 90.43% to 97.19%. However, it is important to note that the aluminosilicate phases and residual oxides, such as ferric oxide, can be dissolved by leaching with HCl [3]. Subsequently, the carbon content of alkaline leached graphite after a subsequent acid leaching step increased the carbon content from 90.88% to 98.06% [3].

1.7 A Potential Alternative Lixiviant: Phosphoric acid (H_3PO_4)

Phosphoric acid, also known as orthophosphoric acid, is a colorless, odorless phosphorus-containing inorganic acid, and is commonly used as an etching agent in dentistry, a food additive, bonding agent, and is the acid from which phosphorus fertilizers are produced [36]. Phosphoric

acid is produced from the dissolution of apatite minerals. Apatite minerals include calcium phosphates that include fluoride, chloride, and/or carbonate, such as carbonated apatite ($Ca_5(PO_4)_3(CO_3)$), commonly found in sedimentary deposits, and fluorapatite ($Ca_5(PO_4)_3F$), or chlorapatite ($Ca_5(PO_4)_3Cl$) [36]. Fluorapatite is more concentrated in igneous apatite deposits.

Some of the physical and chemical properties of phosphoric acid include: melting/freezing point at 21 °C, boiling point at 158 °C, specific gravity of 1.68, and molecular weight of 98 g/mol [37]. Moreover, it has high-temperature stability, low vapor pressure, and tolerance to carbon monoxide and carbon dioxide formation [38]. Having a polyprotic acid characteristic, phosphoric acid releases hydrogen atoms in a stepwise manner, also known as stepwise ionization [39]. This is illustrated in Eqs. 30 - 32, with the K_a values for 25°C [40].

$$H_3PO_{4(aq)} + H_2O_{(l)} \rightarrow {H_3O^+}_{(aq)} + {H_2PO_4}^-_{(aq)}, \quad K_{a1} = 6.9 \times 10^{-3} \tag{30}$$

$${H_2PO_4}^-_{(aq)} + H_2O_{(l)} \rightarrow {H_3O^+}_{(aq)} + {HPO_4}^{2-}_{(aq)}, \quad K_{a2} = 6.2 \times 10^{-8} \tag{31}$$

$${HPO_4}^-_{(aq)} + H_2O_{(l)} \rightarrow {H_3O^+}_{(aq)} + {PO_4}^{3-}_{(aq)}, \quad K_{a3} = 4.8 \times 10^{-13} \tag{32}$$

The speciation of phosphoric acid is summarized in Figure 1-5.

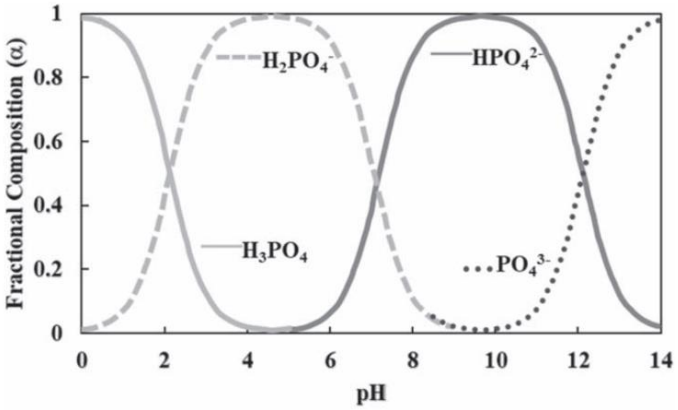

Figure 1-5. Phosphoric acid speciation as a function of pH [41]

pH is a measure of the hydrogen concentration in an aqueous solution, where as pK_a is a pH value at which a chemical species can accept or donate a proton [40]. The pKa can be used as a threshold to predict the acid speciation by comparing it with the working pH as shown in Figure 1-5.

The ionization constant is an equilibrium constant for acid (K_a)/base (K_b) ionization. It is also a quantitative way of expressing the acid or base's strength [39]. A strong acid will completely ionize resulting in large K_a, whereas weak acids will only partially ionize which is characterized by small K_a. decreases significantly with from K_{a1} to K_{a3}. This decline in the ionization constants indicates that the degree of ionization becomes less important with each successive step, thus the acidic power of H_3PO_4 is the greatest. Considering the differences in ionization constants by a factor of 10^5 - 10^6, calculations can be facilitated by treating each ionization step as an individual reaction [39].

The pKa can be calculated from Ka as shown in the Equation 33 [39].

$$-\log(K_a) = pK_a \tag{33}$$

To date, no publically available research study on the purification of concentrated graphite or with phosphoric acid was identified. Jagtoyen et al. report on coal purification by of phosphoric acid leaching to produce activated carbon noted both iron and silicate dissolution [42]. They reported that iron phosphate ($FePO_4$), aluminum tripolyphosphate ($Al(PO_3)_3$) and $Si_2P_2O_7$ were in the ash from coal treated with high temperature, concentrated phosphoric acid, suggesting an affinity between these impurities and phosphorus chemistry. As the coal matrix is a also organic carbon, applying a phosphorus-base lixiviant to graphite may open doors to an innovative approach of dissolving the metal oxide, metal sulphide, and silicate contaminants found in concentrated graphite. The use of phosphoric acid as the lixiviant is promising, as phosphoric acid was employed to recover valuable metals from waste cathode materials ($LiCoO_2$) of spent lithium-ion batteries by Chen et al. [43]. Their experimental result confirmed the initial conjecture of phosphoric acid being an effective cathode lixiviant, as they were able to recover over 99% of the cobalt and lithium [43].

Orthophosphoric acid differs from the stronger acids because of its smaller ionization constants which qualify it as a weaker acid than HCl or H_2SO_4. Their ionization constants are greater than 1, meaning they undergo complete ionization and therefore have higher acidic strength than H_3PO_4 [39]. In contrast, HF is also a weak acid, which is related to its hazardous property of infusing through skin, and damaging the underlying tissues by the action of fluoride reducing local calcium and magnesium concentrations [21]. Moreover, phosphate ions may cause interference when

measuring cation concentrations due to complexation and precipitation [44]. These reasons may explain why phosphoric acid has not garnered much attention as a graphite ore lixiviant. This work explored the use of both phosphoric acid and polyphosphate chemistry to enhance the leaching performance of phosphoric acid to a comparable level to other frequently used acids.

1.8 Enhanced Phosphoric Acid: Condensed Phosphoric Acid (CPA)

In this section, condensed phosphoric acid will be addressed. The scope of this section will focus on the manufacturing route of condensed phosphoric acid, a comparative examination of the condensed phosphoric acid and other strong acids, and few research findings using condensed phosphoric acid as a lixiviant.

1.8.1 Overview: condensed phosphoric acid (CPA) and its use in industry

Condensed phosphoric acid (CPA) is polymerized orthophosphoric acid. By increasing the concentration of orthophosphoric acid, PO_4^{3-} tetrahedra are bonded by sharing a "bridging oxygen" atom, as shown in Figure 1-6. Generally, CPA can be made by dissolving solid phosphorus pentoxide, P_2O_5, into an orthophosphoric solution, or condensing orthophosphoric acid by directly heating and concentrating the acidic solution by dehydration [37].

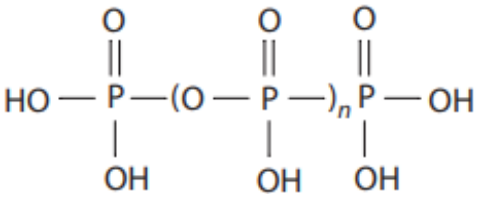

Figure 1-6. Semi structural model of linear polyphosphoric acid [37]

The simplest strong phosphoric acid, condensed phosphoric acid (CPA), is pyrophosphoric acid, $H_4P_2O_7$. It is formed by heating phosphoric acid to above 210 °C, or by condensation of H_3PO_4 with $POCl_3$, as represented in Figure 1-7 and Figure 1-8 [36, 45].

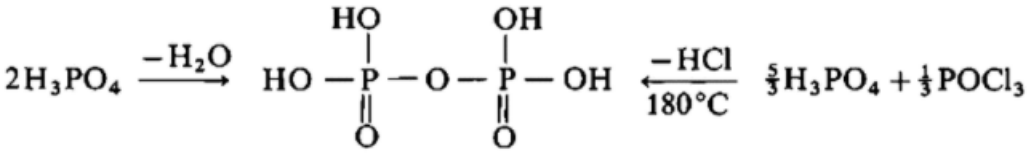

Figure 1-7. Formation of pyrophosphoric acid [36]

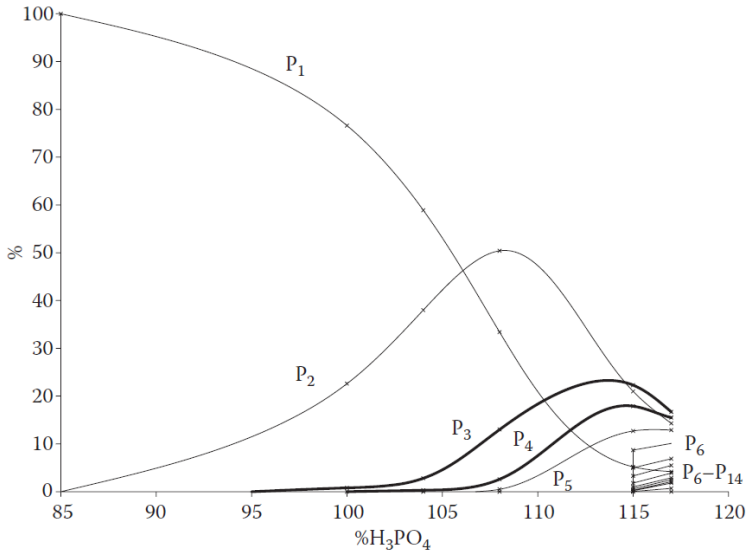

Figure 1-8. Phosphorus (P) compound speciation according to the concentration of polyphosphoric acid. P_x represents the number of P atoms. The y-axis is the % composition of the different P- compounds [37]

The "strong" phosphoric acids with higher pKa, or CPA, are also defined as equilibrium mixtures of phosphoric oxide and water containing more than 72.4% of phosphoric oxide, P_2O_5, forming a polymeric structure of $H_{n+2}P_nO_{3n+1}$ [46]. Though later studies have revealed that condensed phosphoric acids are typically available starting at 70% of P_2O_5 concentration, which is 96.6% of H_3PO_4 (Figure 1-8) [37]. As the acid is concentrated through the dehydration process, phosphate ions condense and form a long chain of P bridged by oxygen atoms. Phosphoric acid polymerization proceeds further, and eventually a greater variety of polymerized phosphoric acids, such as triphosphoric acid, $H_5P_3O_{10}$, tetraphosphoric acid, and $H_6P_4O_{13}$ form [37]. The compound solution containing these acids is called "polyphosphoric acid". It is suggested to manipulate polyphosphoric acid above 100°C as the viscosity of polyphosphoric acid is high at low temperature, and polyphosphoric acid may even crystallize partially [37, 46].

The polymerization, or joining mechanism, occurs in a linear manner in the range 68 - 81 % P_2O_5 as shown in Figure 1-9. Beyond this range, cyclic metaphosphoric acids start to form. Branching and crosslinked polyphosphate anions are created at the higher concentration and temperature conditions, as shown as in Figure 1-9 [37].

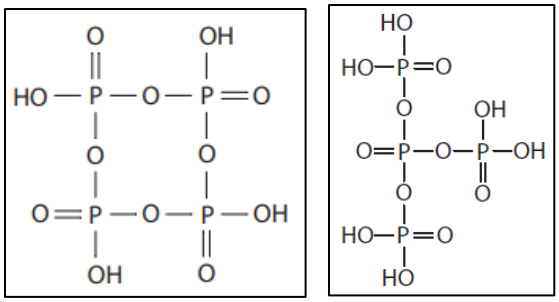

Figure 1-9. Semi structural model of metaphosphoric acid [37]

These polymerized orthophosphoric acids are used in industrial applications such as manufacturing of pigments, pharmaceutical intermediates, fine chemicals, synthetic fibers, and ceramics [37].

1.9 Comparative Look: How Much Stronger Is Condensed Phosphoric Acid?

Phosphoric acid with high pKa is generated by polyphosphate formed from concentration orthophosphoric acid, or $POCl_3$ addition. The acidic strength is established by comparing the K_a values. K_a is larger for stronger acids. The K_a values at 25 ˚C for phosphoric acid and the simplest CPA, pyrophosphoric acid, are compared in Table 1-5 [40].

Table 1-5. Comparison between K_α values of phosphoric and pyrophosphoric acid (25 °C)

Acid	$K_{\alpha 1}$	$K_{\alpha 2}$	$K_{\alpha 3}$
H_3PO_4	6.9×10^{-3}	6.2×10^{-8}	4.8×10^{-13}
$H_4P_2O_7$	1.2×10^{-1}	7.9×10^{-3}	2.0×10^{-7}

All three dissociation constants increase with phosphoric acid polymerization. The first dissociation constant increased by two orders of magnitude by condensation. In the case of pyrophosphoric acid, the improvement in acidic strength is related to the characteristic structure of pyrophosphoric acid and the increased proton transferability. The central oxygen atom in $H_4P_2O_7$ acts as an electron sink that increases the acidity of OH groups of the molecule [47]. In other words, the electron sink draws the electron density away from the OH groups, hence weakening the OH groups and facilitating the dissociation of hydrogen as H^+. This phenomenon is also known as the inductive effects [48]. The low proton ("H^+") transfer barrier of $H_4P_2O_7$ contributes to the efficient structural diffusion of hydrogen atoms within its molecular structure [47].

Strong acids are conventionally defined as acids that are completely dissociated in aqueous solution and having K_α higher than 1 [49]. The K_{a1} value of pyrophosphoric acid is relatively high

compared to other moderately strong acids, though it is still insufficient to be qualified as "strong acid". The K_a values of a few moderately acidic acids at 25°C compared with K_{a1} of pyrophosphoric acid are provided in Table 1-6. Only $K_{\alpha 1}$ of the CPA was considered for the comparison with the assumption that first ionization step is the most significant [40].

Table 1-6. Comparison of K_α values for moderately strong acids (25 °C)

Acid	HA	$K_{\alpha 1}$
Pyrophosphoric	$H_4P_2O_7$	1.2×10^{-1}
Iodic	HIO_3	1.6×10^{-1}
Oxalic	$H_2C_2O_4$	5.9×10^{-2}
Sulfurous	H_2SO_3	1.54×10^{-2}
Sulfuric (2)	HSO_4^-	1.2×10^{-2}
Chlorous	$HClO_2$	1.1×10^{-2}
Arsenic	H_3AsO_4	5.0×10^{-3}

1.10 Condensed Phosphoric Acid as an Effective Lixiviant

With superior acidic strength than orthophosphoric acid, condensed phosphoric acid (CPA) could potentially dissolve the commonly found impurities in graphite, similarly to hydrochloric acid or sulfuric acid. It has been reported that CPA can decompose up to 70 natural minerals among sulfides, oxides, silicates, and carbonates [44].

CPA garnered the attention of a few researchers. Hannaker investigated the dissolution of commonly found geological materials, such as silicate, oxide, sulfide, and carbonate minerals, with heated phosphoric acid (85%) at 290 °C [50]. Though ineffective sulfide dissolution was attributed to the poor oxidizing power, the condensed phosphoric acid rapidly dissolved impurities containing silicate, oxide, and carbonate minerals [50]. With the addition of perchloric acid, the heated phosphoric acid exhibited a stronger oxidizing behavior. The acid mixture dissolved the sulfur minerals [50].

Mizoguchi and ishii performed a series of experiments with CPA by heating orthophosphoric acid (85%) at 300 °C. They examined the decomposition behavior of sulfur compounds specifically by comparing the effectiveness of CPA, and a mixture of CPA and the reducing agents sodium hypophosphite and tin [51]. When the test sample was leached with CPA only, a complete recovery of sulfur was empirically measured for galena (PbS) and sphalerite (ZnS). For the same experiment,

only a partial recovery was observed for other sulfur compounds including pyrite (FeS_2), chalcopyrite ($CuFeS_2$), nickel sulfide (NiS), cobalt sulfide (Co_xS_y), and cadmium sulfide (CdS). The recovery of these compounds was significantly improved upon the addition of sodium hypophosphite and tin, except for chalcopyrite ($CuFeS_2$). This was attributed to the difficulty at dissolving the copper (II) sulfide. This was because the chalcopyrite first decomposes into copper (II) sulfide and iron (II) sulfide, and the former is more stable than the latter without the presence of a reducing agent in CPA (Eq. 34) [51]. The iron (II) sulfide easily decomposed and generated hydrogen sulfide gas (H_2S) (Eq. 35) [51]:

$$CuFeS_{2(s)} = CuS_{(s)} + FeS_{(s)} \quad (34)$$

$$FeS_{(s)} + 2H^+ = Fe^{2+} + H_2S_{(g)} \quad (35)$$

H_2S gas evolution is in accordance with the result of Nagashima's study whose research scope focused on sulfide-sulfur and sulfate-sulfur evolutions by comparing the effect of contacting with tin(II)-strong phosphoric acid or strong phosphoric acid [52]. It was demonstrated that when CPA was used alone (prepared by heating H_3PO_4 for 30 min at 280 °C), sulfide-sulfur evolution occurred by generating H_2S. When tin was added as a reducing agent, both sulfide-sulfur and sulfate-sulfur were reduced to H_2S under the same experimental conditions [52].

H_2S generation was mentioned in a study of activated carbon purification from coal - an analogous example of graphite processing. Jagtoyen *et al.* conducted a synthesis of activated carbon using phosphoric acid and heat treatment [42]. From the H/C ratio and S/C ratio analysis, they observed a higher yield of carbon after acid leaching, caused by reduced hydrogen and sulfur contents. This result was assumed to be caused by the emission of H_2S during leaching. It was remarked that a highly cross-linked structure between activated carbon and P=O groups could have formed during leaching, providing higher resistance to the volatile carbon loss [42]. Strong phosphoric acid was the lixiviant; thermal treatments were performed between 350 – 650 °C [42]. Section 1.8 reviewed how phosphoric acid heated to temperatures above 210 °C triggers the formation of CPA. Therefore, it is assumed that the phosphoric acid must have transformed into CPA, and the higher ionizability of CPA must have contributed to the evolution of H_2S gas at the elevated temperature [42]. Moreover, the XRD analysis result of the ash generated by incinerating the leached carbon product identified $FePO_4$, $Al(PO_3)_3$, and $Si_2P_2O_7$. These solids align with another study that underlined the

capability of strong phosphoric acid to form chemical compounds with stable geological minerals [42, 53].

Mizoguchi & Ishii further investigated the solubility of various metallic compounds in CPA [54]. They examined the solubility of iron ores in CPA. They observed a rapid decomposition of all the iron ores at 99.9% within 20 minutes. This was significantly shorter than the several hours required to perform the iron ore leaching with HCl, according to the Japanese Industrial Standard (JIS) method [54]. The dissolved iron minerals in the ores were limonite ($FeO(OH)_nH_2O$), hematite (Fe_2O_3), and magnetite (Fe_3O_4) [54]. The author made an important comment on the leaching temperature, as CPA during leaching may solidify when heated above 300 °C and for extended time. This solidification may be due to impurities precipitating as phosphate complexes, and the elevated temperature favoring the precipitation process [55]. In light of this, a working temperature of 290 °C was recommended by the author [54]. Moreover, they noted that limonite reacts exceptionally well with CPA to form iron phosphates, even at a temperature as low as 210°C, which is within the temperature range when condensed phosphoric acid starts forming.

Another study by Minoguchi & Ishii examined the effect of CPA on bauxite ore containing aluminum, iron, and titanium [56]. Their experiment successfully dissolved aluminium and iron using CPA even at a relatively low temperature of 220°C, though titanium required more dissolution time than other impurities [56].

A comprehensive study on the high-temperature reaction of phosphoric acid with muscovite ($KAl_2(F, OH)_2$ or $(KF)_2(Al_2O_3)_3(SiO_2)_6$) was conducted by Varadachari [53]. The experiment was conducted at high temperatures (at 250 °C, 300 °C, and 350 °C) to promote the formation of CPA. The result demonstrated the solubilization of major cationic constituents of muscovite, namely K^+, Al^{3+}, and Si^{4+}. The author suggested a new reaction perspective of condensed phosphoric acid with muscovite; the reaction mechanism of CPA does not necessarily occur by the acid attack (exchange of H^+ of the acid), nor the reactive polyphosphates produced at high temperature, but rather the cleavage of chemical bonds by OH^- ions that are produced during the polymerization of phosphoric acid at high temperature [53].

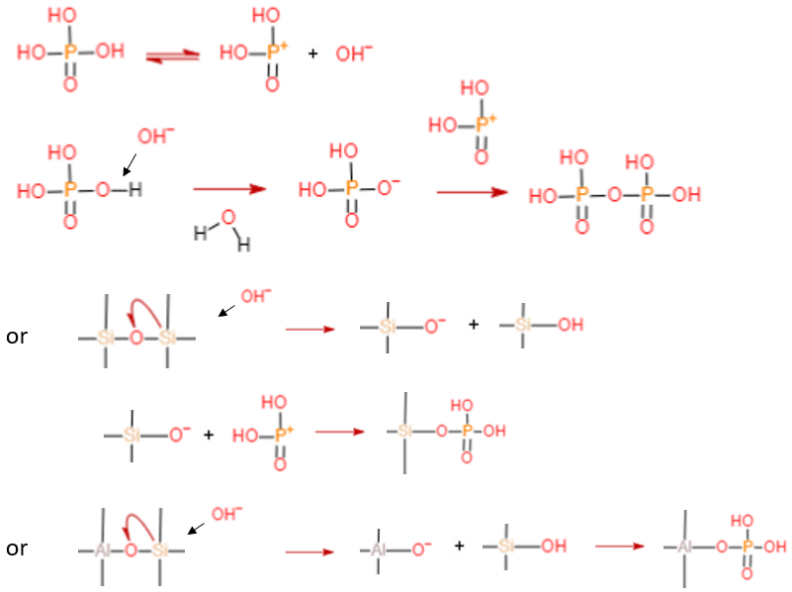

Figure 1-10. Proposed mechanism of oxygen cleavage adapted from [53]

As shown in Figure 1-10, heating of phosphoric acid condenses phosphate ions, creates a bridging oxygen, and produces OH^- ions. The OH^- ions react with oxygen-containing groups by forming hydroxide-bonded groups. If this hypothesis is valid, the rate-limiting step of impurity dissolution is the availability of OH^- ions which are in abundance only at the initial stage of reaction [53]. In other words, a long residence time will not necessarily guarantee a higher removal fraction of impurities. Furthermore, the use of a strong base, such as NaOH, could be avoided as OH^- can be provided from phosphoric acid condensation. Considering this, it has the potential to be an effective lixiviant of the impurities in graphite ores.

1.11 Conclusions

In this chapter, an overview of the graphite market and graphite beneficiation methods were discussed. The graphite market is forecasted to grow progressively given the current role of graphite in high-end applications. The graphite value is dependent on two factors: the graphite purity and graphite size. Greater graphite size correlates to greater graphite value. The beneficiation methods are categorized by physical and chemical approaches. The chemical beneficiation allows the graphite purity beyond 95 %, while physical beneficiation is limited to 95 %. The graphite purity is commonly measured by the carbon content. Graphite leaching by conventional methods, and with phosphorus chemistry was scrutinized and phosphoric acid as the novel lixiviant for graphite leaching was proposed.

2 Introduction to State-of-the-Art Graphite Characterization Techniques & Characterization of the Concentrated Graphite for the Current Study

In this chapter, the state-of-the-art graphite characterization techniques are addressed: X-ray powder diffraction (XRD), scanning electron microscopy (SEM), and energy dispersive spectroscopy (EDS). A brief theoretical overview of the four solid characterization techniques and graphite characterization techniques with XRD and Raman spectroscopy are discussed in this chapter. Furthermore, the graphite sample in the current study was characterized and described.

Table 2-1. Author Statement

Conceptualization, Writing (Review & Editing)	Hak Jun Oh Associate Professor Sidney Omelon
Investigation	Hak Jun Oh Tian Zhao (Ph.D. Candidate)
Writing – Original Draft	Hak Jun Oh

2.1 State-of-the-Art Graphite Characterization

X-ray powder diffraction (XRD) is an analytical technique that identify crystal structures by measuring atomic spacing within a crystal lattice. This technique is based on constructive interference of x-rays within a crystalline sample [57]. Raman spectroscopy is non-destructive and vibrational spectroscopy method that provides detailed information about chemical structure, phase, and molecular interactions from Raman-active bonds. It is based on the interaction of low-powered laser with the chemical bonds within a material, also called the Raman scatter effect [58]. Based on these two techniques, it is possible to understand some of the structural characteristics of graphite.

2.2 Powder X-Ray Diffraction

X-ray diffraction is an analytical technique primarily for the understanding of crystal structures, phase identification, and atomic spacing [59]. Crystalline materials have a long-ranged ordered lattice structure, a 3-dimensional pattern of atoms, ions or molecules, which is repeated over a length scale that diffracts x-rays typically generated by copper or cobalt cathode ray tube [60]. The sample analyzed by powder XRD is required to be crushed into a fine and homogeneous powder to reduce the preferential orientation effect that may create misleading peak intensity results. Powder XRD relies on the constructive interference patterns of the x-ray in a crystalline sample. The constructive interference patterns are detected and used to characterize the crystalline sample,

as the patterns appear at specific x-ray incident angles. These angles can be related to the d-spacing between the lattice planes, which is represented by the Bragg's equation [60]:

$$2dsin\theta = n\lambda \quad (36)$$

Where d is the lattice plane spacing, θ is half of the corresponding diffraction angle, n is the diffraction order, and λ is the wavelength of the X-ray source [61].

With a copper anode, graphite has its characteristic primary peak at 26.369 °2θ with (002) having a d-spacing of 0.3372 nm [62]. Oxidation of graphite shifts this characteristic peak to 9.535° (0.9628 nm d-spacing) due to the oxygen atoms being introduced into the graphite interlayer spaces [62]. The different positions of this primary graphite XRD peak are shown in Figure 2-1.

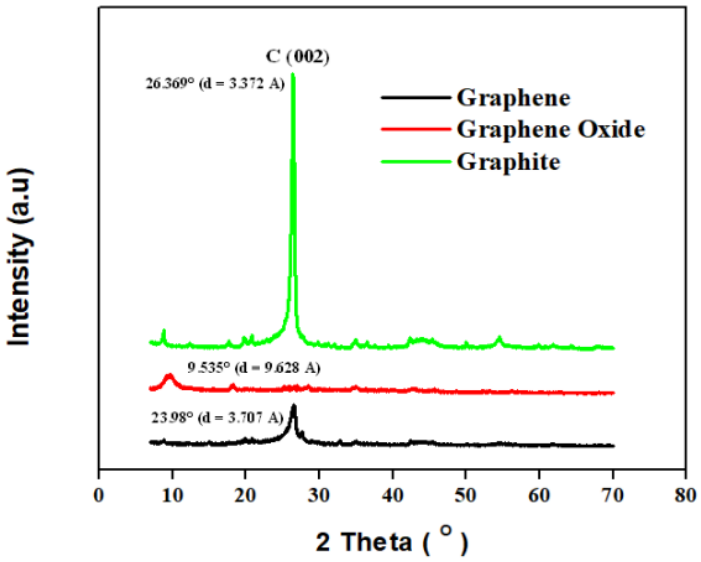

Figure 2-1. X-ray diffraction pattern of graphite, graphene oxide and graphene [62]

Generating x-ray diffraction patterns of the graphite before and after the purification process can identify peaks shift caused by the purification process [63]. If the primary graphite ore peak shifts to a higher two-theta angle, it is interpreted as a reorganization of the graphite crystal that decreases the distance between the graphite interlayers; this is also called "graphitization". For instance, Gao et al. focused on recycling graphite from a spent battery [63]. They performed a structural analysis of graphite to evaluate the graphite using the XRD patterns. The primary peak of the commercial grade graphite was initially at 26.51 °2θ (d_{002} = 0.336 nm), and the peak of the spent graphite from the used battery shifted to a value of 26.07 °2θ (d_{002} = 0.342 nm). After their graphite recycling process, the "refined graphite" peak position was increased from the spent graphite value to

26.35 °2θ (d_{002} = 0.338 nm), but did not match the commercial grade primary peak position (Figure 2-2) [63].

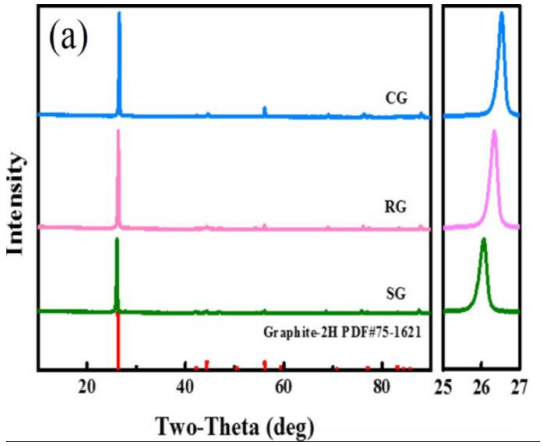

Figure 2-2. XRD analysis results for commercial graphite (CG, blue), refined graphite (RG, pink), and spent graphite (SG, green) [63]

The authors interpreted the shift to increased °2θ value for the primary diffraction peak after the refining process as a representation of the transition from a disordered carbon structure to an ordered crystal structure, leading to a smaller interlayer spacing. Additionally, the authors noted that the two-theta peak of refined graphite is slightly lower than commercial graphite due to residual organic substances, such as conductive agents and binders [63].

There is another material characteristic that can be extracted from powder XRD peaks. The full width of the XRD peak at its half maximum value (β: FWHM) that is related to the size of crystalline graphitic domains inside the macroscopic graphene materials. With this, it is possible to estimate the average crystallite size, D, or the perpendicular dimension within a maintained graphitic ordering, shown in Figure 2-3.

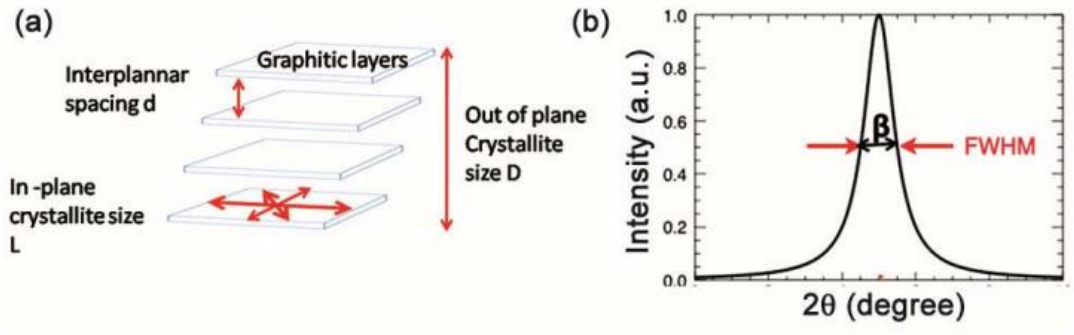

Figure 2-3. Schematic representation of a) graphite b) XRD FWHM [61]

The average crystallite size can be estimated using the Debye-Scherrer equation (Eq. 37) [61]:

$$D = \frac{K \cdot \lambda}{\beta cos\theta} = \frac{0.89 \cdot \lambda}{\beta cos\theta} \quad (37)$$

Where K is the shape factor, β is the full peak width of a diffraction peak at its half maximum height (FWHM) in radians (rad) after subtracting the instrument broadening, λ is the wavelength of the x-ray (nm) and θ represents half of the diffraction angle of the peak corresponding to inter-layer spacing ($^{\circ}2\theta$), as shown in Figure 2-3 b). The K value is assumed to be 0.89, representing for spherical crystals with cubic unit cells [61].

Similarly, the in-plane crystallite size, L, can be estimated with Eq. 38 [61],

$$L = \frac{1.84 \cdot \lambda}{\beta cos\theta} \quad (38)$$

where the K factor is 1.84 to represent the in-plane crystallite width [64].

2.3 Other Solid Characterization Technique for the Current Project: Graphite Concentrate Characterization

XRD and Raman spectroscopy are the two commonly employed solid characterization techniques for graphite. For the current project, scanning electron microscopy (SEM) and energy dispersive spectroscopy (EDS) are also used to characterize the concentrated graphite sample. In the following sections, a description of the graphite impurity identification with XRD, SEM and EDS, and the theory behind the SEM and EDS will be explored.

2.4 Brief Overview: Scanning Electron Microscopy (SEM) and Energy Dispersive Spectroscopy (EDS)

Scanning electron microscopy is a characterization technique that provides information about surface topography, crystallography, and chemical composition of solid samples. High energy electrons between 2 - 40 keV are accelerated onto the specimen surface [65]. The interaction of the electron beam with the specimen results in the emission of secondary electrons, backscattered electrons, auger electrons and other electromagnetic waves that carry characteristic information about the specimen [65]. One great advantage of SEM is in detectors of different types can collect different data from the same sample [66]. Secondary electrons (low energy of below 50 eV, topographic information), backscattered electrons (high energy, crystallographic and

compositional information) and X-rays (chemical composition) comprise the commonly used electron microscopy signals [66].

Energy dispersive spectroscopy (EDS) is a technique that provides information on the chemical composition of the specimen by analyzing the energies emitted when the specimen is "excited" by the electron beam [66, 67]. The incident, high energy electron beam generates electron vacancies in the inner electron shells. These vacancies are filled with electrons from higher energy shells. By the law of energy conservation, this reduction in electron energy generates X-rays with discrete wavelengths that can be associated with elements. These energy emission quanta provide suggestions for elemental chemical composition [67].

2.5 Characterization of the Concentrated Graphite for the Current Study

2.5.1 Scanning Electron Spectroscopy (SEM)

The preliminary characterization of the graphite concentrate was undertaken by Reichert [68]. Graphite concentrate images were obtained using scanning electron microscopy. The concentrate graphite is coarse flake graphite (>150 μm). Two SEM images are provided in Figure 2-4.

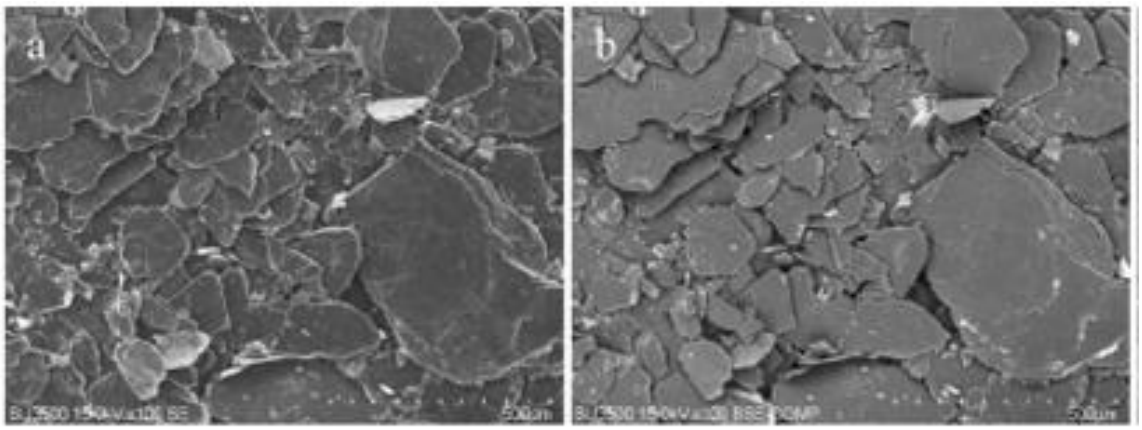

Figure 2-4. Hitachi SU 3500 images of graphite concentrate in a) secondary electron b) backscatter [68]

Elements with higher atomic number (high Z contrast) result in brighter features in backscatter images [69]. Figure 2-4 b) shows scattered white regions on the graphite flake. Higher resolution images of the white regions are provided in Figure 2-5.

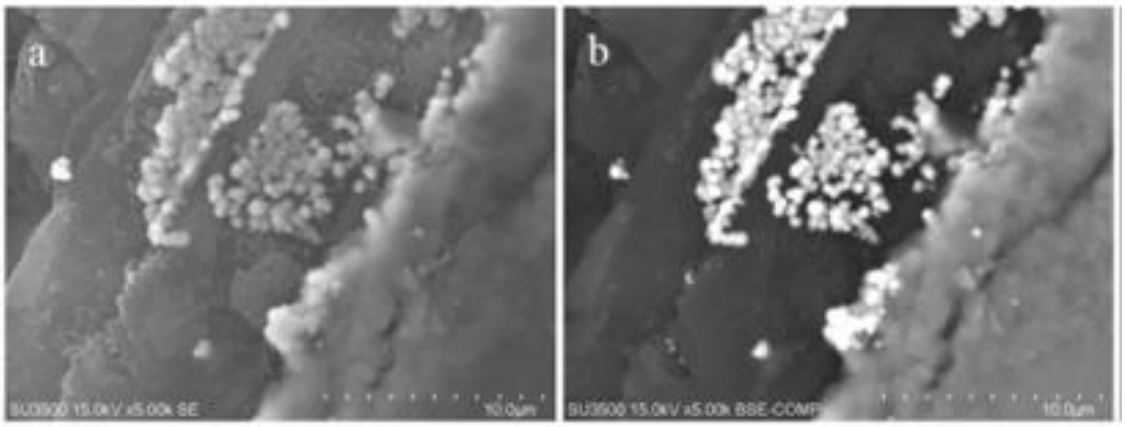

Figure 2-5. Higher resolution Hitachi SU 3500 images of graphite concentrate in a) secondary electron b) backscatter [68]

White clusters are observed on the surface of concentrate graphite flake and they are suspected to be the impurities.

2.5.2 Energy Dispersive Spectroscopy (EDS)

Elemental identification was performed with EDS to characterize possible impurities in the graphite sample. The EDS result revealed scattered distribution of four predominant elements (Fe, K, Al, and Si). Carbon is described in blue in Figure 2-6.

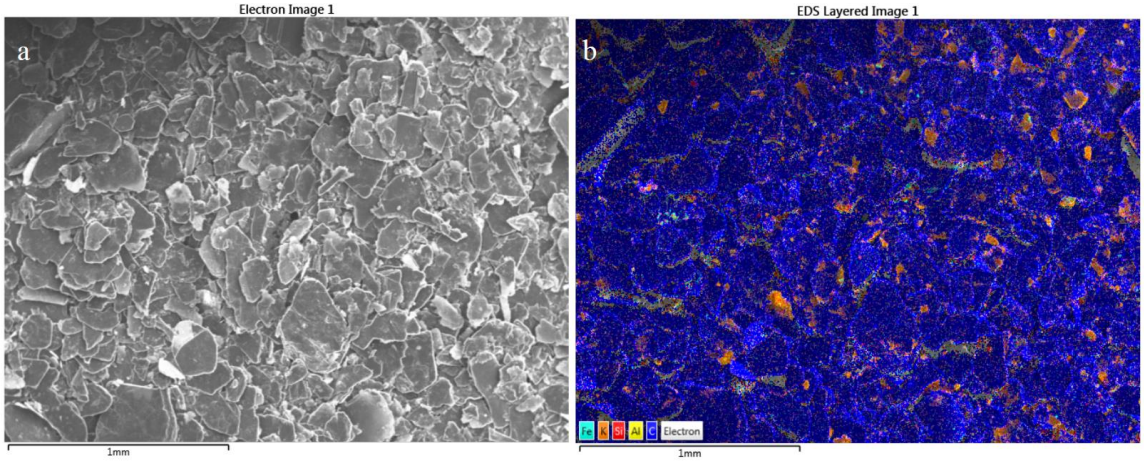

Figure 2-6. Hitachi SU 3500 images of graphite concentrate in a) secondary electron b) energy dispersive spectroscopy

K, Si, and Al overlaying suggests the possible presence of potassium-containing aluminosilicates in the graphite sample. Fe presence is assumed to be from iron sulphides, such as pyrite (FeS_2). However, this needs to be confirmed because sulfur detection was not possible with the EDS.

2.5.2.1 X-Ray Powder Diffraction by Reichert

Based on the Co-source XRD analysis reported by Reichert, major crystalline sulphide and silicate impurities in the graphite concentrate are presumed to be pyrite (FeS_2) and dickite ($Al_2Si_2O_5(OH)_4$) [68]. These results are supported by the fact that pyrite is the most abundant sulphide mineral, and dickite is a mineral found in igneous rocks, where graphite is also formed [2, 70, 71]. Cruz suggested that kaolinite ($Al_2Si_2O_5(OH)_4$) originates from the hydrolysis of feldspars (expressed in three endmembers: $KAlSi_3O_8$, $NaAlSi_3O_8$, and $CaAl_2Si_2O_8$) under hydrothermal condition following Eq. 39 [72]:

$$2xAlSi_3O_8 + 3H_2O \rightarrow Al_2Si_2O_5(OH)_4 + 4SiO_2 + 2x(OH), \quad where\ (x = K, Na, Ca) \tag{39}$$

Though kaolinite and dickite share a uniform chemical composition ($Al_2Si_2O_5(OH)_4$), kaolinite is the thermodynamically stable phase, and dickite is considered a metastable phase, which forms from the phase transition of kaolinite at elevated temperatures [72, 73]. Given that elevated temperatures and pressures in igneous rock also form graphite, a mixture of dickite and/or kaolinite, in the graphite concentrate is plausible. Careful silicate impurity characterization is recommended [74].

Feldspars are also present in igneous and many types of metamorphic rocks, in which graphite also forms [2, 75, 76]. The possibility of feldspars being a graphite impurity should remain open as it is one of the most predominant minerals, making up approximately 60 % of Earth's crust.

2.5.3 X-Ray Powder Diffraction & Crystalline Impurities Identification with a Different Diffractometer

The identification of crystalline phases was redone with a Bruker AXS D2 Phaser with Cu source. XRD patterns were built with a Lynxeye detector. Dry powdered samples were scanned at 30 kV and 10 mA from 5 to 100 °2θ, and 0.5 s per step with an increment of 0.02 °2θ. Minerals were identified using EVA (V5.2) and the ICDD Database (PDF - 4).

The XRD results strongly suggest that the impurity in the graphite concentrate is an Al containing silicate mineral as three identified crystalline impurities were all aluminosilicates as shown in Figure 2-7 and Figure 2-8. Kaolinite ($Al_2Si_2O_5(OH)_4$) originate commonly from parental minerals such as Feldspars (aluminosilicate containing K, Na and Ca) and muscovite

(aluminosilicate containing K and F) [72]. This may explain the detected K in the previous EDS result.

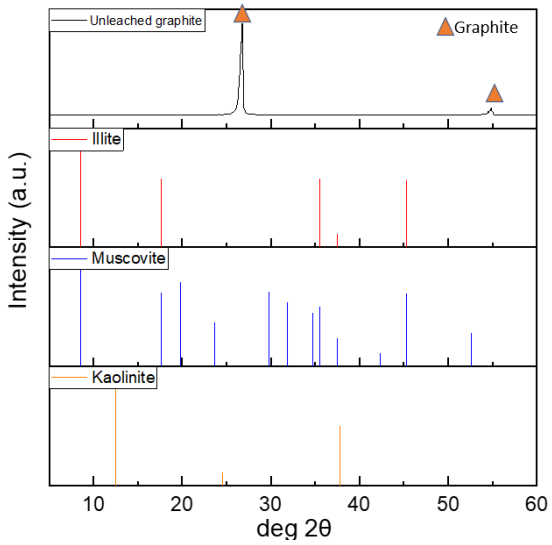

Figure 2-7. XRD result on linear scale (normalized) – measured with a Bruker D2 Phaser with a LYNXEYE detector search & matched with EVA

In Figure 2-8, graphite peaks were excluded to analyze the impurities peaks by sections as their intensities were relatively lower than graphite. It is shown that all the impurities had an aluminosilicate base. Hence, kaolinite will be considered as the sole impurity in the natural graphite concentrate because it is the most representative and simplest aluminosilicate structure [77, 78].

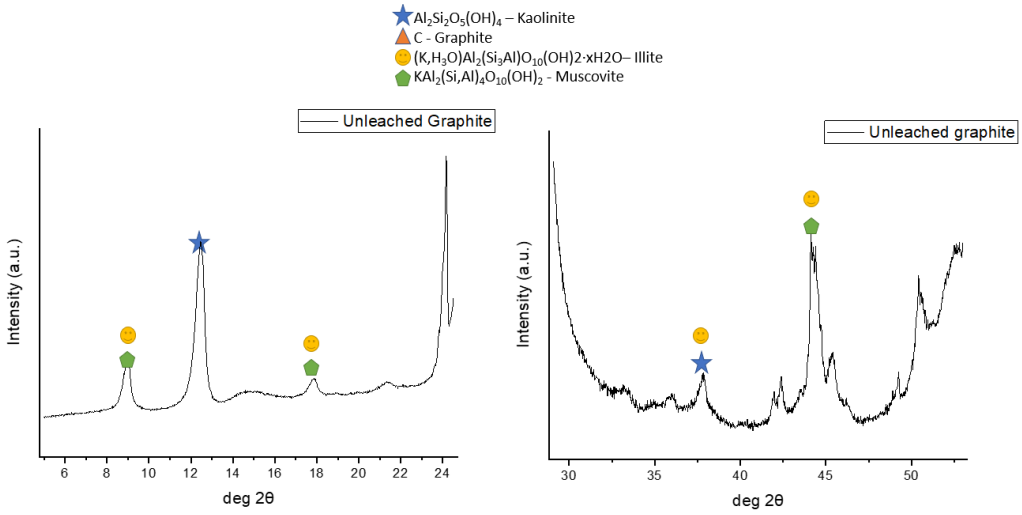

Figure 2-8. XRD result in linear scale (normalized) - measured, search & matched

Pyritic mineral (FeS_x) was assumed to be another impurity in the graphite concentrate, though the possibilities of an aluminosilicate containing Fe should not be discarded [79, 80].

2.5.4 Loss on Ignition (LOI) analysis of the Graphite Concentrate

Loss on ignition analysis allows the study of the noncombustible ash composition after the complete combustion of the organic material [81]. The carbon content, or fixed carbon content, is the percentage of organic matter in a given organic mass without the noncombustible and volatile contents [1, 5, 14, 15]. The noncombustible ash is analyzed to identify the mineral matter which is defined as impurity in graphite beneficiation techniques.

The carbon content of the graphite concentrate was 94.3 % according to the LOI analysis provided by SRG. The summary of the predominant impurities is provided in Table 2-2.

Table 2-2. LOI data of graphite concentrate (unsized) provided by SRG

Carbon Content (%)	94.3			
Volatile (%)	1.88			
Ash (%)	3.82			
Element	Si	Al	Fe	K
g/t	7386.0	6970.0	2807.0	1001.0

2.6 Conclusion

XRD and Raman spectroscopy are commonly used solid characterization techniques for graphite. For the current project, the graphite concentrate has a carbon content of 94.3 %. The results from various solid characterization techniques (XRD, SEM, EDS and LOI) strongly suggest the presence of aluminosilicate and pyritic mineral. Kaolinite is considered as the main aluminosilicate impurity due to its representative and simple crystal structure.

3 Preliminary Test: Phosphoric Acid Leaching

3.1 Motivation

Previous work demonstrated that condensed phosphoric acid heated above 100 °C can leach silicate and other minerals. A possible leaching mechanism was the effect of the condensed phosphates that form spontaneously in the hot, concentrated phosphoric acid. With the goal of developing a lower energy and lower risk impurity leaching process, the effect of limited temperature (maximum 100 °C) at atmospheric pressure, lower phosphoric acid concentration, and the use of sodium pyrophosphate ($P_2O_7^{4-}$) or polyphosphate ($\sim(PO_3^-)_{15}$) on leaching concentrated graphite is explored in this section to assess if they are potential graphite impurity lixiviants.

Table 3-1. Author Statement

Conceptualization, Writing (Review & Editing)	Hak Jun Oh Associate Professor Sidney Omelon
Investigation, Writing (Original Draft)	Hak Jun Oh
Methodology	Hak Jun Oh Ozan Kökkılıç (Research Associate) Associate Professor Sidney Omelon
Writing – Original Draft	Hak Jun Oh

3.2 Goal

This section presents the effect of elevated temperature (100 °C), phosphoric acid concentration, pyrophosphate, and polyphosphate on impurity leaching from concentrated graphite ore will be examined. The goal was to verify the hypothesis that relatively low concentration (1.0 M or less) phosphoric acid is capable of dissolving iron sulfide and silicate impurities in natural graphite concentrate, and that the relatively low concentration of sodium pyrophosphate or the same $NaPO_3$ concentration of commercial sodium polyphosphate can dissolve the mentioned impurities. The identification of impurities in the spent lixiviant will complement the objective of this investigation.

3.3 Theory

A brief description of theories and previous studies about leaching graphite impurities will be discussed in Section 3.3. A short literature review provides the rationale for the temperature, leaching time, solid to liquid ratio, and lixiviant concentrations.

3.3.1 Literature review for the selection of operating variables

The leaching process operating variables temperature, leaching time, and solid to liquid ratio were selected based on previous studies on the purification of different graphite ores by acid leaching [5, 22, 25]. The origin of natural graphite, procedure of graphite leaching, and the equipment used for the leaching process in the previous studies are assumed to be factors that are unrelated to the leaching results. Sulfuric acid, H_2SO_4, is the reference acid for the leaching experiment because sulfuric acid, like phosphoric acid, is polyprotic. Therefore, the scope of this literature review is to review and select the leaching operating variables with sulfuric acid as the reference lixiviant for concentrated graphite purification. The effect of temperature on graphite impurity leaching with H_2SO_4, HCl, and HF was reported by Kaya *et al*. (Figure 3-1).

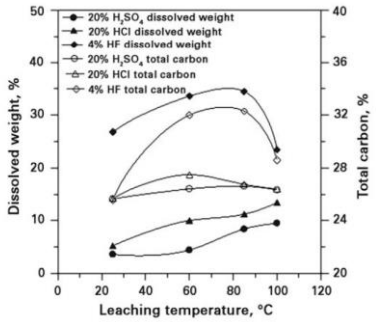

Figure 3-1. Effect of leaching temperature of natural graphite ore (Inebolu) (Solid to liquid ratio (w/v) = 1/10, 1 hour leaching time [22]

Based on the increasing sulfuric acid leaching result of Kaya & Canbazoğlu [22], 20 ˚C and 100 ˚C were selected for phosphoric acid leaching. Thi & Hong also reported the effect of temperature on graphite impurity leaching with sulfuric acid [25]. Although the error was not presented, increased impurity removal was reported with increasing leaching temperature, though the difference was assumed to be insignificant at the range of 50 – 70 ˚C, as shown in Figure 3-2 [25].

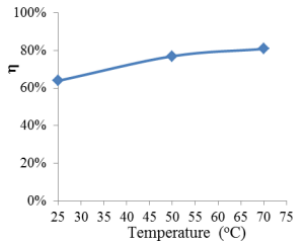

Figure 3-2. Effect of temperature on graphite impurity removal (liquid to solid ratio: 5, stirring: 200 rpm, 10 % sulfuric acid, leaching time: 60 min)
$\eta = (M_{before} - M_{after})/M_{before} \cdot 100$, where M is the graphite mass [25]

Jara & Kim reported an optimal solid to liquid ratio of around 1:6 to 1:5 (w : w) because this range yielded the largest final carbon content (%) for all tested acids at high concentrations (HF 48%, HCl 36%, HNO_3 70%, H_2SO_4 98%, and H_2O_2 30%) [5]. It is recommended to work with lower acid concentrations for safety reasons. The author justified the selected solid to liquid ratio range by addressing the detrimental effect of excessive acid usage on the environment.

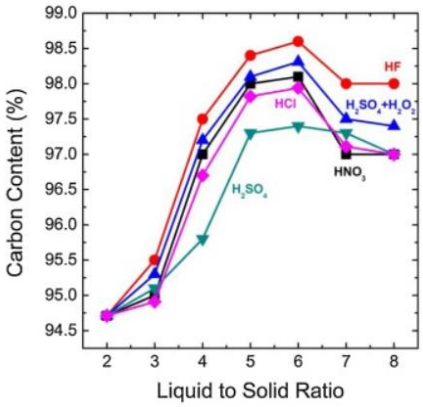

Figure 3-3. Effect of liquid to solid ratio of lixiviants: HF 48 %, HCl 36 %, HNO_3 70 %, H_2SO_4 98 %, and H_2O_2 30 %, leaching temperature ranged from 25 – 180 °C for 1-4 h [5]

In the work of Thi & Hong, the solid to liquid ratio of 1:5 was concluded to be sufficient (Figure 3-4). Higher solid to liquid ratio did not significantly impact the removal of impurities from the graphite sample [25]. The authors did not recommend a solid to liquid ratio lower than 1:3 due to challenges associated to stirring of the graphite-lixiviant slurry [25]. Though the leaching time was different, the results of Thi & Hong align with results presented by Jara & Kim. Hence, the choice of 1:6 (w/v) solid to liquid ratio was selected as a reasonable value for the current experiment.

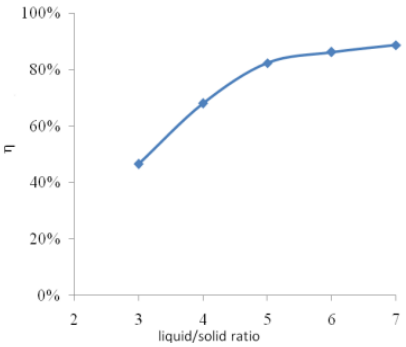

Figure 3-4. Effect of liquid to solid ratio on efficiency of impurity removal on graphite 10% sulfuric acid, stirring speed 200 rpm, room temperature, time 120 min). The efficiency is calculated as $\eta = (M_{before} - M_{after})/M_{before} \cdot 100$, where M is the graphite mass [25]

The leaching time of 175 – 250 minutes (without error estimates) was determined to be sufficient to maximize the graphite purity for all acids in the study of Jara & Kim as shown in Figure 3-5 [5].

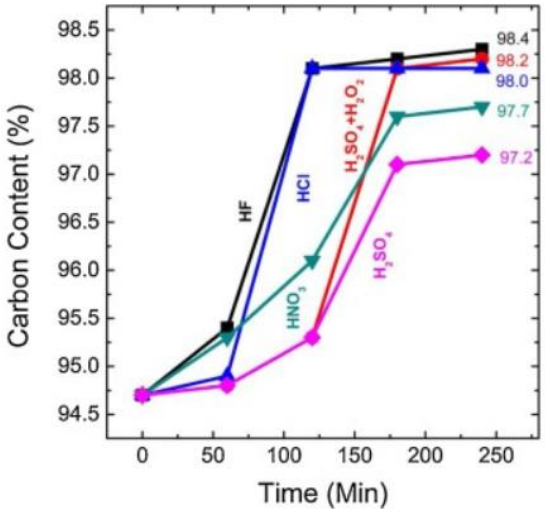

Figure 3-5. Effect of leaching time of lixiviants: HF 48 %, HCl 36 %, HNO_3 70 %, H_2SO_4 98 %, and H_2O_2 30 %, 1:5 solid to liquid ratio, leaching temperature of 70 ˚C [5]

Compared to the result of Jara & Kim, the leaching time of 120 – 150 minutes yielded the maximum graphite purity in Thi *et al.*'s work, although no error magnitude was provided (Figure 3-6) [25]. Considering the results presented by Jara & Kim and Thi & Hong, 180 minutes of leaching time was selected.

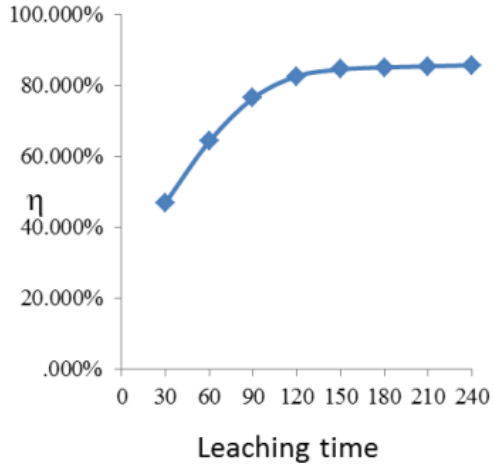

Figure 3-6. Effect of leaching time on graphite impurity removal (liquid to solid ratio 5:1, stirring speed 200 rpm, sulfuric acid concentration of %, room temperature leaching) $(\eta = M_{before} - M_{after})/M_{before} \cdot 100$, where M is the graphite mass [25]

The operating parameters in the previous works are summarized in Table 3-2.

Table 3-2. Operating parameters in previous graphite leaching studies with sulfuric acid

Reference	**Lixiviant and leaching process**	**Liquid to solid ratio**	**Temp. (˚C)**	**Reaction time (min)**	**Fixed carbon content after (%) [before (%)]**
[22]	H_2SO_4 (20 %)	10 to 1 (v/w)	85	60	N.A.
[25]	H_2SO_4 (10 %) +Alkali roasting	5 to 1	20	120	98 [92.6]
[5]	H_2SO_4 (10 %) + H_2O_2 (30 %) + Alkali roasting (Path A) + HCl (18 %) (path B) + HF (5 %) (path C)	5 to 1 & 6 to 1 (w/w)	70	175 - 250	99.68 [94.71]
[20]	H_2SO_4 + alkali roasting	4 to 1 (w/w)	20	N.A.	99.4 [87.7]
[17]	H_2SO_4 + HNO_3	N.A.	100	5.5	99.9 [92.9]

Table 3-3. Operating parameters for the current study using phosphoric acid

H_3PO_4 concentration (mol/L)	Temperature (˚C)	Leaching time (min)	L:S ratio(v:w) or (ml:g)
0, 0.1, 0.5 & 1.0	20 & 100	180	6

The operating parameters for the current work are summarized in Table 3-3.

Although the determination of operating variables was solely based on sulfuric acid lixiviant results, leaching the graphite concentrate used in this study with phosphoric acid may not show the same published trends with different operating variables due to differences in graphite origin, leaching procedure, and equipment type [17, 20].

The chosen operating variables will be optimized using Design of Experiment (DoE) to maximize graphite impurity removal.

3.4 Pregnant Leaching Solution Characterization with MicroPlasma Atomic Emission Spectroscopy

Microwave plasma atomic emission spectroscopy is an atomic emission technique. This section will be primarily based on the handbook by Agilent [82]. This technique analyzes the light emitted from the excited samples when they return to ground state. The emitted light is characterized by their specific wavelengths, and the unknown elements in the analyzed samples can be qualitatively and quantitatively identified. Similar to inductively couple argon plasma, MP-AES offers a high temperature excitation source because the nitrogen fuelled microwave plasma reaches temperatures nearing 5 000 K. Microwave energy from an industrial magnetron is used to form a plasma using the extracted nitrogen from compressed air by Agilent's Nitrogen Generator. An optimized microwave waveguide creates concentrated electromagnetic fields at the torch, forming a plasma using the powerful electromagnetic field. The emitted light from the excited atoms is then directed into a spectrometer, and MP-AES analyzes the intensities of measured wavelengths (Figure 3-7) [82].

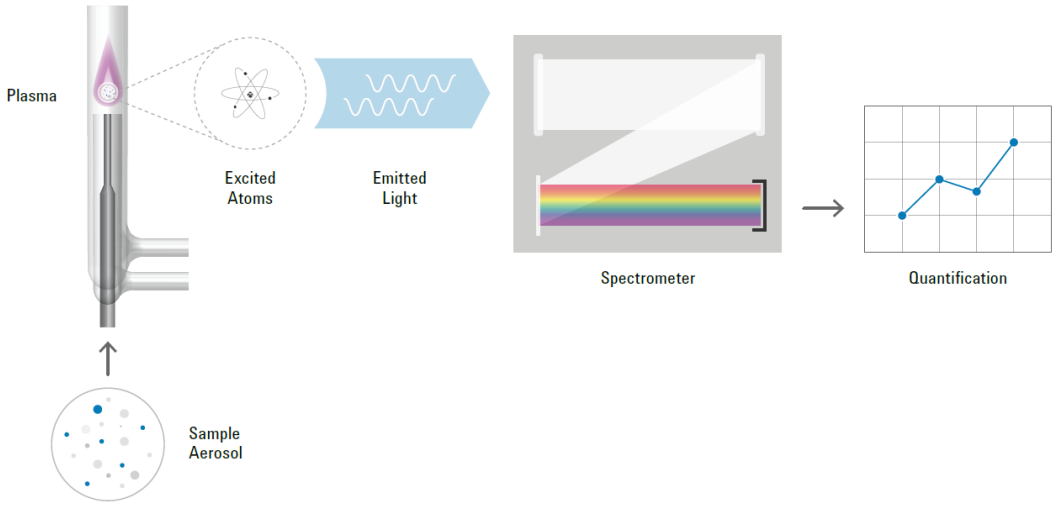

Figure 3-7. Schematic representation of MP-AES [82]

The Agilent Model 4210 was used in this work to perform the solution characterization of the pregnant leaching solutions.

3.5 Methods

Natural graphite concentrates in powder form were leached at 20 °C and 100 °C in reverse osmosis (RO) water, 0.01, 0.05, or 1 M phosphoric acid (Fisher Chemical, A242-500), pyrophosphate solution (0.1 M $NaPO_3$), or polyphosphate (0.1 M $NaPO_3$) solutions. Sodium

pyrophosphate decahydrate (Acros, CAS:13472-36-1) and sodium polyphosphate (Emplura, CAS : 10361-03-2) were dissolved in RO water. The pyrophosphate concentration was 0.1 M $NaPO_3$ based on previous work that observed successful dissolution of Fe and Al in organic matrix [83, 84]. Similarly, polyP solutions were prepared with 0.1 M $NaPO_3$ to create solutions with equivalent PO_3^- concentrations, independent of chain length.

There were twelve different leaching groups. The graphite-RO/DI water group was selected as the negative control. The samples and leaching conditions are summarized in Table 3-4.

Table 3-4. Sample group names and information

Sample Group Name	Leaching Solution Composition	Sample Group Labels
Control	RO/DI water	A1-3 (20 °C), A4-6 (100 °C)
0.10 PA	0.10 M H_3PO_4	B1-3 (20 °C), B4-6 (100 °C)
0.50 PA	0.50 M H_3PO_4	C1-3 (20 °C), C4-6 (100 °C)
1.0 PA	1.0 M H_3PO_4	D1-3 (20 °C), D4-6 (100 °C)
0.10 M PyroP	0.05 M $P_2O_7^{4-}$	E1-3 (20 °C), E4-6 (100 °C)
0.10 M PolyP	0.10 M PO_3^-	F1-3 (20 °C), F4-6 (100 °C)

2.0 ± 0.01 g of graphite was recorded and transferred to a 15 mL borosilicate glass digestion tube. 12 mL of lixiviant was added to achieve a solid to liquid ratio of 1:6, then closed with a Teflon cap. The 20 °C leached samples were placed on a shaking table for 3 h. The 100 °C leaching tests were undertaken in digestion tubes in a heat block (Dry bath/heat block., Thermo Scientific) for 3 h. Three replicates were run, and all error bars denote ± 1 standard deviation.

After leaching, the tubes were cooled to approximately 20 °C by placing them in a 4 °C refrigerator. The slurries were vacuum filtered in an Erlenmeyer filter-flask with a ceramic Buchner funnel and filter paper (Whatman, grade GF/F 0.7 µm, 41.5 mm diameter). The leached, filtered graphite was dried in a 100 °C drying oven for 20 min. The lixiviant pH was measured before and after leaching. The PLS were prepared for micro-plasma atomic emission spectroscopy (MP - AES, model Agilent 4210) by diluting in 2 % HNO_3 to measure the dissolved iron, sodium, calcium, potassium, aluminum, and silicon (measured as silicic acid) concentrations. These elements were selected as they were the impurity elements identified in the graphite concentrate with EDS by Reichert [68].

3.6 Results and Discussion

In this section, the leaching results will be presented and discussed. The effect of temperature, lixiviant types, and the possible dissolution mechanism will be described.

3.6.1 PLS pH

The lixiviant pH values before and after leaching are presented in Figure 3-8.

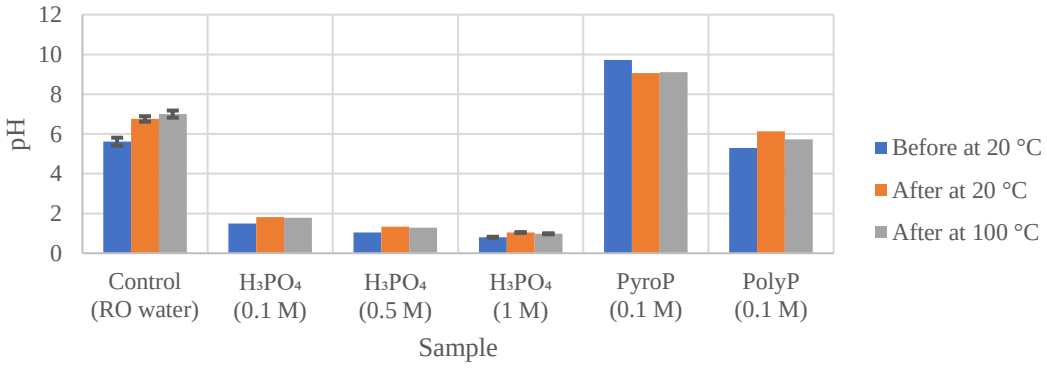

Figure 3-8. Lixiviant pH values before and after leaching for 20 °C and 100 °C (n=3). All error bars denote ± 1 standard deviation.

The result in Figure 3-4 shows that the pH was lowered with the increase in phosphoric acid concentration. This could be due to greater concentration of proton (H^+) in the solution due to single deprotonation with the increase in phosphoric acid concentration. The pH values after leaching increased slightly. The formation of silicic acid (H_4SiO_4) in the pregnant leaching solution could have led to this slight increase in pH [85, 86].

The pH of dissolved sodium pyrophosphate (0.1 M) is greater than RO water. This could be explained by the dissolved sodium pyrophosphate in RO water rapidly protonating and lowering the concentration of protons in the solution (H^+). The rationale is that pK_{a3} (second protonation threshold) is near the pH of the control before leaching (pH 5.8) [87]. The K_a values of pyrophosphate are described in Table 3-5. The Ka values are assumed to be similar at 20 °C.

Table 3-5. Pyrophosphate dissociation constants at 65.5 °C [87].

Dissociation Constant	Value
K_{a1}	0.107
K_{a2}	7.58×10^{-3}
K_{a3}	1.45×10^{-6}
K_{a4}	9.81×10^{-9}

The pK_{a3} calculation is described as:

$$pK_{a_3} = -\log(K_a) = -\log(1.45 \times 10^{-6}) = 5.84$$

The pH of dissolved sodium polyphosphate showed a slight increase after leaching which could also be due to partial protonation of the polyphosphate chain upon dissolution in the RO water.

3.6.2 PLS Element Composition

3.6.2.1 H_3PO_4 as leaching lixiviant

The dissolved impurity concentrations at 20 ˚C are presented in Figure 3-9, and the 100 ˚C leaching results are presented in Figure 3-10.

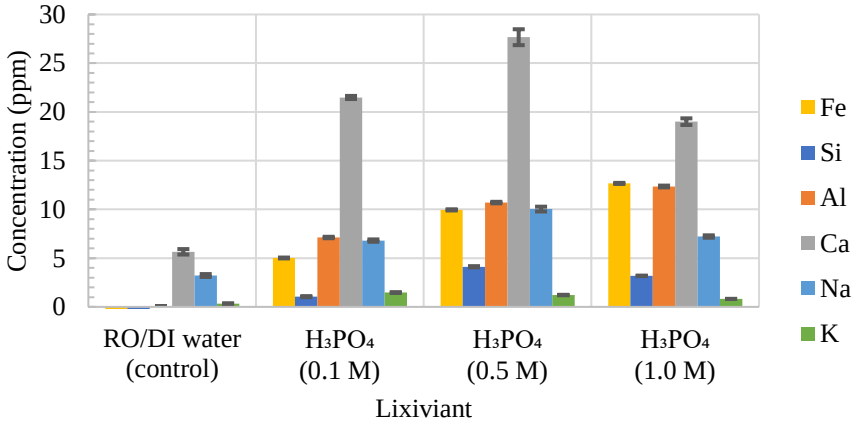

Figure 3-9. Dissolved impurity concentrations after H_3PO_4 leaching at 20 ˚C & 3 h. All error bars denote ± 1 standard deviation

One-way ANOVA is a parametric test to compare the means of two or more independent groups to verify a significant difference between the two population means [88]. The one-way ANOVA result of H_3PO_4 leached samples (0.1 M, 0.5 M, and 1.0 M) shows that they are significantly different with a F value at 70.3 (F_{crit} at 2.4) and a P value at 6.5×10^{-21}. This means that it is unlikely that the observed result difference occurred by chance. The statistical results including Tukey analysis are compiled in the Table 3-6. Tukey analysis was done on Minitab20 and the results are provided in Appendix A.

Table 3-6. One-way ANOVA result summary of H_3PO_4 samples (0.1 M, 0.5 M, and 1.0 M) leached at 20 °C & 3 h

Element	F value	$F_{critical}$	P value	Pairwise Tukey Summary
Fe	427.5	5.1	3.4×10^{-7}	Each concentration group is different
Si	81.1	5.1	4.5×10^{-5}	Each concentration group is different
Al	85.8	5.1	3.9×10^{-5}	Each concentration group is different
Ca	5.9	5.1	0.04	0.5 M and 1.0 M are different, but 0.1 M is same as 0.5 M and 1.0 M
Na	8.1	5.1	0.02	0.5 M is different, but 0.1 M and 1.0 M are the same
K	19.4	5.14	0.002	0.1 M and 0.5 M are the same, but1.0 M is different

Figure 3-9 and Figure 3-10 show that the Al and Fe leached concentrations increased monotonically. Increased phosphoric acid concentration could have led to more effective leaching of Al and Fe by forming phosphates ion-pairs that reduced the free dissolved metal concentrations. Leached Si concentration increase up to 0.5 M H_3PO_4 and it decreased at 1.0 M phosphoric acid. This may indicate that increasing acidity does not necessarily promote Si leaching. Measurable sodium (Na^+) and calcium (Ca^{2+}) concentrations were in the control solution. Figure 3-9 shows that the maximum leached calcium concentration at 20 °C was leached at 0.5 M H_3PO_4. A similar trend was observed for leached Na concentrations.

The Tukey post-hoc test suggests that Ca leaching is not enhanced with increased H_3PO_4 concentration. MP-AES analysis of Ca concentration may be underestimate Ca concentrations in higher H_3PO_4 concentrations [89]. 0.5 M phosphoric acid could be the ideal concentration to leach Ca and Na. K leached concentration remained low for all phosphoric acid concentrations. The increase in phosphoric acid concentration could impede K leaching due to preferential leaching of multivalent ions (Al and Fe) and increased probability of orthophosphate being fully protonated. Measurement artifacts could still be possibilities due to pairing between Na/K and orthophosphate. These ion pairs may form low volatility species in the MP-AES plasma, and not be detected [89].

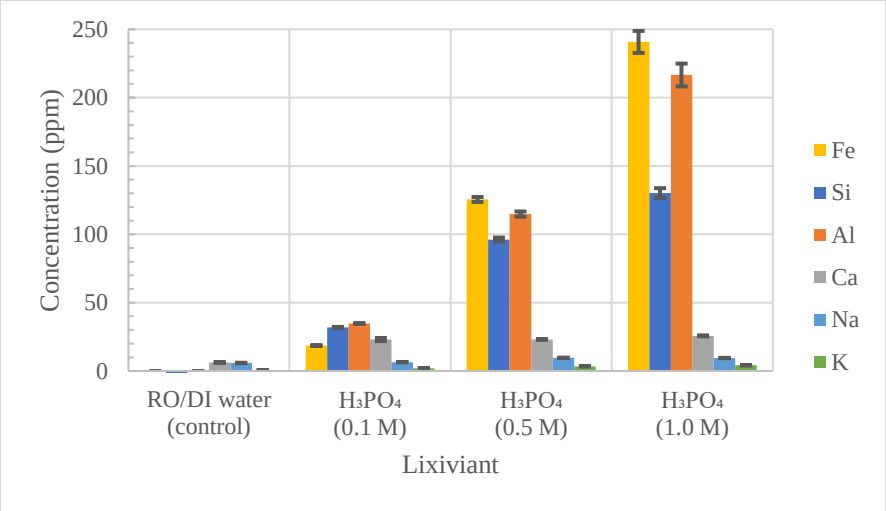

Figure 3-10. Dissolved impurity concentrations after H_3PO_4 leaching at 100 ˚C. All error bars denote ± 1 standard deviation

The two-way ANOVA result of H_3PO_4 samples (0.1 M, 0.5 M, and 1.0 M) and temperature difference (20 ˚C & 100 ˚C) showed that they were significantly different. Two-way ANOVA assesses the relationship between two categorical variables over a continuous variable [88]. The two-way ANOVA result is summarized in Table 3-7. The temperature difference is considered to be categorical: low temperature leaching (20 ˚C) and high temperature leaching (100 ˚C).

Table 3-7. Summary of two-way ANOVA PLS concentration results of 0.1, 0.5, and 1.0 M phosphoric acid, 20 ˚C and 100 ˚C

	Temperature			Interaction ([H_3PO_4] & temperature)		
Element	F value	$F_{critical}$	P value	F value	$F_{critical}$	P value
Fe	138.31	5.32	0.00	14.85	5.32	0.00
Si	266.20	5.30	0.00	6.80	5.32	0.03
Al	103.70	5.30	0.00	10.94	5.32	0.01
Ca	0.38	5.32	0.55	10.96	5.32	0.01
Na	2.54	5.32	0.15	6.59	0.03	5.32
K	87.74	5.32	0.00	3.72	5.32	0.09

Statistically significant interactions between temperature and concentration were observed for all impurities except K. The Tukey post-hoc test shows that the phosphoric acid concentration increases with high temperature resulted in substantial Fe, Si and Al extractions. This could be due to high temperature providing sufficient energy for effective leaching by phosphoric acid. Conversely, Ca leaching was not statistically different with the change in both concentration and

temperature. The Tukey result of Na leaching is inconclusive as the leached concentration means are not statistically different. The insignificant leaching of Ca and Na with phosphoric acid at 20 °C could be due to the low concentrations of Na and Ca in the graphite concentrate. The leached K concentrations were low. The measurement error may be of similar magnitude, therefore no statistical claims will be made. The Tukey post-hoc test result of interactions is provided in the Appendix B:

3.6.2.2 Possible silicate leaching mechanism in H_3PO_4

The Si leaching could be explained by a mechanism described by Crundwell [90]. Silicate mineral dissolution in acidic conditions was proposed to be initiated by the interaction of metal ions with water molecules (H_2O), and silicate groups (SiO_4^{4-}) with protons (H^+) (Figure 3-11) [90]. Once initiated, the metal and silicate dissolutions continue independently and in parallel. Metal ion dissolution was thought to be favored due to the lower energy requirement to dissociate the metal-oxygen bond than the silicon-oxygen bond [85].

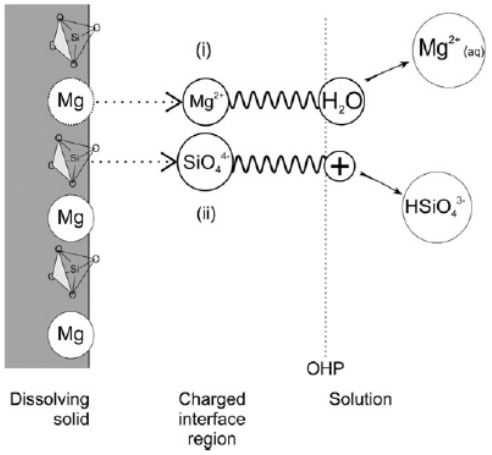

Figure 3-11. Mechanism for the dissolution of orthosilicate minerals and metal ions in acidic solutions by complexing with protons and water molecules with a Mg containing silicate OHP: Outer Helmholtz Plane [90]

The result of graphite impurity leaching with phosphoric acid (Figure 3-9 and Figure 3-10) is in concordance with Crundwell's proposed mechanism. As aluminum ions (Al^{3+}) are released from the silicate structure, the number of anionic vacancies may have increased and consequently accelerated the dissolution of the silicate groups (SiO_4^{4-}) by the attraction of protons provided by the acidic lixiviant, phosphoric acid. With the increase in concentration of phosphoric acid and temperature, the dissolution of silicate groups is likely to be amplified. Iron sulfide dissolution is

assumed to be the source of dissolved Fe^{3+}, based on the previous XRD result by Reichert [68]. Sulfur measurement was unsuccessful with the MP-AES measurement in this work, though it was reported to be possible in the petroleum industry [91].

3.6.2.3 Pyrophosphate and Polyphosphate Lixiviants

The leaching results from 0.1 M $NaPO_3$ as pyrophosphate and polyphosphate leaching are shown beside the negative control (RO water) and positive control (0.1 M H_3PO_4) leaching results for comparison in Figure 3-12 (20 °C) and Figure 3-13 (100 °C).

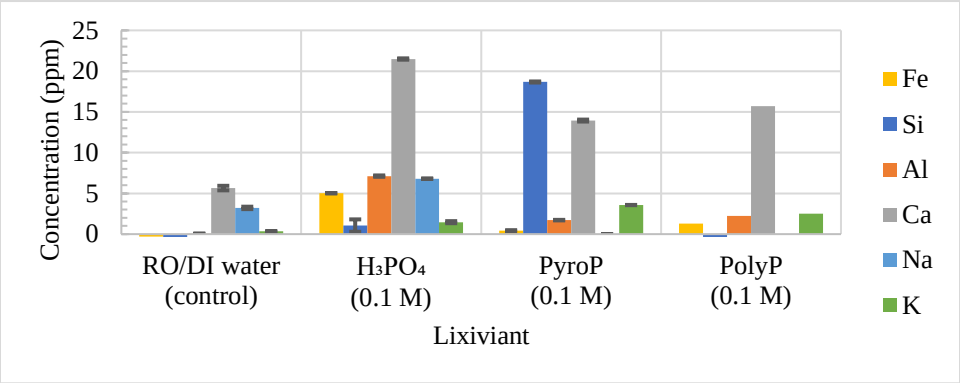

Figure 3-12 Dissolved impurity concentrations after 0.1 M ($NaPO_3$) pyrophosphate and polyphosphate leaching at 20 °C

One-Way ANOVA was performed while considering the type of lixiviant. The sodium concentration was not reported because sodium pyrophosphate and polyphosphate salts were used to prepare the solutions. Therefore, the sodium concentrations surpassed the upper MP-AES detection limit. The one-way ANOVA result of the three 0.1 M lixiviants (H_3PO_4, pyroP, and polyP) showed a F value of 13.66 ($F_{critical} = 2.4$) and a P value of 2.67×10^{-8}. This indicates the lixiviant difference is statistically significant. Pairwise Tukey post-hoc test results are summarized in Table 3-8.

Table 3-8. One-way ANOVA result summary of the three lixiviant types at 0.1 M (H_3PO_4, pyroP, and polyP)

Element	F value	$F_{critical}$	P value	Pairwise Tukey Summary
Fe	206.9	5.1	2.91×10^{-7}	Each lixiviant group is different
Si	49.5	5.1	1.8×10^{-4}	pyroP is different, H_3PO_4 and polyP are same

Element	F value	$F_{critical}$	P value	Pairwise Tukey Summary
Al	157.1	5.1	6.6×10^{-6}	H_3PO_4 is different, pyroP and polyP are same
Ca	81.1	5.1	4.53×10^{-5}	H_3PO_4 is different, pyroP and polyP are same
K	16	5.1	3.9×10^{-4}	PyroP-polyP and polyP-H_3PO_4 are same. pyroP and H_3PO_4 are different.

In Figure 3-12, 0.1 M H_3PO_4 lixiviant dissolved the most amount of Fe, Al and Ca at 20 ˚C. This could be due to preferential binding of orthophosphate with multivalent ions. The pyrophosphate solution dissolved a significant amount of SiO_4^{4-} at 20 ˚C, while Al did not dissolve well. This could be due to $Si_2P_2O_7$ formation as previously reported by Jagtoyen [42]. The 0.1 M polyphosphate solution dissolved Ca, Al and Fe more effectively than 0.1 M pyrophosphate. However, Si dissolution by polyphosphate was ineffective. Though the leached concentrations are less than 5 ppm, polyP and pyroP solution leached more K^+ than H_3PO_4. This may be due to condensed phosphorus compounds providing higher possibility of univalent ion bonding. However, this is inconclusive because pyroP and polyP solutions are not statistically significantly different.

The 100 ˚C leaching study with the three different lixiviants is shown in Figure 3-13. The two-way ANOVA results are summarized in Table 3-9 and the Tukey post-hoc result can be found in Appendix D:

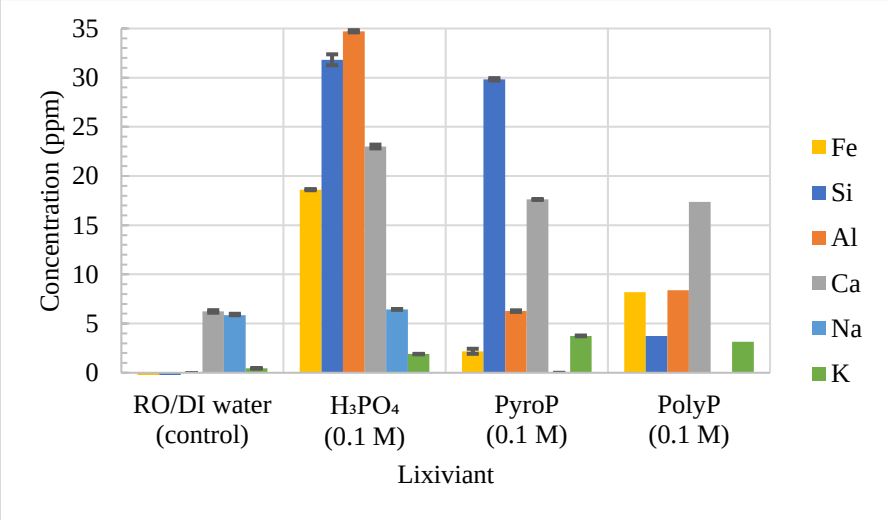

Figure 3-13. Dissolved impurity concentrations after 0.1 M ($NaPO_3$) pyrophosphate and polyphosphate leaching at 100 ˚C

Table 3-9. Summary of two-way ANOVA results of 0.1 M lixiviants (H_3PO_4, pyroP, and polyP) at 20 °C and 100 °C

	Temperature			Interaction (lixiviant type & temperature)		
Element	F value	$F_{critical}$	P value	F value	$F_{critical}$	P value
Fe	80.93	5.32	0.00	28.39	5.32	0.00
Si	23.73	5.31	0.00	3.15	5.32	0.113
Al	339.17	5.32	0.00	7.71	5.32	0.02
Ca	39.27	5.32	0.00	5.71	5.32	0.04
K	3.25	5.32	0.11	1.05	5.32	0.34

In contrast to leaching with 0.1 M phosphoric acid, the increase in leaching temperature did not improve the impurity dissolution for pyroP and polyP solutions. Fe and Al dissolutions were less than 10 ppm for pyroP and polyP even at 100 °C. Although, polyP had relatively better Fe and Al leaching results, slight improvement in Si leaching is shown in Figure 3-13. The polyphosphate leaching result suggests that it is more responsive for multivalent ions than univalent ions. The superior leachability of polyP for multivalent ions is supported by the two-way Tukey post-hoc test (Appendix F 2). The ineffectiveness of polyphosphate in Si dissolution compared to pyroP could be due to the inadequate pH range of the leaching solution and relatively weaker complexing power of polyphosphate than pyrophosphate. If leached in a more basic condition, the predominant presence of hydroxides might have expedited the dissolution process of metal ions by complexation [85]. PyroP maintained its excellent leachability of SiO_4^{4-}. The Tukey post-hoc test results show that SiO_4^{4-} leachability with 0.1 M $NaPO_3$ as pyroP is not significantly different from 0.1 M H_3PO_4 (Appendix F 2). Ca and K leaching results are inconclusive both empirically and statistically.

3.6.2.4 Possible silicate leaching mechanism with pyrophosphate and polyphosphate

This result gives an indication that pyrophosphate has the potential to be a lixiviant capable of dissolving silicate groups by forming $Si_2P_2O_7$ as described in the work by Jagtoyen et al. [42]. Another perspective is that pyrophosphate might simply have superior complexing ability than polyphosphate due to its symmetrical feature which favors the intramolecular proton exchange by minimizing the distance between adjacent proton accepters, such as oxygen [47]. Low molecular weight of pyrophosphate compared to polyphosphate could be another factor

contributing to greater dissolution of Si and Al [92]. Figure 3-14 shows a potential silicate dissolution mechanism in alkaline lixiviants [90].

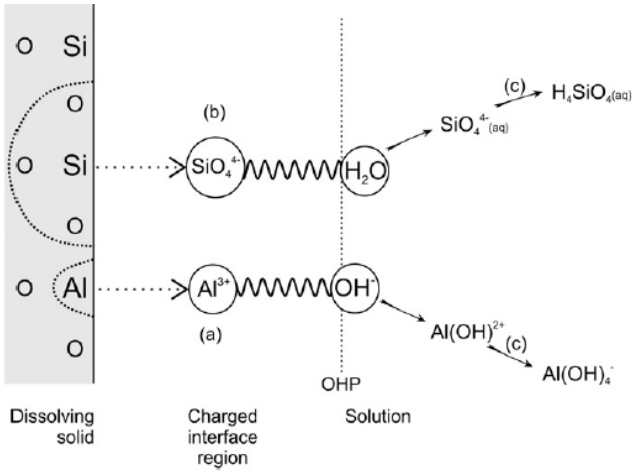

Figure 3-14. Proposed mechanism of trivalent metal containing feldspar silicate structure in alkaline condition [90].

As dissolved pyrophosphate raises the lixiviant pH to approximately 10 (Figure 3-8), hydroxide molecules may have preferably targeted metal ions first because of their lower bonding energy compared to silicon-oxygen bonding. Then, the water molecules could have targeted the weakened silicate groups by protonating the silicates to form silicic acid as proposed in the work by Crundwell [85, 86]. The silicate protonation is plausible as the pK_{a1} of silicic acid is reported to be above 9 [93-95]. In other words, the first protonation of silicic acid should be occurring at a pH less basic than pH 9.

Another SiO_4^{4-}, Fe, and Al dissolution mechanism could be ligand-promoted dissolution, which was introduced by Casey and Ludwig [96]. Dissolved pyrophosphate can be considered an active ligand that acts as a strong Lewis base, capable of switching binding sites with coordinated water or hydroxide molecules in the silicate matrix [96]. As the ligand exchange by pyrophosphate continues, the bonds between the water-metal or hydroxide molecule-metal in the silicate structure may be weakened, releasing the metal ions into the leaching solution, or complexing with pyrophosphate, such as $AlP_2O_7^-$ and $Si_2P_2O_7$ [42, 96]. This opens the possibility that the impurities in the concentrate graphite may be characterized by their "imperfect" crystal structure containing water-metal or hydroxide-metal bonds. This dissolution mechanism of ligand exchange will be further explored in the following chapters. It would be interesting to study the effect of

concentration for pyrophosphate and polyphosphate solutions, and the effect of mixing phosphoric acid and pyrophosphate on the dissolution of impurities in the graphite concentrate.

3.7 Compositional Mass Balance – Graphite Impurities

A component analysis for the graphite impurities was performed to quantify the percent leached. The initial impurity amount was quantified in ash by XRF by SGS (Table 3-10).

Table 3-10. Concentrated graphite impurity concentration after LOI by SGS

Element	Si	Al	Ca	Fe	Na	K
g/t	7386.0	6970.0	101.0	2807.0	30.0	1001.0

The pregnant leach solution concentrations were measured. Assuming the volume of lixiviant remained constant before and after leaching, the lixiviant concentration and volumes provide the mass of dissolved impurity from each sample. These values can be normalized to per gram of graphite concentrate in the leaching experiment.

For 1.0 g of graphite concentrate (GC), an elemental impurity content was calculated (Eq. 40)

$$M_{element}/_{g_{GC}} = M_{GC}(g) \times \frac{M_{element}\ (g)}{t\ of\ GC} \times \frac{t\ of\ GC}{1 \times 10^6\ g\ of\ GC} \times \frac{1\ 000\ mg\ element}{1\ g\ element} \quad (40)$$

Table 3-11 is a summary of impurity concentrations per g of graphite concentrate.

Table 3-11. Calculated impurity concentrations in 1.0 g of GC

element	Si	Al	Ca	Fe	Na	K
mg/g GC	7.4	7.0	0.1	2.8	0.1	1.0

The estimation of leached element mass within an experiment was calculated from impurity concentrations given in ppm (very close to mg/L for aqueous solutions at room temperature) and the lixiviant volume (Eq. 41).

$$M_{element}(mg) = ppm\left(\frac{mg}{L}\right) \times Volume\ of\ the\ lixiviant\ (mL) \times \frac{1\ L}{1000\ mL} \quad (41)$$

Appendix G 1 and Appendix G 2 summarize the mass of impurities in 12 mL of lixiviant at 20 ˚C and 100 ˚C.

Using the data in Table 3-11, Appendix G 1 and Appendix G 2, the weight percentages of dissolved impurities were calculated from the dissolved and initial impurity masses (Eq. 42).

$$Wt\ \%\ dissolved\ impurity = \left(1 - \frac{M_{impurity\ in\ GC}\ (mg) - M_{impurity\ in\ PLS}}{M_{impurity\ in\ GC}\ (mg)}\right) \times 100 \quad (42)$$

The weight percentages of dissolved impurities are summarized in Appendix H 1 (20 °C) and Appendix H 2 (100 °C).

Appendix H 1 and Appendix H 2 show that 1 M phosphoric acid dissolved some silicate impurities. For Si and Al, less than 20 % of the initial impurity contents in the graphite concentrate leached into the leaching solution. Phosphoric acid (1.0 M) extracted nearly 50 wt% of Fe. The temperature influenced the dissolution kinetics as the mass of dissolved impurities noticeably increased for 1.0 M phosphoric acid leaching at 100 °C.

For dissolved pyrophosphate (0.1 M $Na_4P_2O_7$) and polyphosphate (0.1 M $NaPO_3$), the extracted wt% of Si, Al and Fe are insignificant compared to phosphoric acid (1.0 M). All impurity extractions were less than 3 wt%. Sodium pyrophosphate dissolution created an alkaline solution and was a more effective SiO_4^{4-} lixiviant than polyphosphate, which was slightly acidic (near pH 6). However, polyphosphate showed superior leachability for Al and Fe at both temperatures (20 °C and 100 °C) than pyrophosphate. Compared to pyrophosphate, polyphosphate leached 200% more Al and 30% more Fe at 20 °C and leached about 140% more Al and 360% more Fe at 100 °C. Increasing the leaching temperature to 100 °C generally improved the impurity leaching for the three lixiviants tested.

3.8 Conclusions

The hypothesis that 0.1, 0.5, and 1.0 M phosphoric acid and 0.1 M of pyrophosphate or polyphosphate ($NaPO_3$) can dissolve SiO_4^{4-}, Al, Fe and K at 20 °C was confirmed. The impurity dissolution was enhanced at 100 °C. Increased phosphoric acid concentration increased the impurity extraction. The pyrophosphate and polyphosphate lixiviants achieved lower weight percent impurity extraction than 0.1 or 1 M phosphoric acid. These results suggested that a more rigorous exploration of the effect of phosphate chemistry on graphite impurity dissolution was warranted. Chapter 4 describes the identification of optimal process boundary conditions to apply the efficient “design of experiments” technique to this open problem.

4 Design of Experiment (DoE): Boundary Condition (±β) Identification

In this chapter, the determination of boundary conditions for the design of experiment is discussed. The operating variables (temperature, phosphoric acid concentration, liquid to solid ratio, leaching time, and polyphosphate concentration) were selected based on previous leaching studies performed with sulfuric acid. Sulfuric acid was deemed comparable to phosphoric acid given the polyprotic nature of it. The cost analysis between pyrophosphate and polyphosphate revealed that polyphosphate is about five times more economically viable. Polyphosphate is paired with phosphoric acid to study the synergetic effect on graphite leaching. The characterization technique solely focused on MP - AES for the leached solution. The sample preparation for MP-AES is described.

Table 4-1. Author Statement

Conceptualization, Writing (Review & Editing)	Hak Jun Oh Associate Professor Sidney Omelon
Investigation, Writing (Original Draft)	Hak Jun Oh
Methodology	Hak Jun Oh Ozan Kökkılıç (Research Associate) Associate Professor Sidney Omelon
Writing – Review & Editing	Hak Jun Oh Associate Professor Sidney Omelon

4.1 Goal

The goal is to define the most useful lowest and highest values of the leaching parameters (± β) before executing the design of experiment.

4.2 Theory

A short literature review is provided to explain the motive behind choosing the leaching parameters. The cost evaluation of sodium polyphosphate revealed that the leaching with polyphosphate is more economical than the one with pyrophosphate. A brief overview of Design of Experiment (DOE) will be provided in the current section.

4.3 Design of experiment: Response Surface Methodology (RSM) with Central Composite Design

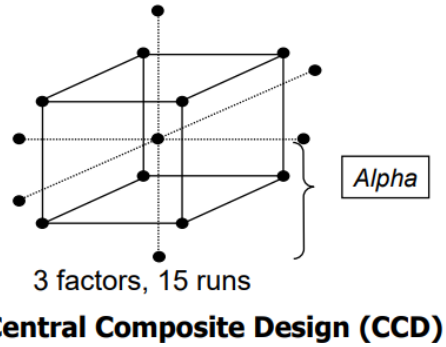

Figure 4-1. Central composite design (CCD) graphed in 3D plot [88, 97]

Response surface methodology (RSM) is a frequently used design method for optimization that has statistical and experimental aspects. It is collection of statistical and mathematical methods that can provide useful information in experiment designing, modelling, evaluation of effect of factors, and optimum condition finding [88, 97]. The main objective lies within the optimization of the response surface that is influenced by the various input parameters [88, 97].

Central composite design is a RSM design that was originally developed by Box and Wilson [88, 97]. In a central composite design, each factor has 5 levels for estimating main effects and quadratic terms. The main effects are the effects of one independent variable on the dependent variable. Quadratic terms are the factors that have an interact with themselves, resulting in a curvature in the response of interest. The number of experimental runs is dependent on the number of input factors (operating variables) as shown below.

$$\#\ of\ experimental\ runs = 2^{K\ (\#\ of\ variables\ to\ optimize)} \qquad (43)$$

Firstly, it is required that the boundaries (the lowest and highest values, ± β) of each parameter are defined. After the boundary definition, the DOE runs are designed with randomized operating conditions within the given boundaries for experimental collection of data points. The experimental results are then studied to understand the effects of each variable on the desired response and interactions between the variables. Lastly, a robust mathematical model is built to predict the optimized conditions for a desired response. The model must be validated experimentally to assess the prediction accuracy [88, 97].

4.4 Literature review of graphite leaching process conditions

In the Chapter 3, the operating variables of graphite leaching were selected without thorough examination based on the results of studies that used sulfuric acid as lixiviant [5, 22, 25]. The parameters defined in Chapter 3 will be revisited to study and select the boundaries of each operating parameters carefully. Given the polyprotic characteristic of phosphoric acid and sulfuric acid, the operating variables for the unknown phosphoric acid leaching performance will be benchmarked against sulfuric acid.

4.4.1.1 Phosphoric acid concentration

The sulfuric acid concentrations indicated by Jara & Kim [5], Thi & Hong [25], and Kaya & Canbazoğlu works was a percentage value. Due to unclear specification, the percentage concentration is assumed to be wt%. Kaya's work examined the concentration of H_2SO_4 between 5 % to 30 %, where the maximum carbon content was measured at 25 wt% H_2SO_4 [22].

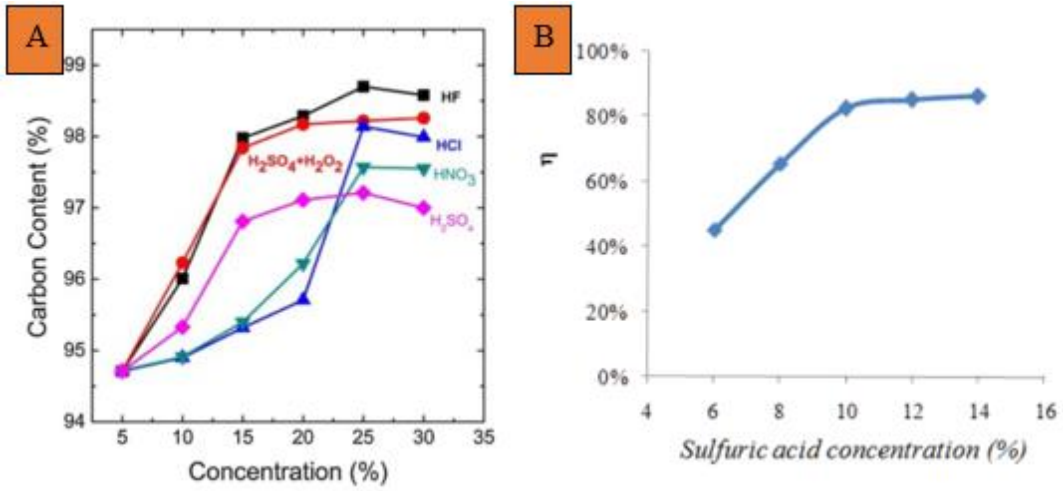

Figure 4-2. A) Effect of acid concentrations on the carbon content according to the acid kind (Liquid to solid ratio of 5:1, leaching temperature at 70 ˚C, and 90 min of leaching time) [5]. B) Effect of sulfuric acid concentration on the removal of impurities (Liquid to solid ratio of 5:1, room temperature leaching, stirring speed 200 rpm, and leaching time of 120 min) The efficiency was calculated as $(M_{before} - M_{after})/M_{before} \cdot 100)$, where M is the graphite mass [25]

Thi & Hong reported that the impurity extraction efficiency did not change significantly beyond 10 wt% H_2SO_4. One limitation of these studies is that no error bars were provided in either publication works (Figure 4-2 and Figure 4-3). The lower boundary of 10 wt% (-β) and the upper boundary of 30 wt% (+β) sulfuric acid were selected [5, 22, 25].

4.4.1.2 Leaching temperature

Jara & Kim's work did not study the effect of temperature on graphite leaching [5]. Based on the results of Kaya & Canbazoğlu and Thi & Hong, the temperature boundaries were set between 20 °C (-β) and 100 °C (+β) to investigate the effect of temperature on graphite leaching [5, 22, 25].

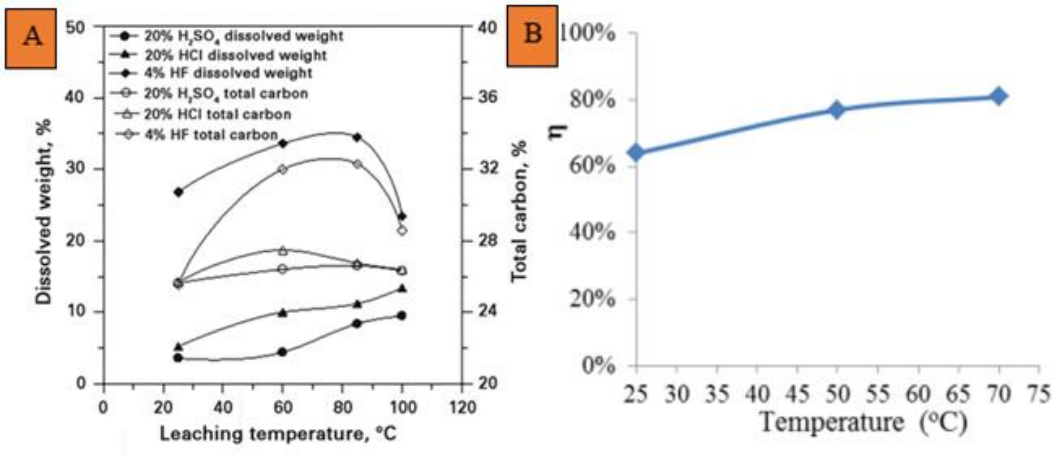

Figure 4-4. A) Effect of leaching temperature of natural graphite ore (Inebolu) (Solid to liquid ratio (w/v) = 1/10, 20 % H_2SO_4 concentration, leaching time of 60 min) [22]. B) Effect of temperature on the removal of impurities from graphite (Liquid to solid ratio 5, stirring at 200 rpm, 10 % Sulfuric acid concentration, leaching time 60 min). The efficiency was calculated as $\eta = (M_{before} - M_{after})/M_{before} \cdot 100)$, where M is the graphite mass [25]

4.4.1.3 Liquid to solid ratio

Kaya & Canbazoğlu 's work solely focused on a liquid to solid ratio of 10:1 (v:w) [22]. This information is insufficient as two boundaries are required for the central composite design. The liquid to solid ratio (v:w) was chosen to be between 3 (-β) and 7 (+β), considering Jara & Kim and Thi & Hong's results (Figure 4-5) [5, 22, 25].

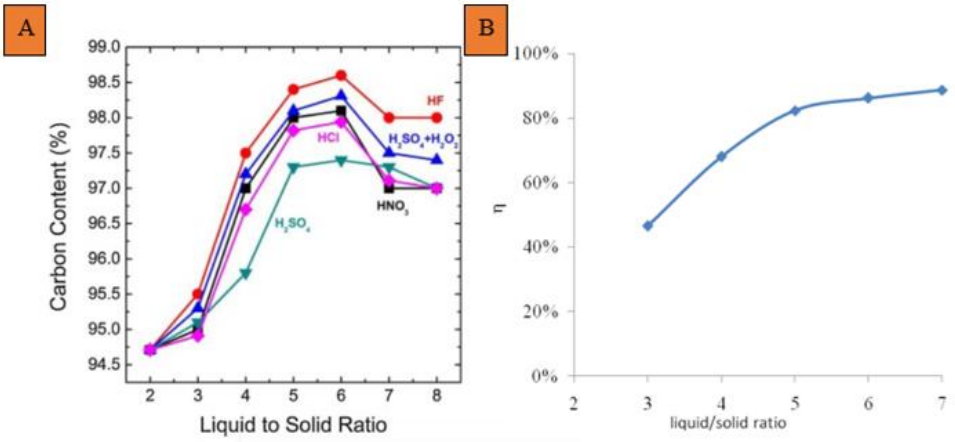

Figure 4-5.A) Effect of liquid to solid ratio of leaching solutions HF 48 %, HCl 36 %, HNO_3 70 %, H_2SO_4 98 %, and H_2O_2 30 % [5]. B) Effect of liquid to solid ratio on the removal of impurities from graphite (10% sulfuric acid, 200 rpm stirring speed, room temperature leaching, leaching, 120 min). The efficiency was calculated as $\eta = (M_{before} - M_{after})/M_{before} \cdot 100)$, where M is the graphite mass [25]

4.4.1.4 Leaching time

Kaya & Canbazoğlu investigated the leaching time between 60 – 240 min [22]. The result showed little change in the final carbon content [22]. On the other hand, Jara & Kim and Thi & Hong demonstrated that approximately 60 min of leaching marks the initiation of impurity dissolution, and little change in final carbon content was observed when the leaching time exceeded 210 min [5, 25]. For DOE, the leaching time between 60 – 300 min will be studied.

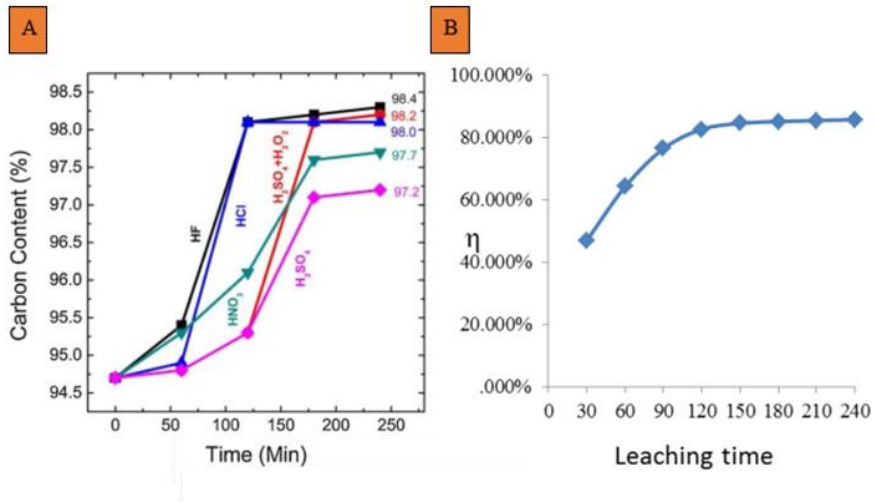

Figure 4-6. A) Effect of leaching time of leaching solutions HF 48 %, HCl 36 %, HNO_3 70 %, H_2SO_4 98 %, and H_2O_2 30 %, 1 to 5 solid to liquid ratio, leaching temperature 70 ˚C [5]. B) Effect of leaching time on impurity dissolution: 5:1 liquid to solid ratio, 200 rpm stirring speed, 10% sulfuric acid, room temperature. $\eta = (M_{before} - M_{after})/M_{before} \cdot 100)$, where M is the graphite mass [25]

The process operating variables reviewed for this study are summarized in Table 4-2. The highest and lowest values are assumed to be candidate ±β values for this study.

Table 4-2. Tested ranges of DOE ±β operating variables by previous studies using sulfuric acid (H_2SO_4)

Ref.	Leaching solution	H_2SO_4. (%)		Liquid to solid ratio		Temperature (˚C)		Leaching time (min)	
		Low (-β)	High (+β)	Low (-β)	High (+β)	Low (-β)	High (+β)	Low (-β)	High (+β)
[14]	H_2SO_4 (20 %)	10	20	10 *(v/w)*	10 *(v/w)*	25	100	60	240
[15]	H_2SO_4 (10 %) +Alkali roasting	6	14	3	7	25	70	30	240
[5]	H_2SO_4 (10 %) + H_2O_2 (30 %) + NaOH roasting (Path A) + HCl (18 %) (path B) + HF (5 %) (path C)	10	30	3 *(w/w)*	8 *(w/w)*	25	25	60	240

Considering the tested ranges of operating variables in the previous studies, the operating parameter ranges were selected, and are summarized in the Table 4-3.

Table 4-3. Selected DOE ±β values for operating variables

H_3PO_4 (mol/L)		Liquid to solid ratio (v/w)		Temperature (˚C)		Leaching time (min)		PolyP (mol/L)	
Low (-β)	High (+β)	Low (-β)	High (+β)	Low (-β)	High (+β)	Low (-β)	High (+β)	Low (-β)	High (+β)
1	5	3	7	RT	100	60	300	0	2.5

4.5 Polyprotic acid deprotonation behavior

As discussed in Section 3.6.2.1, sulfuric acid and phosphoric acid share the polyprotic characteristic. Acidic leaching conditions considered in this study (pH < 4), the single deprotonated species ($H_2PO_4^-$) and the neutral phosphoric acid species ($H_3PO_4^0$) are predominant (Figure 4-7).

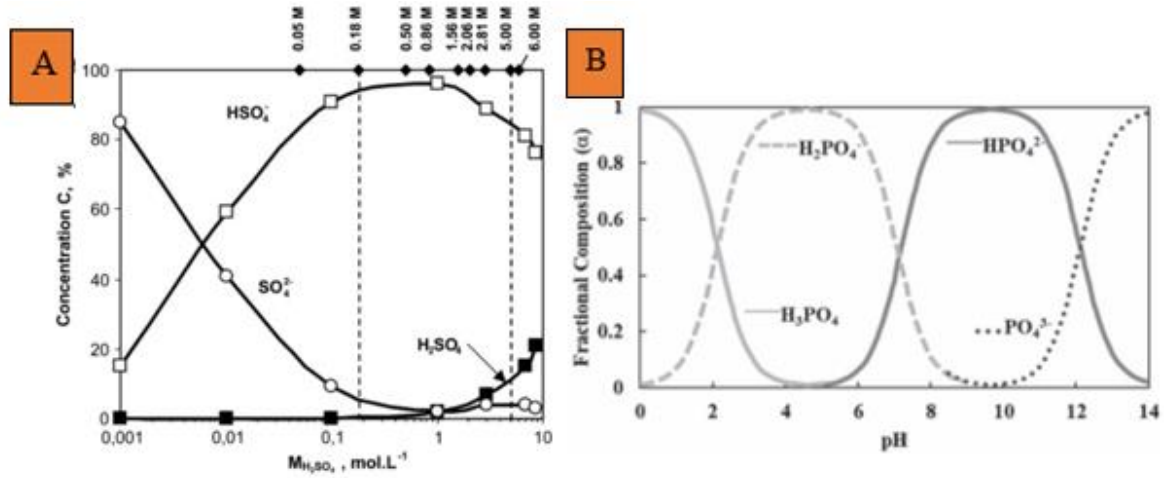

Figure 4-7. A) Sulfuric acid deprotonation according to the concentration (mol/L) [98]. B) Phosphoric acid deprotonation according to the pH. 25 °C is assumed as the temperature was not indicated [41]

The sulfuric acid concentrations listed in Table 4-2 are assumed to be in wt%. Therefore, a single deprotonation of sulfuric acid (HSO_4^-) is similarly expected to be dominant for the reported leaching experiments (Figure 4-7) (A). The conversion from wt% to mol/L is described in Eq. 44.

$$wt\%_{H_2SO_4}\left(\frac{g}{100\ g\ solution}\right)\times\frac{1}{M_{H_2SO_4}}\left(\frac{mol}{g}\right)\times\rho_{H_2SO_4}\left(\frac{g_{solution}}{L_{solution}}\right)=mol/L \qquad (44)$$

The demonstrated calculation method was used to find the required concentration of phosphoric acid in mol/L (Eq. 45).

$$C_{H_2SO_4}\left(\frac{mol}{L}\right)\times\frac{2\ mol_{H^+}}{1\ mol_{H_2SO_4}}\times\frac{x\ mol_{H_3PO_4}}{3\ mol_{H^+}}=\frac{mol}{L} \qquad (45)$$

Using Eq. 44 and Eq. 45, the lowest and highest concentration of phosphoric acid were [1.2 – 3.7] mol/L using [10 – 30] wt% sulfuric acid concentrations. DOE boundaries were set at lower and higher concentrations to include the calculated phosphoric acid concentrations (Table 4-3).

4.6 Cost evaluation of pyrophosphate vs polyphosphate

Before further proceeding in the leaching study, a reagent cost estimation was undertaken to evaluate the economical feasibility of using pyrophosphate or polyphosphate as a condensed phosphate lixiviant. The cost of the pyrophosphate, sold as $Na_4P_2O_7 \cdot 10H_2O$ (446.06 g/mol), was compared with the cost of sodium polyphosphate, sold as an often unknown a size distribution of $(NaPO_3)_n$ polymers (102 g/mol), was normalized to a per $NaPO_3$ unit. The cost estimate summary is summarized in Table 4-4 and Table 4-5.

Table 4-4. Summary of sodium pyrophosphate decahydrates purchase costs

Supplier	Purity (%)	$/kg ($CAD)	Avg.$/kg ($CAD)	mol $NaPO_3$ per kg	$CAD per mole $NaPO_3$
Avantor Performance Materials US [99]	99.0 ~ 103.0	$74	$118	4.5	$26
Fisher Chemical [100]	99.0 ~ 103.0	$67			
Sigma-Aldrich Canada Co. [101]	> 99	$213			

Table 4-5. Summary of sodium polyphosphate $NaPO_3$-normalized purchase cost

Supplier	Purity (%)	$/kg ($CAD)	Avg. $/kg ($CAD)	Mol $NaPO_3$ per kg	$CAD per mole $NaPO_3$
Sigma-Aldrich Canada Co.[101]	> 68	$40	$50	9.8	$5.10
Thermo Fisher Scientific[100]	65 - 70	$59			

The calculation was made to find the cost of normalized to mol of sodium polyphosphate monomer ($NaPO_3$). Based on the values found in Table 4-4 and Table 24, sodium polyphosphate is approximately 5 times less expensive per unit $NaPO_3$.

4.7 Method – Determining ±β for sodium polyphosphate and its effect on MP-AES results

Evidence for sodium polyphosphate use as a lixiviant was not identified. Assessment of the upper boundary (+β) for polyphosphate concentration is described in this section. No replicates were done because MP-AES results are provided as a mean of three measurements.

4.7.1 Determination of the Upper Boundary (+β) for the Polyphosphate Concentration.

4.7.1.1 Undigested Leached Samples

The sodium polyphosphate was reported to be 1 000 g/L at 20 °C, [100, 101]. A practical upper boundary (+β) for polyphosphate concentration was not known. Therefore, the effect of polyphosphate concentration on concentrated graphite leaching was examined considering four points up to the maximum solubility (1 000 g/L at 20 °C).

Four graphite samples (1.0 ± 0.01 g) were leached for an hour using 1 M H_3PO_4 solutions containing four different polyphosphate concentrations: 250, 500, 750 and 1 000 g $NaPO_3$/L at room temperature. -β of liquid to solid ratio was selected (3 mL). The slurries were vacuum-filtered, and syringe-filtered to separate the solid from liquid. The concentrations of the impurities in the pregnant leach solutions (PLS) were diluted 10 times with 2 %v/v HNO_3. The lixiviant ion concentrations of Fe^{3+}, SiO_4^{4-}, Ca^{2+}, Al^{3+}, and K^+, were measured with MP-AES (Table 4-6).

Table 4-6. Lixiviant iron, silicate, calcium, aluminum, and potassium concentrations in the pregnant leach solutions

Concentration of $NaPO_3$ (Max solubility 1000 g/L) (g/L)	Fe (ppm) 371.993 nm	Si (ppm) 251.611 nm	Ca (ppm) 396.847 nm	Al (ppm) 394.401 nm	K (ppm) 769.897 nm
250	6.1	31	17.8	22.4	43.3
500	2.9	0	6.9	13.6	121
750	2.2	0	3.3	8.0	211
1000	2.0	0	3.7	7.4	183

The lowest polyphosphate concentration (250 g/L) resulted in the highest dissolved impurity concentrations of SiO_4^{4-}, Ca^{2+}, Fe^{3+}, and Al^{3+} in the PLS. Increasing polyphosphate concentration generated different impurity ion PLS concentrations. Assuming that a higher polyphosphate concentration would increase its leaching power, it was surprising that only the monovalent ion (K^+) increased in concentration from 250-750 g/L. As polyphosphate is a known effective

multivalent ion chelator, it is possible that polyphosphate ion chelation may change the emission energy of the dissolved ions as measured by MP-AES [89, 102].

4.7.1.2 Effect of PLS digestion on MP-AES results

The effect of polyphosphate concentration on MP-AES results was examined. No repetition was done. However, the measured concentrations were provided after three repeats by MP-AES. To break down the polyphosphates into orthophosphates, an acidic hydrolytic degradation was performed on the PLS (Eq. 4-1)

$$[PO_3^-]_n + H_2O \rightarrow [PO_3^-]_{n-1} + HPO_4^{2-} + H^+ \quad (46)$$

A 1:1 v/v ratio of filtered PLS was mixed with 2 M HCl in 15 mL sealable Teflon tubes (VWR). The solutions were digested at 100 °C for 30 min with a dry bath (Dry bath/block heater, ThermoFisher). The digestion temperature was selected based on the previous works by Omelon and coworkers, and the concentration of HCl and time were selected arbitrarily in view of the substantial concentrations of the tested polyphosphate [103, 104]. The goal of this digestion was to hydrolytically break down the polyphosphate chains into orthophosphate ions, which have less chelating power than polyphosphate.

The digested PLS was diluted five times with 2 % v/v HNO_3. The MP-AES results are summarized in Table 4-7.

Table 4-7. PLS dissolved impurity ion concentrations measured after 30 minute digestion of (2 M HCl, 100 °C & 1:1 volume ratio of PLS and HCl)

$NaPO_3$ concentration (g/L)	Fe^{3+} (ppm)	Si (ppm)	Ca (ppm)	Al (ppm)	K (ppm)
250	10.4	11	23.8	25.8	49.6
500L	9.8	13.8	24.6	21.2	36.8
750	6.8	0	18.2	26.2	99.8
1000	5.8	0	11	23.4	263

The measured dissolved impurity ions in the PLS increased after PLS digestion. This result supports the hypothesis that multivalent ions were concealed from detection by MP-AES due to their chelation with polyphosphates. Considering the decreased impurity concentrations observed for 750-1000 g/L $NaPO_3$ concentrations, digestion for 30 min was assessed to be insufficient to completely liberate the chelated ions.

A second PLS digestion was undertaken with a diluted PLS and a longer digestion time. The PLS was diluted 10 times with reverse osmosis (RO) water. The diluted PLS was diluted 10 times with 2% v/v HNO_3 The dilution factor for MP-AES measurement was 200x. The digestion results are summarized in Table 4-8.

Table 4-8. PLS dissolved impurity ion concentrations measured after 60 min of digestion (2 M HCl, 100 °C & 1:1 volume ratio of PLS and HCl)

[$NaPO_3$] (Max sol. 1000 g/L) (g/L)	Fe^{3+} (ppm)	Si (ppm)	Ca (ppm)	Al (ppm)	K (ppm)
250	0	136	108	8	30
500	0	146	118	12	40
750	0	138	104	12	54
1000	0	158	134	16	56

Increased digestion time and acidity generated a proportional relationship between polyphosphate concentration the PLS impurity ion concentrations $SiO_4^{4-}$and Ca^{2+}. The measured Al^{3+} and K^+ concentrations decreased with increasing polyphosphate concentration compared to the 30 min digestion result. This result may be due to ion-pairing of these multivalent cations with the higher concentration of inorganic orthophosphates which are generated when polyphosphate chains are hydrolytically degraded. The Fe concentrations were below the detection limit.

There are many possible sources of error in this measurement of dissolved impurities in the lixiviant. Matrix – a term to describe the background electrolyte in a solution - dissimilarity between the analyte and the solutions used to generate the calibration curve may result in erroneous measurements; this is called the "matrix effect" [105]. The calibration standards will need to be adjusted to change the background electrolyte matrix composition for future experiments. Another possible mechanism for reduced cation concentration is by ion pairing with orthophosphate ions. The ion pairing could probably shift or reduce the measured wavelength and/or energy for these cations. The current result also indirectly suggests that the previous MP-AES measurements are questionable.

4.7.1.3 Re-Evaluation of Maximum Sodium Polyphosphate Concentration

Tests of impurity leaching from concentrated graphite with 250, 500, 750, or 1 000 g sodium polyphosphate/mL were undertaken in Sections 4.7.1.1-4.7.1.2 to determine its upper

boundary (+β) concentration. The slow process of sodium polyphosphate dissolution also generated a polyphosphate gel (Figure 4-8). The solution was decanted from the gel. This means that the actual polyphosphate concentrations were lower than the calculated polyphosphate concentrations.

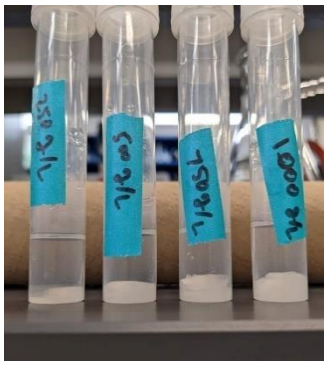

Figure 4-8. Incomplete dissolution of sodium polyphosphate at different (labeled) concentrations) and hydrogel formation in 1 M phosphoric acid at room temperature.

A short test was performed to evaluate the practicality of a +β sodium polyphosphate value of 1000 g/L. The published solubility of sodium polyphosphate in water is 1 g/mL at room temperature [100]. This maximum solubility in water was tested for 1 M phosphoric acid. 10 g of sodium polyphosphate was mixed with 10 mL of 1 M phosphoric acid in a 100 mL beaker with a stir-bar. The mixed was stirred for 3 h. Similar to the previous observation, a sodium polyphosphate gel layer remained undissolved at the bottom of the beaker.

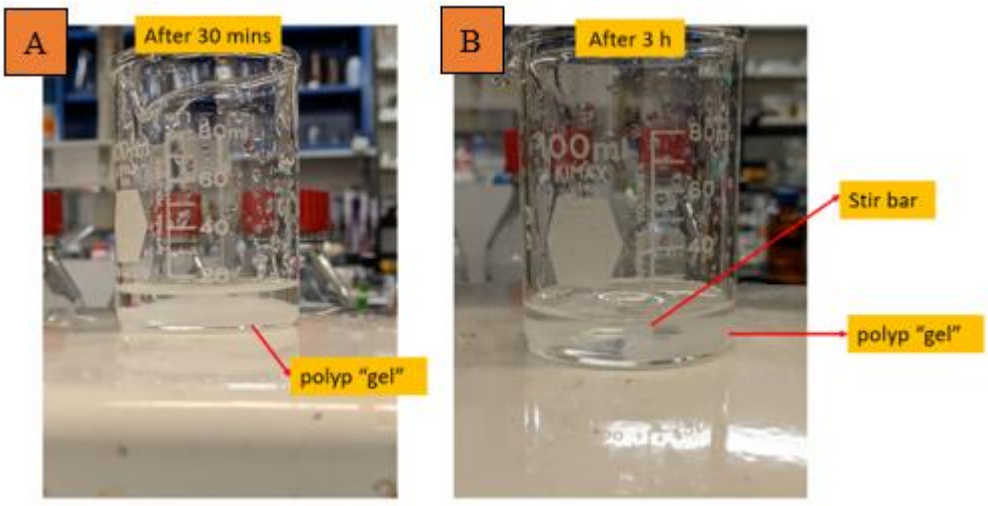

Figure 4-9. 10 g sodium polyphosphate in 10 mL 1 M H_3PO_4 shows gel accumulation at the beaker bottom after (A) 30 min and (B) 3 h of mixing at room temperature

Considering the slow dissolution rate of sodium polyphosphate, 250 g/L was selected for the +β value for sodium polyphosphate. Four sodium polyphosphate concentrations were selected for the DoE: 50, 100, 200, and 250 g/L.

The upper boundary (+β) for the molar concentration of polyphosphate was calculated Eq. 47.

$$[NaPO_3](\frac{g}{L}) \times \frac{1}{M_{NaPO_3}}(\frac{mol}{g}) = [NaPO_3](\frac{mol}{L}) \qquad (47)$$

4.7.1.4 Rebuilding the calibration standards for MP-AES and studying the effect of 60 min digestion on spiked MP-AES results (no repetition)

The matrix for the Fe, Si, Al, K, and Ca calibration standards for 2.5, 5, and 10 ppm was adjusted to account for phosphoric acid and polyphosphate contents. Mixtures of elements for each concentration level were prepared. Element standard solutions were pipetted into 50 mL tubes to create the desired final concentrations. 10 mL of a digestion solution without impurity elements was added to the standards. The simulated digestion solution was 5 mL of 1 M phosphoric acid with 50 g/L sodium polyphosphate and 5 mL of 2 M HCl hydrochloric acid. The lowest sodium polyphosphate concentration was selected as one matrix for all experiments RO water was added to make a final volume of 50 mL

The effect of polyphosphate concentration on leaching impurities from concentrated graphite was examined at 50, 100, 200, and 250 g/L $NaPO_3$. For this set of experiments, the lower boundaries (-β) for phosphoric acid concentration, liquid to solid ratio, temperature, and leaching time (Table 4-3) were used to survey the sodium polyphosphate concentrations to identify its the upper boundary (+β). Four graphite samples (2.0 ± 0.01 g/3 mL lixiviant) were leached for one hour with 1 M H_3PO_4 mixed with 50, 100, 200, or 250 g/L sodium polyphosphate).

After leaching, the slurry was vacuum-filtered and syringe-filtered. The filtered PLS was divided into two groups for analysis: undigested samples and digested samples. Both groups were subdivided into two subsequent groups: spiked and un-spiked groups. Spiking is the addition of a known amount of an analyte to a sample, in order to confirm the analytical method. The spiked group samples were mixed with a small (0.06 uL) volume of 1 000 ppm element standards in sealable 15 mL Teflon tubes (VWR, 76437-110) to increase the total solution element concentration by 20 ppm. Spiked and unspiked undigested samples were diluted 10x with RO water. Spiked and unspiked digested samples were digested at 1:1 vol/vol with 2 M HCl for 60

min at 100 °C. After digestion, all sample groups were diluted 5x with RO water for a total sample dilution factor of 10x. The samples were not diluted with 2% v/v HNO_3 as the prepared solutions were adequately acidified with HCl. The concentrations of the different elements as a function of polyphosphate concentration for spiked and unspiked samples are provided in Figure 4-10.

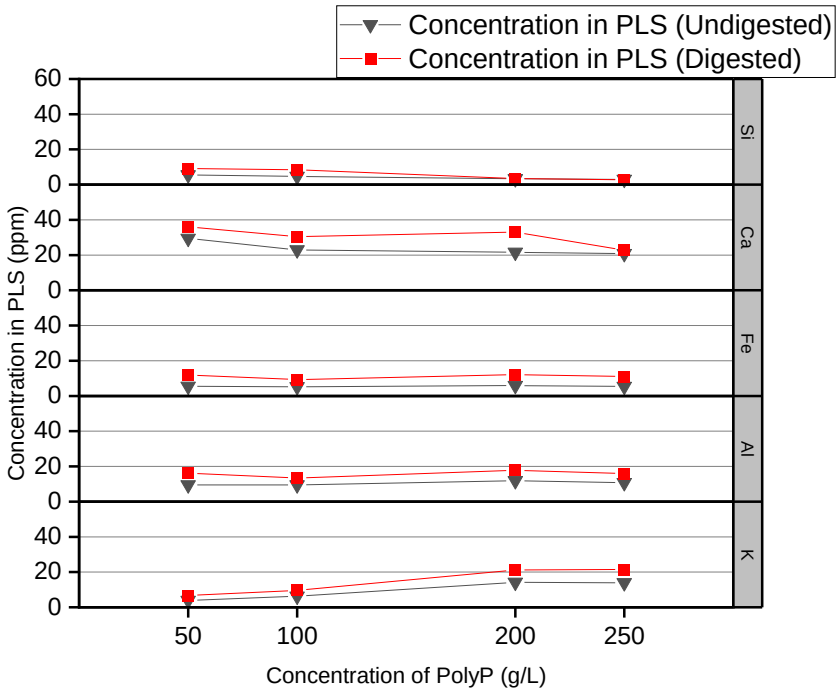

Figure 4-10. The effect of 2 M HCl digestion (1:1 vol/vol, 60 min) on the measured graphite impurity concentrations in the undigested (black triangles) and digested (red squares) PLS.

Figure 4-10 shows an increase in measured impurity concentrations after 60 min of PLS digestion. Polyphosphate hydrolytic degradation may reduce the fraction of chelated multivalent cation ions. The effect of PLS digestion on Ca^{2+} at 250 g/L polyphosphate and all silicon samples was less than for the other groups.

The spiking results of undigested samples is provided in Figure 4-11 and Appendix I 1.

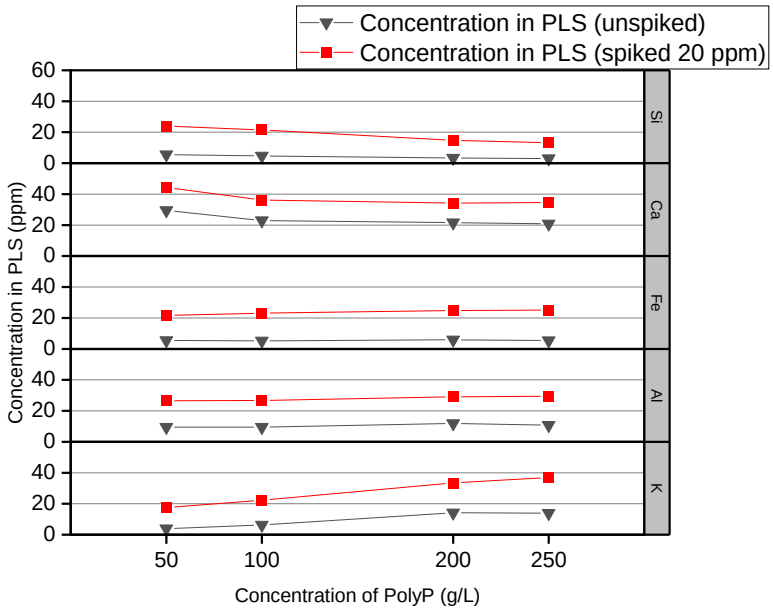

Figure 4-11. Spiking results without PLS digestion

The spiking recovery was calculated using Eq. 48, where the spiking solution concentration is 20 ppm.

$$\%\ Spike\ Recovery = \frac{C_{spiked\ solution} + C_{unspiked\ solution}}{C_{spiking}} \times 100 \qquad (48)$$

The spiking recovery rate varied between 51% and 115% without PLS digestion.

The measured impurity element concentrations responded in one of three ways to increased polyphosphate concentration: Si and Ca generally decreased, Fe and Al concentrations were not strongly affected, and K concentrations increased. Both spiked and unspiked Si and Ca concentrations decreased with increasing polyphosphate concentration. The decreased Ca concentration measurement may be due to their chelation with polyphosphates [106-109]. The decreased Si concentration could probably be due to concealment by phosphorus compounds. The Fe, Al, and K concentrations generally increased with increasing polyphosphate concentration. Increased concentrations of Fe and Al could be due to polyphosphate's preferential binding to divalent ions. Hence, trivalent ions are less likely to be affected by polyphosphate chelation. [110, 111]. PLS K concentration generally increased with increasing polyphosphate concentration. Polyphosphate may be an effective lixiviant for kaolinite, which may be a K impurity mineral. The measured K concentration may also not be inhibited by complexation with polyphosphate. The

numerical complexation measure for ion pair complex dissociation is the pK_d of potassium has a small pK_d with orthophosphate and tripolyphosphate [106].

The digested, spiked and unspiked PLS impurity ion concentrations are provided in Figure 4-12 and Appendix I 3. Spiking is a method of adding a known concentration of analyte to a matrix to assess the validity and quality of the sample test results [112].

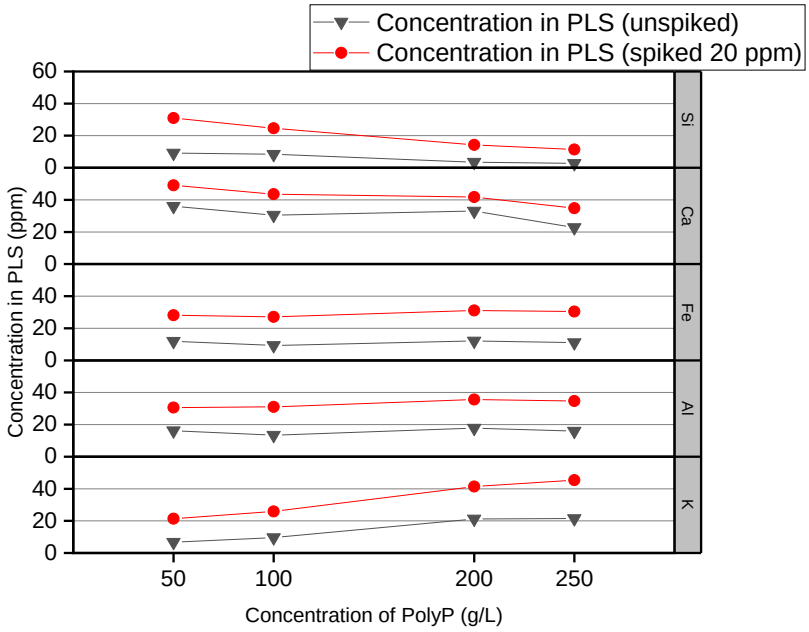

Figure 4-12. The result of spiked and un-spiked samples with 2 M HCl, 1 h digestion

The spiking recovery rate varied between 43% to 120% with acid digestion. Similar to the measured PLS Si and Ca concentrations without digestion there were three general responses to increased polyphosphate concentration. Si and Ca concentrations decreased with increased polyphosphate concentration. Fe and Al concentrations did not change dramatically. 50 g/L of polyphosphate in the lixiviant yielded highest concentrations for Fe and Al. The K concentration increased with increased polyphosphate concentration from 50 to 200 g/L, but the trend was inconclusive between 200 – 250 g/L. In summary, digesting PLS resulted in higher impurity ion concentrations.

4.7.1.5 Testing the effect of polyphosphate and phosphoric acid on element emission spectra measured with MP-AES

The experiments in Section 4.7.1.4 dissolved measurable Fe concentrations, possible because smaller lixiviant polyP concentrations did not shift the Fe emission spectrum as far as for

the higher polyP concentrations (Section 4.7.1.2) [89]. High ionic strength solutions could cause background shift interference, leading to measured wavelength variation [113, 114]. Concentrations measured for different emission spectrum energies attributed to each impurity element are presented in Appendix J 1.

From Appendix J 1, the matrix effect caused the measured element concentrations to vary, depending on the measured wavelength. MP-AES measurements of Ca at 393.666 nm and 422.673 nm were not possible with the polyP - orthophosphate matrix. All three Ca wavelengths were detected with HNO_3 matrix. Fe concentrations measured in the HNO_3 matrix at 371.993 nm yielded the highest concentrations, while the highest Fe concentrations in a polyP and phosphoric acid matrix concentrations were measured at 385.991 nm.

Dissolved phosphate was observed to affect the result of the spectroscopic concentration measurements [107, 115]. Anions in the matrix, such as SO_4^{2-} and PO_4^{3} , may react with analytes to produce species of low volatility in the plasma and could reduce the measured ion/atom population of the analyte [89]. The measured sample and the calibration curve need to share the same matrix as the accuracy of the instrument is reduced when the sample matrix is not the same as the calibration solutions [105]. It would be worthwhile to further study the matrix effect, and possibly redo the MP-AES measurements.

4.8 Conclusions

This chapter identified the operating condition boundaries for the DoE to optimize graphite impurity leaching with phosphoric acid and sodium polyP. A two-level characteristic of central composite design requires definition of the lowest (-β) and the highest (+β) variable values to define the DoE experiment. Sulfuric acid as a graphite impurity lixiviant was reviewed as a proxy for phosphoric acid because of its polyprotic characteristic. Sodium polyP was estimated to be approximately five times more economical than sodium pyrophosphate. A sodium polyP concentration range of 0 to 250 g/L was selected to study its possible synergetic leaching effect with phosphoric acid. Spiking recovery varied. In Chapter 5, the impurities in the natural graphite concentrate are characterized, and the dissolution mechanisms of these impurities in presence of phosphoric acid and polyP are proposed.

5 Impurity Characterization Before & After Leaching, & Possible Dissolution Mechanisms

The dissolution mechanisms of silicate impurities in the graphite concentrate by leaching with polyphosphate and phosphoric acid will be discussed in this chapter. Section 2.5 included an XRD characterization of the crystalline phases in the natural graphite concentrate [68]. Kaolinite, an aluminosilicate, was selected as the major crystalline impurity. Three mechanisms are proposed to describe the nature of kaolinite dissolution with phosphoric acid and polyphosphate.

Table 5-1. Author Statement

Conceptualization, Methodology, Writing (Review & Editing)	Hak Jun Oh Associate Professor Sidney Omelon
Investigation	Hak Jun Oh
Methodology	Hak Jun Oh Associate Professor Sidney Omelon
Writing – Original Draft	Hak Jun Oh

5.1 Goal

This chapter evaluates XRD data from the graphite concentrate and leached samples produced in Section 4.7.1.4 Possible dissolution mechanisms for kaolinite ($Al_2(Si_2O_5)(OH)_4$), and assumed minor pyritic (FeS_x) impurities in the natural graphite concentrate are proposed and discussed.

5.2 Crystalline impurity phase identification using x-ray diffraction (XRD)

The XRD results from Section 2.5.3 indicate that the impurity in the graphite concentrate is an Al containing silicate mineral as three identified crystalline impurities were all aluminosilicates as shown in Figure 2-7 and Figure 2-8. Kaolinite ($Al_2Si_2O_5(OH)_4$) originates from parental minerals such as feldspars (aluminosilicate containing K, Na and Ca) and muscovite (aluminosilicate containing K and F) [72]. This may explain the dissolved K and Ca in the PLS reported in Section 3.6.

Kaolinite will be considered as the sole impurity in the natural graphite concentrate because it is the most representative and simplest aluminosilicate structure [77, 78].

The dissolved iron in the PLS could originate from a non-detectable fraction of pyritic mineral (FeS_x), although the possibilities of aluminosilicate that contains Fe should not be discarded [79, 80]. The dissolution mechanism is hypothesized to be a compound of three different

mechanisms that occurs simultaneously: proton-assisted dissolution, polyphosphate-assisted dissolution, and phosphate-assisted dissolution.

5.3 Proton-assisted dissolution mechanism

Considering the acidic leaching condition, the dissolution of aluminosilicate could have occurred as described in Figure 5-1 with protons (H^+).

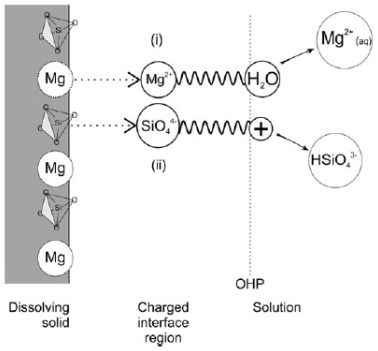

Figure 5-1. Mechanism for the dissolution of orthosilicate minerals and metal ions in acidic solutions by complexing with protons and water molecules. An example of Mg containing silicate is shown in the figure. OHP: Outer Helmholtz Plane [85]

According to Crundwell, metal ions could interact with H_2O molecules and dissolve, while silicates can be protonated [85]. May, Hradil, and Polzer and Hem proposed a similar silicate protonoation dissolution mechanism tha as Crundwell (Eq. 49) [116-118].

$$Al_2Si_2O_5(OH)_4 + 6H^+ = \ 2Al^{3+} + 2H_4SiO_4 + H_2O \qquad (49)$$

5.4 Polyphosphate-assisted dissolution: Cleavage of metal ions by chelation, or ligand exchange/Lewis acid-base interaction

Sodium polyphosphate ($Na(PO_3)_n$) is a molecular chain of condensed phosphate ions that is characterized by P-O-P bonds formed by dehydration/condensation [119].

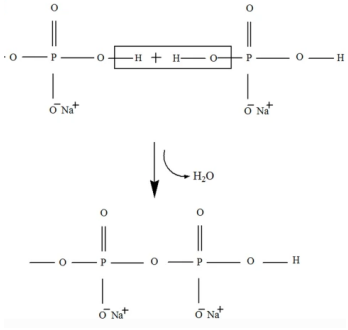

Figure 5-2. Formation of polyphosphate chain by the condensation reaction [119]

Polyphosphate was reported to chelate multivalent metal ions [104, 106, 108, 109, 120, 121]. The chelation mechanism was described as oxygen atoms from p-subunits forming stable complexes with multivalent metal ions in specific binding sites (Figure 5-3) [106].

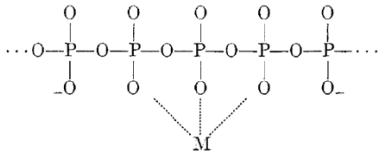

Figure 5-3. Chelation mechanism of polyphosphate chain with a metal ion [106]

The alkaline earth metals have been observed to bind to both oxygen atoms of p-subunits (middle chains in polyphosphates), and end-of-chain oxygen atoms [108]. For Al^{3+} ions, it has been reported to bind to both the end-of-chain oxygens and subunits of the polyphosphate chain [108]. At the low working pH of graphite leaching (~pH 1), the sequestration of metal ions may not be as effective due to charge neutralization by protons (H^+) (Figure 5-4).

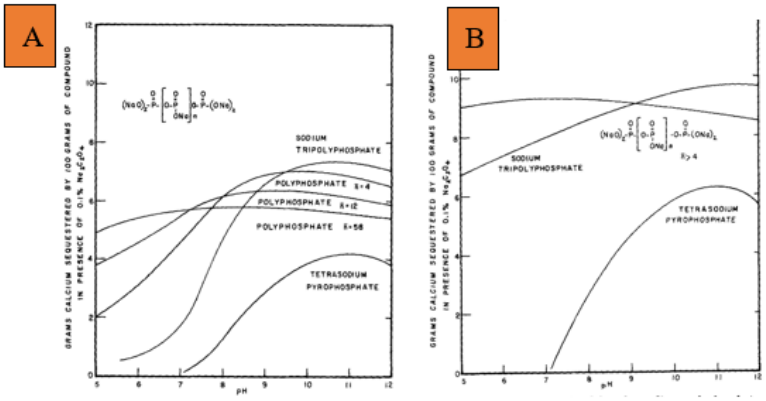

Figure 5-4. Calcium sequestration by polyphosphate at 25 °C (A), and 60 °C (B) [120]

The lixiviant was prepared by dissolving sodium polyphosphate in phosphoric acid. Na^+ ions are also charge neutralizers, and competitors for polyphosphate bond formation with multivalent ions [108]. Na^+ ions may have been more effective in blocking multivalent ion sequestration because protons are charge neutralizers, whereas Na^+ ions would compete for the available binding sites with divalent ions [108].

The P-O-P bond of polyphosphates is known to undergo spontaneous hydrolysis by reaction with water molecules, resulting in orthophosphates as shown in Figure 5-5 [111, 122], as well as shorter-

chain polyphosphates. Temperature, pH extremes, dilution, and increased metal-ion concentrations have been reported to accelerate the polyphosphate chain hydrolysis [111, 123, 124].

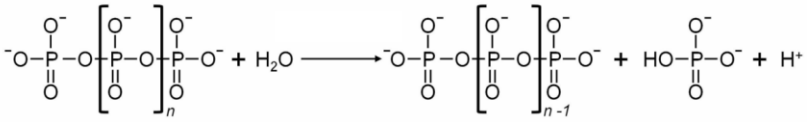

Figure 5-5. Schematic representation of polyphosphate hydrolysis. Adapted from [125]

Considering the hydrolysis mechanism of polyphosphate and the presence of hydroxide in the aluminosilicate structure, one could suggest an indirect hydrolysis mechanism in acidic conditions. The lattice structure of Kaolinite is described in Figure 5-6.

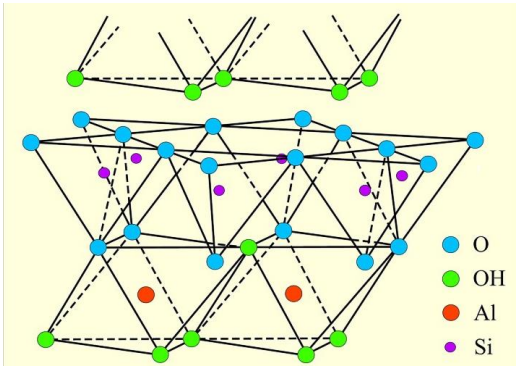

Figure 5-6. Lattice structure of kaolinite in 3D [126]

To simplify the complex structure of kaolinite, a 2D representation is described in Figure 5-11 and Figure 5-12.

A mechanism could be suggested for the aluminum dissolution from the kaolinite: The aluminum in kaolinite is in hydroxyl state [127, 128]. Aluminum is likely to be in hydroxyl state at neutral condition (Figure 5-7) [129].

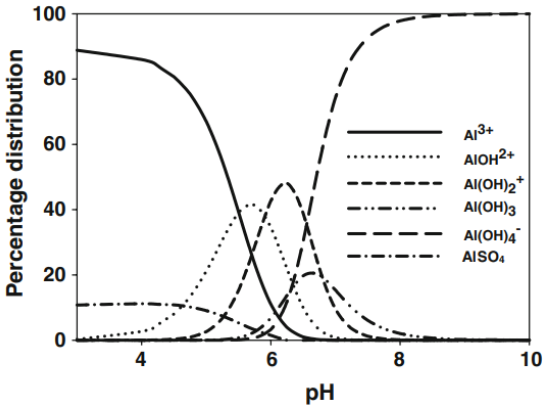

Figure 5-7. Al speciation over a range of pH values [129]

The dissolution mechanism initiating at the basal and edge hydroxyl groups (OH^-) of the aluminol layer of kaolinite is presumed. The dissolution of aluminol layer was prioritized over the siloxane layer in two previous studies [130, 131]. It is noted that the proposed dissolution mechanisms are built upon the framework of kaolinite dissolution concepts established by previous studies [92, 117, 130-134]. Edge hydroxyl groups being the dissolution initiation point is plausible as it is one of three reported reactive sites in kaolinite: Edge hydroxyl groups, basal hydroxyl sites, and Al-O-Si bridging sites [128].

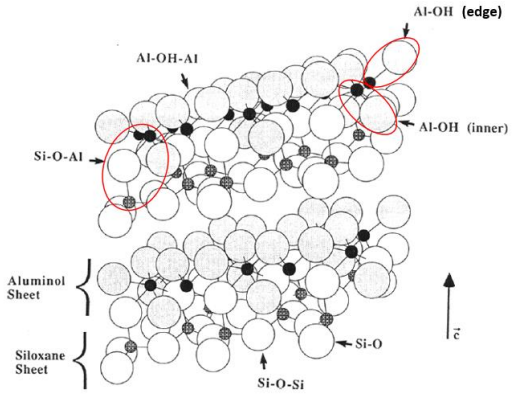

Figure 5-8. Kaolinite crystal structure with reactive sites indicated [128]

Al = solid; Si = hatched; O = open; OH = shaded

The interaction between the surface charge of kaolinite and polyphosphate chains should be discussed to support the hypothesis of metal chelation by polyphosphate chains. To do so, the concept of surface charge needs to be understood. The concept of point of zero charge is often confused and in multiple literatures, it's used as a compound terminology to describe point of zero

net proton charge (PZNPC), point of zero net charge (PZNC), and point of zero charge (PZC) [135, 136]. The PZNPC is the pH at which the charge due to protonation and deprotonation is zero [136]. The main difference between PZNC and PZC arise from the charge associated with adsorbed solute ions immobilized in interfaces [136]. For PZNC, solely the intrinsic charge (proton surface charge and permanent structural charge) is considered, while PNC considers the charge from the adsorbed solute ions as well [136]. Therefore, pH_{pzc} is the pH at which the surface charge of sorbent is neutral. Below the pH_{pzc}, the surface of sorbent is positively charged, and the opposite can be said above the pH_{pzc} [137, 138].

Kaolinite is known to have a localized negative charge on the siloxane layer due to isomorphous substitution of Si^{4+} by Al^{3+}, while the edge hydroxyl groups have variable charges due to protonation/deprotonation [131, 139]. The pH_{pzc} of overall kaolinite is reported to be approximately 3 at room temperature, and it varies with the increase in temperature as de-hydroxylation occurs at high temperatures (>500 °C) as shown in Figure 5-9 [127, 140].

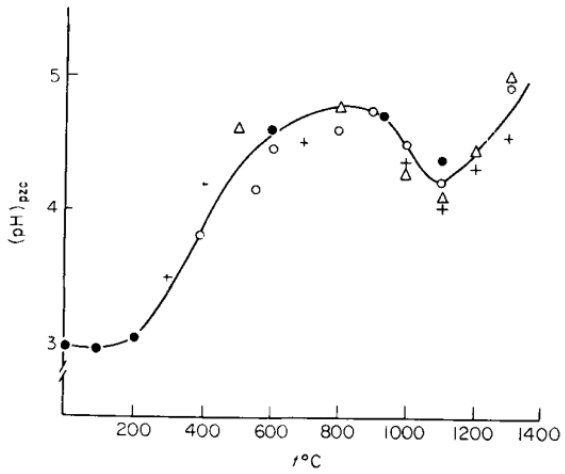

Figure 5-9. The pHpzc curve according to temperature (°C) for kaolinite [127]

The theoretical pH value of 1 M H_3PO_4 is approximately 1. This pH is lower than the theoretical pH_{pzc} value of kaolinite (~3) and the kaolinite structure could be presumed to be positively charged. There are studies that reported higher pH_{pzc} for kaolinite [131, 133, 141-143]. Therefore, the hydroxyl (OH^-) edge groups of kaolinite are presumed to be positively charged and attract anions in the solution. The protonation of aluminum-hydroxide groups (Al-OH) is a known phenomenon, occurring in the pH range between 4 – 6 (Figure 5-10) [78, 131, 134, 142-148].

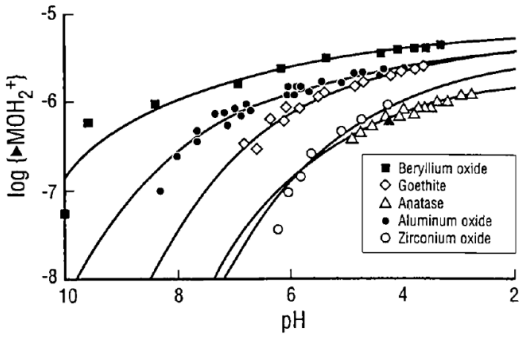

Figure 5-10. Surface protonation for a few oxides. Symbols correspond to titration curves at ionic strength of 0.1 M (except hematite). The concentrations of protonated sites (MOH_2^+) are given in moles/m^2 [147]

Along with the protonation of hydroxyl edge groups, the integrity of a metal-hydroxide structure at a greatly acidic condition (< pH 2) could be impaired, and the speciation of aluminum could be Al^{3+} at low pH (Figure 5-7) [117, 129, 149]. The edge hydroxyl groups could release from the kaolinite structure as H_2O, and the exposed Al^{3+} could attract the polyphosphate ions by electrostatic. The two possible chelation mechanisms by polyphosphate are summarized in the schematic descriptions in Figure 5-11 and Figure 5-12.

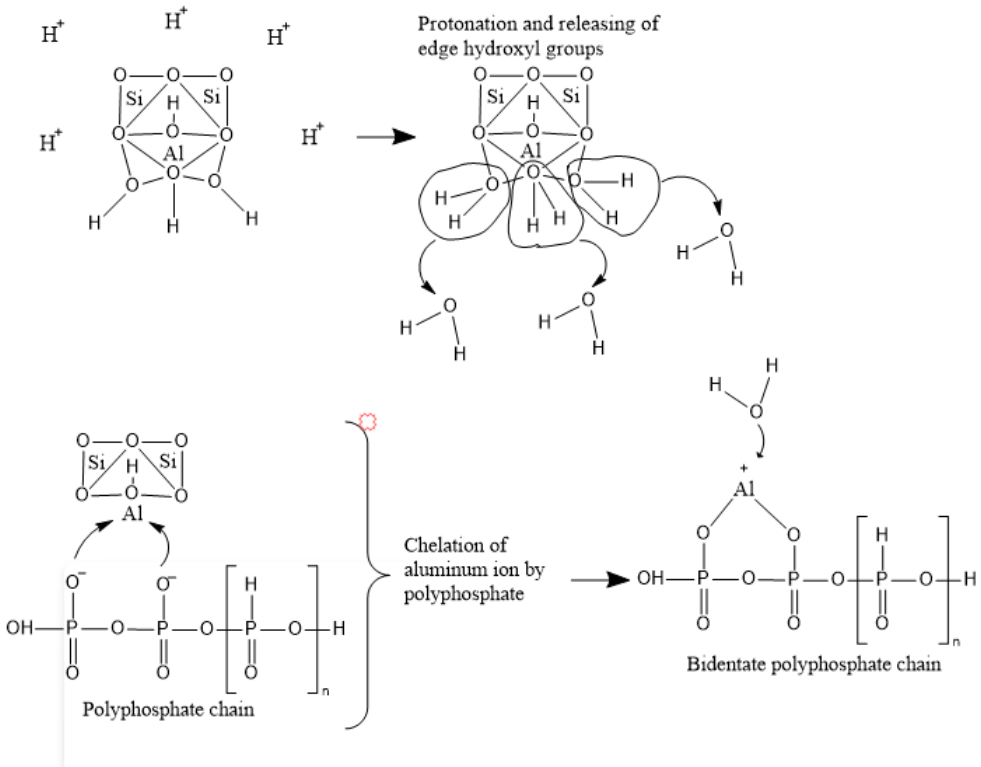

Figure 5-11. Schematic description of kaolinite dissolution driven by the chelation of Al^{3+}

P-subunits possess a strongly acidic hydrogen (pK_a= ~ 0 - 3) and one weakly acidic hydrogen (pK_a= ~ 7 – 9) at either end of the polyphosphate chain [122]. In other words, the p-subunits should be conjugate bases (negatively charged) at low pH due to deprotonation. Additionally, protons might have ceded the available bonding sites to Al^{3+} because protons are merely charge-neutralizers that don't compete for the binding sites [108, 150]. Based on the previous study by de Oliveira Lima et al., the molecular structure of the polyphosphate with aluminum could be a bidentate structure (having two binding sites) due to the high polyphosphate/aluminum ratio [151]. This Al-bidentate complex could have remained soluble in the lixiviant. The structural integrity of kaolinite could have been compromised with the release of Al ion from the aluminol layer. A H_2O molecule could have compensated for the last positive charge of the Al-bidentate complex (Figure 5-11).

Another possible interaction between the polyphosphate chain and aluminum ions could be due to Al complexation due to ligand exchange, and/or or Lewis acid-base interaction. The protonated OH^- edge groups of kaolinite could have been replaced by a nearby polyphosphate chain. The complexation of aluminum ion with the polyphosphate chain may have facilitated the release of Al from the kaolinite structure. Tripolyphosphate and pyrophosphate are known ligands, and polyphosphate may analogously act as ligand to bind with Al [96]. Alternatively, the protonated edge hydroxyl groups could have assumed the role of Lewis acid (electron acceptor) and attracted the deprotonated polyphosphate that behaved as Lewis base (electron donor). As a result of the acid-base interaction, the protonated hydroxyl groups could have been released as H_2O into the lixiviant [149]. The ligand exchange and Lewis acid-base interaction is summarized in Figure 5-12.

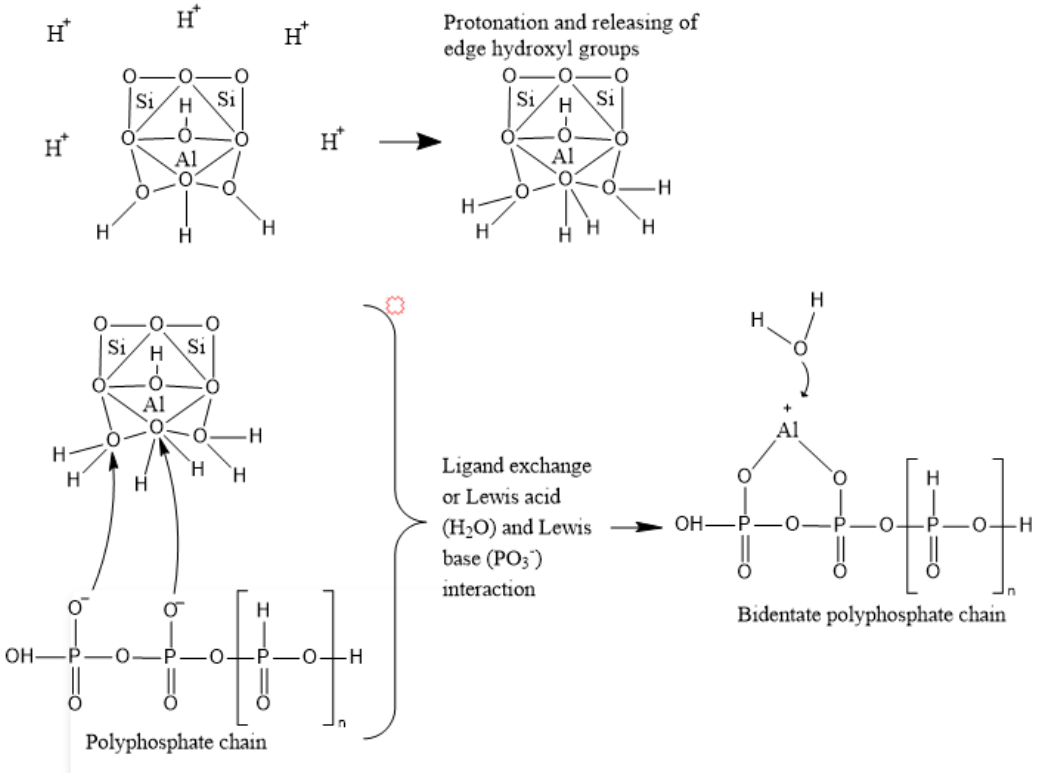

Figure 5-12. Schematic description of ligand exchange & Lewis acid-base interaction. Chelation of aluminum ion by polyphosphate, forming a bidentate complex.

If the aluminum in kaolinite structure is $Al(OH)_3$, the dissolution of aluminum hydroxide in acidic condition can also be describe as Eq. 50 [152].

$$Al(OH)_{3(s)} + 3H^+ = Al^{3+} + 3H_2O \qquad (50)$$

The release of aluminum ion into the lixiviant could have resulted in a formation of anionic sites, electrostatically attracting nearby protons and promoting the dissolution of silicate groups in the upper layer of kaolinite (Figure 5-13) [85, 116].

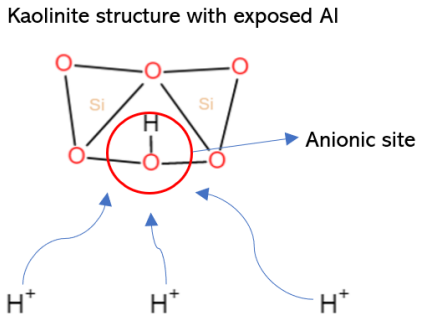

Figure 5-13. Schematic description of silicate groups in the kaolinite structure by protons

The proposed dissolution mechanism aligns with the proposed kaolinite dissolution sequence in the study by Wieland [131].

Polyphosphate, including various length of phosphate, and kaolinite interaction has been a subject of interest by many researchers as polyphosphate adsorption on the positive sites of kaolinite showed the deflocculating behavior [153-157]. In this work, the polyphosphate is presumed to be attracted to the hydroxyl edge groups (positive sites) and basal hydroxyl groups of kaolinite based on previous findings [92, 117, 130-134, 153-157].

The dissolution mechanism of kaolinite was discussed in some studies; however, it's not profoundly elaborated as seen in this study or the lixiviant is different [131, 155, 156, 158]. A study in 1950s by Michaels briefly discussed the ligand exchange mechanism promoted by polyphosphate to justify the dissolution of Al from kaolinite, as the author stated "…replacement of coordinated hydroxyl ion or water molecule by oxygen in the phosphate tetrahedra seems likely." [153].

This work differs from the previous studies in that the working pH is substantially acidic and the synergetic effect of polyphosphate and phosphoric acid is investigated.

5.5 Orthophosphate-assisted kaolinite dissolution

The dissolution of silicate impurity in the graphite concentrate by phosphates should be considered as well. Most phosphates in the lixiviant should originate from 1 M phosphoric acid (H_3PO_4) and the breakdown of polyphosphate chain ($Na[PO_3^-]_n$). A small portion of the phosphates should derive from the hydrolysis of polyphosphate chain. Considering the working pH (~pH 1 expected), the phosphates are likely to be protonated and exist as $H_2PO_4^-$ or H_3PO (Figure 4-7).

As the edge hydroxyl groups became protonated due to the working pH (~ pH 1) being lower than the pH_{pzc} of kaolinite (~ pHpzc 3), partially protonated phosphates that are negatively charged could have been electrostatically attracted to the edge hydroxyl groups [127, 149]. This electrostatic interaction is summarized in Figure 5-14.

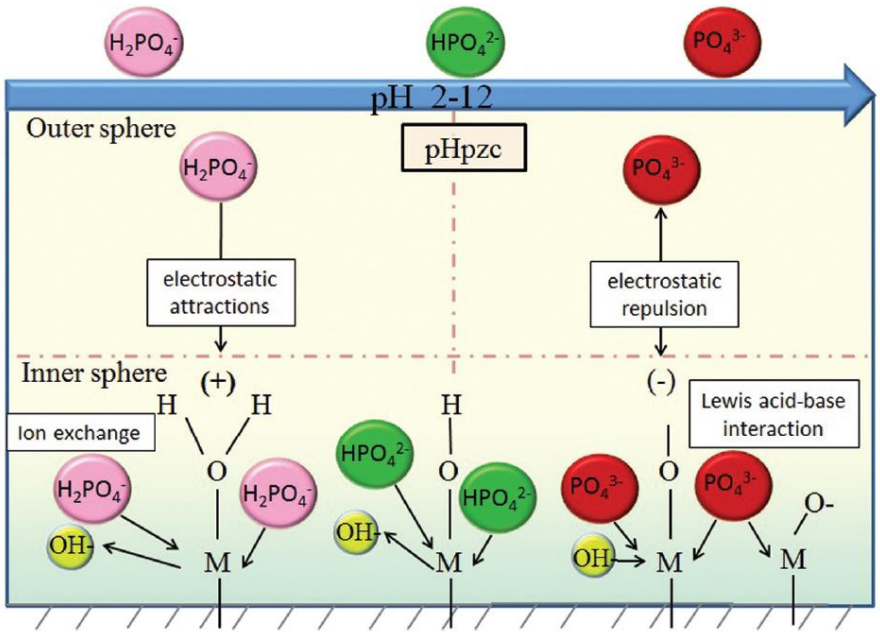

Figure 5-14. Phosphate adsorption mechanism below and above pH_{pzc} [149]

The ligand exchange at a low pH between the protonated hydroxyl groups and phosphate is convincing as metal-based sorbents most widely used are phosphate-based sorbents, and the ligand exchange involving phosphate has already been reported by a few authors [110, 149, 159]. As phosphates are likely to have a single negative charge due to the partial protonation ($H_2PO_4^{2-}$), the formation of monodentate (having one binding site) complexes could be the most convincing complex of the ligand exchange between the kaolinite hydroxyl groups and phosphates.

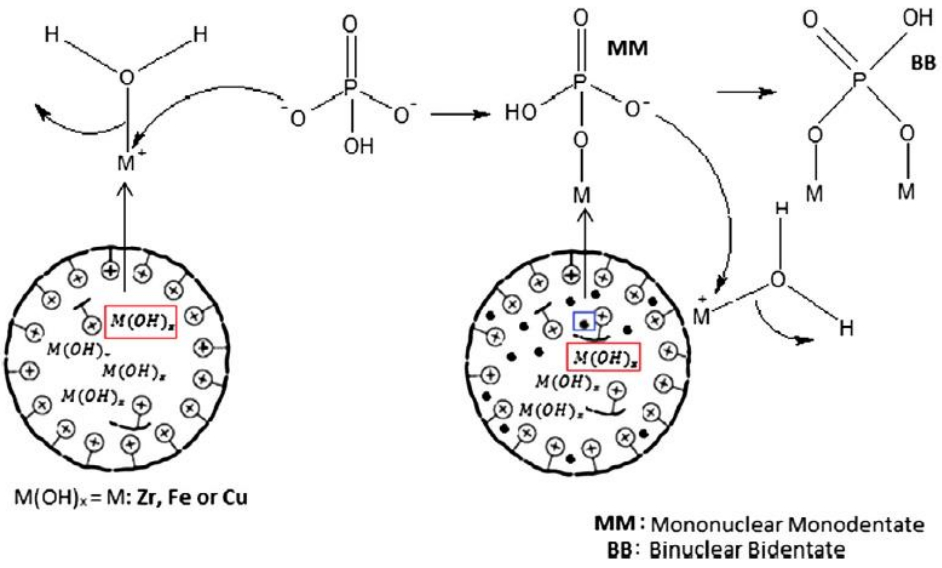

Figure 5-15. Schematic description of the phosphate assisted ligand exchange [159]

Three deprotonated phosphates could be expected to form a complex with an aluminum ion. Protons are reported as being charge-neutralizers that do not necessarily compete for the available binding sites [108]. If this assumption holds, the formation of multidentate complexes with the aluminum ion may be possible as well [159]. As mentioned previously, the acid-base interaction between protonated hydroxyl groups (Lewis acid) on the kaolinite structure and negatively charged phosphates (Lewis base) could have resulted in the formation of soluble aluminum complexes [149].

5.6 Conclusion

This chapter provided an overview of the dissolution mechanisms for the kaolinite impurities in natural concentrated graphite. XRD suggested the presence of three aluminosilicate impurities and kaolinite was selected as the major aluminosilicate given its relatively simple structure compared to other aluminosilicates. A combination of three mechanisms is presumed to be responsible for the impurity dissolution: proton-assisted, polyphosphate-assisted, and orthophosphate-assisted mechanisms. Each mechanism was examined in depth to explain the dissolution of the target impurities (Fe, Al, and Si). In the next chapter, design of experiment (DOE) will be performed to optimize the operating variables to maximize the dissolution of graphite impurities with polyphosphate and phosphoric acid.

6 Design of Experiments (DoE) using Central Composite Design to Generate an Impurity Leaching Model

Using the graphite impurity leaching operating conditions in Chapter 40, DOE was performed to study the interactions between the leaching operating parameters and impurity dissolution.

Table 6-1. Author Statement

Conceptualization, Writing (Review & Editing)	Hak Jun Oh Associate Professor Sidney Omelon
Investigation, Writing (Original Draft)	Hak Jun Oh
Methodology	Hak Jun Oh Ozan Kökkılıç (Research Associate) Associate Professor Sidney Omelon

6.1 Goal

The goal of this chapter is to generate, describe and interpret the DOE leaching results in order to identify the optimal impurity leaching conditions.

6.2 Theory

The central composite design procedure of response surface methodology (RSM) consists of five parts [88, 97]:

1) Perform a series of experiments.
2) Develop a mathematical model to obtain the desired response.
3) Analyzing the model and verifying the model adequacy.
4) Drawing the two-dimensional and three-dimensional plots.
5) Optimization & validation (with contour and surface plots, overlaying the plots, and response optimizer).

The central composite design of RSM was selected because it is a thorough approach that studies each factor without aliasing effect (effect of one factor being overshadowed by grouping with another) [88, 97]. With the DOE software (Minitab20) a mathematical model can be developed to predict the desired response. A graphical analysis needs to be performed to check the model adequacy. Along with the Fischer test (F-test), three graphs need to be verified: normal probability plot, versus fits, and versus order.

6.3 Methods

The low and high boundaries of the leaching operating variables were identified in Chapter 4, and are summarized in Table 4-3. These values were used to create 32 leaching conditions with the DoE Response Surface Method - Central Composite Design (Table 6-2) (Minitab20) with a two-level factorial design (Eq. 51).

$$\#\ of\ experimental\ runs = 2^{K\ (\#\ of\ variables\ to\ optimize)} \qquad (51)$$

The runs were completed sequentially. Each run leached 1 ± 0.01 g of concentrated graphite in a 15 mL Teflon tube (VWR). The lixiviant volume depended on the liquid to solid ratio. The graphite-lixiviant solution was vortexed and placed in a heat block (Dry bath/heat block, Thermo Scientific). The leaching time and temperature were set by the run condition. The slurry was syringe-filtered to recover the PLS.

For each run, a spiked sample was prepared by adding 20 ppm of standards containing the target impurities (Al, Fe, Si, and K). The unspiked and spiked samples were diluted 2x with RO water, and digested with a 1:1 volume ratio of sample: 2 M HCl for an hour at 100 °C in the dry heat block. After digestion, the unspiked and spiked samples were diluted at 1:4 ratio with RO water for a final dilution factor of 20. The diluted PLS samples were analyzed for Fe, Si, Al, and K concentration with MP-AES.

The PLS element concentrations were factors for processing with the response surface methodology (RSM). RSM is a statistical and mathematical design method to evaluate the effect of factors and their interactions, with the goal of identifying the optimum conditions for a defined desirable response [88, 97]. The response for this study is the percent of the impurity element that was measured in the PLS.

Table 6-2. Design of Experiment runs designed using Minitab

Run Order	H_3PO_4 (mol/L)	L/S	Temp. (degC)	LT (min)	PolyP (mol/L)
1	3	5	60	180	1.30
2	2	6	81	240	0.60
3	2	6	41	240	1.9
4	4	6	41	120	1.9
5	4	4	40	120	0.6
6	3	5	61	180	1.3
7	2	6	41	120	0.6

Run Order	H_3PO_4 (mol/L)	L/S	Temp. (degC)	LT (min)	PolyP (mol/L)
8	3	5	60	180	0.0
9	3	5	60	183	1.3
10	2	4	41	120	1.9
11	3	3	61	180	1.3
12	3	7	61	183	1.3
13	3	5	61	186	1.3
14	3	5	61	190	2.5
15	2	4	41	245	0.6
16	3	5	60	180	1.3
17	4	4	80	240	0.6
18	4	6	80	242	1.9
19	2	4	80	245	1.9
20	3	5	61	60	1.3
21	5	5	61	185	1.3
22	2	6	81	120	1.9
23	1	5	60	182	1.3
24	4	6	80	120	0.6
25	3	5	19	183	1.3
26	4	6	41	240	0.6
27	3	5	60	300	1.3
28	3	5	60	180	1.3
29	2	4	80	121	0.6
30	4	4	80	124	1.9
31	4	4	40	240	1.9
32	3	5	100	180	1.3

6.1 Results & Discussion

The results from the central composite design work, and the spiking results are presented. The model results, include the factor weighting and interaction results, as well as model contour plots are shown and discussed.

6.1.1 Predicted extraction % and experimental extraction %

This subsection presents an analysis of the normal distribution of residuals, the consistence variance, and the random nature of the residuals generated by subtracting the predicted model and the experimental results. To confirm the model results the residuals – the difference between the mean model value and experimental result for each case - were plotted for each element (Figure 6-1). The normal probability plot (left column) shows acceptable residual distribution. The

variance plot (middle column) shows acceptable variance distributions. Over the 32 runs, the variance between run shows that the residuals are independent of one another.

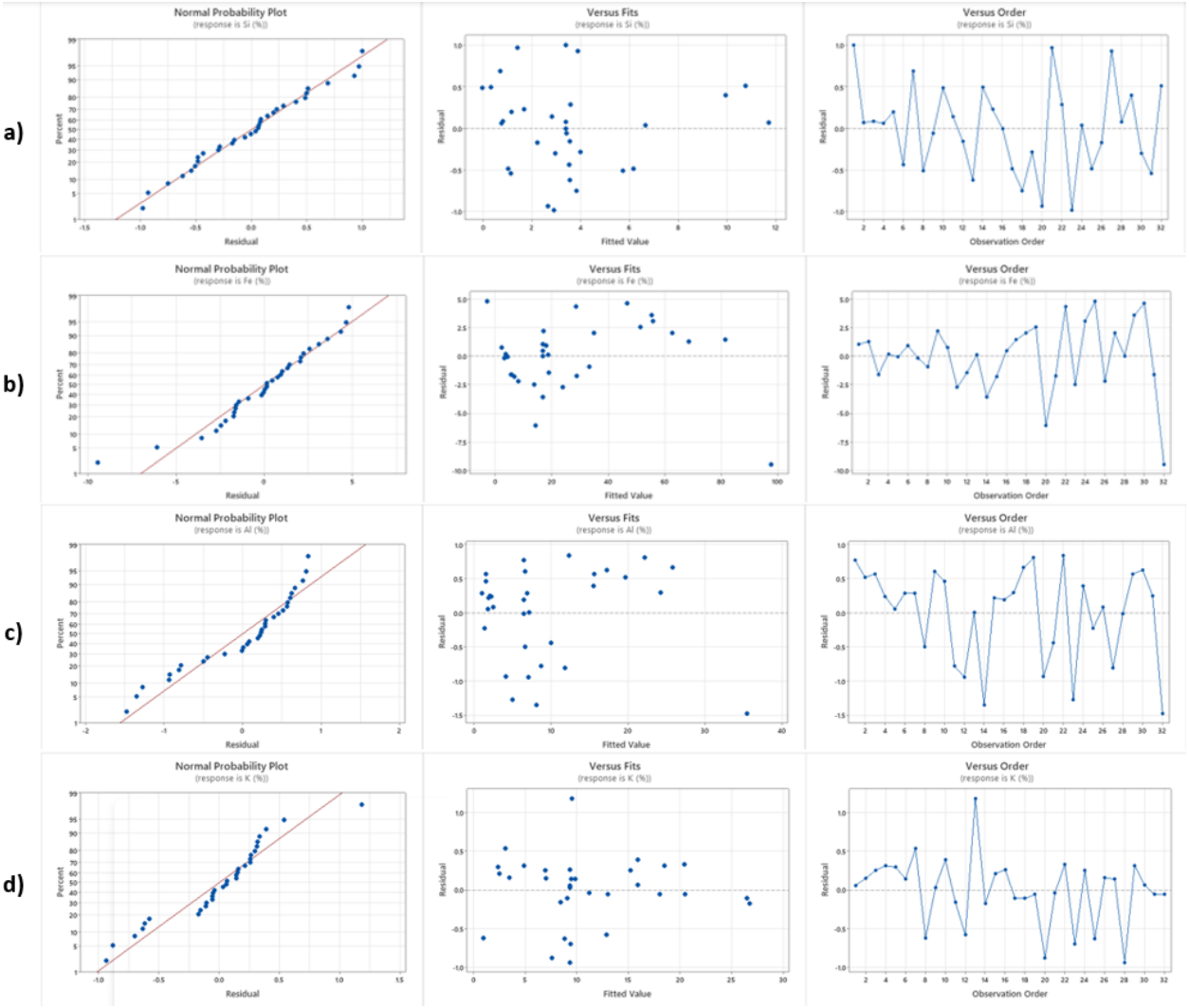

Figure 6-1. Graphical analysis comprising the normal probability plot of residuals (left column), residuals versus fitted value (middle column), and residuals versus observation order (right column). a) Si, b) Fe, c) Al, and d) K

6.1.2 Central Composite Design Results

The DoE PLS concentration impurity extraction results for each run number are shown in Figure 6-2. The percent extraction values were calculated with Eq. 42. Average values are not relevant for Figure 6-2 due to randomized variable selection.

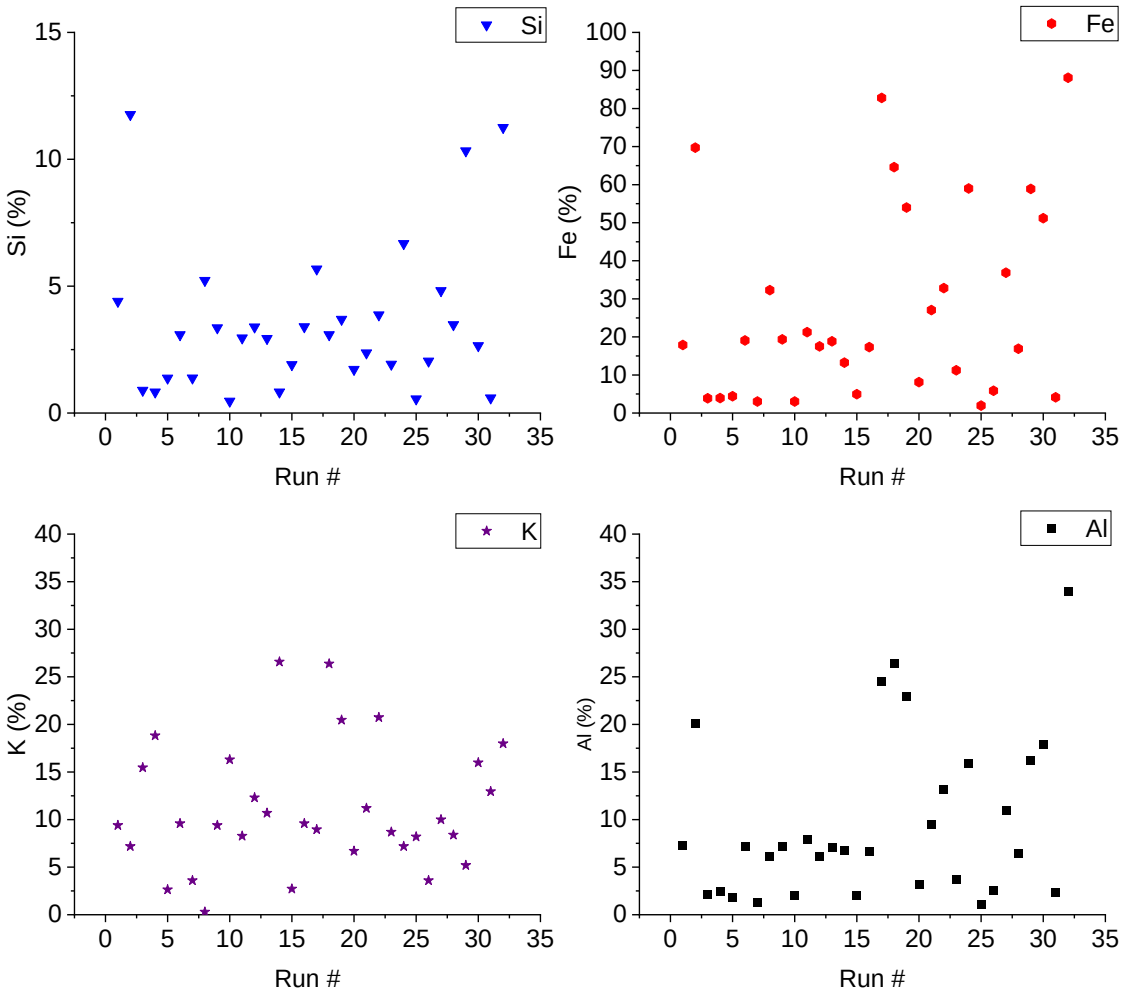

Figure 6-2. Percent dissolved values for Si, Fe, K, and Al elements from 32 DoE central composite design runs

These randomized results showed that the maximum % dissolved impurity values were Fe: 88%, Si: 12%, K: 27%, and Al: 34%.

6.1.3 Element Spiking Results

The tolerance limit provided for the spiking recovery was assumed to be acceptable from 75 - 125% for this study. The spiking results for each element and each run are shown in Figure 6-3: Formation of low volatile phosphate species and concealment of the measured element due to its association with phosphate would generate free element concentrations, which may be less than

the total element concentrations [89]. Residual polyphosphate in the PLS may also reduce the measured element concentration due to ion pair formation.

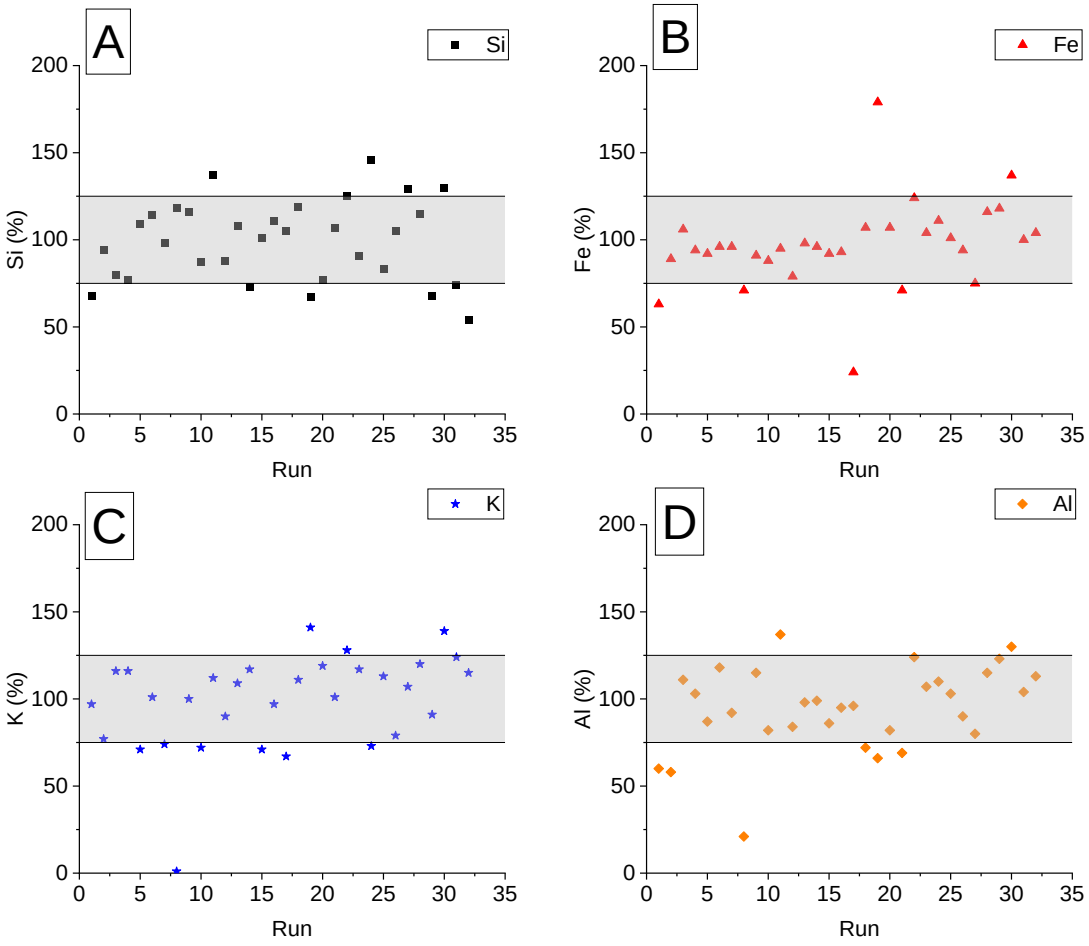

Figure 6-3. Spiking results for A) Si, B) Fe, C) K, and D) Al

6.1.4 Interpretation of DoE results: Identification of important factors and interactions

Only a few of the leaching process factors were identified as statistically significant factors that independently affected the percent leached of the different impurity elements. The model coefficient, T and P-values are presented in Table 6-3 -

Table 6-6. Temperature, phosphoric acid concentration, polyphosphate concentration, and leaching time (in red font) were identified as major factors for the model that predicts the percent of each element leached. Noteworthy interactions are also included.

Table 6-3. Statistically significant factors and interactions identified for Si

Si				
Factors	Coef	SE Coef	T-Value	P-Value
Temp (°C)	2.514	0.181	13.88	0
Temp (°C)*Temp (°C)	0.619	0.16	3.86	0.003
H_3PO_4 (mol/L)*PolyP (mol/L)	0.48	0.213	2.26	0.045
L/S*LT (min)	0.494	0.22	2.24	0.046
H_3PO_4 (mol/L)	-0.424	0.181	-2.34	0.039
H_3PO_4 (mol/L)*Temp (°C)	-0.72	0.223	-3.22	0.008
Temp (°C)*PolyP (mol/L)	-1.031	0.215	-4.8	0.001
PolyP (mol/L)	-1.369	0.176	-7.77	0

Table 6-4. Statistically significant factors and interactions identified for Fe

Fe				
Factors	Coef	SE Coef	T-Value	P-Value
Temp (°C)	25.47	1.04	24.51	0
Temp (°C)*Temp (°C)	7.611	0.92	8.27	0
LT (min)	5.36	1.03	5.19	0
Temp (°C)*LT (min)	4.09	1.27	3.21	0.008
H_3PO_4 (mol/L)	3.22	1.04	3.1	0.01
Temp (°C)*PolyP (mol/L)	-4.18	1.23	-3.4	0.006
PolyP (mol/L)	-4.58	1.01	-4.53	0.001

Table 6-5. Statistically significant factors and interactions identified for Al

Al				
Factors	Coef	SE Coef	T-Value	P-Value
Temp (°C)	8.54	0.231	36.97	0
Temp (°C)*Temp (°C)	2.969	0.205	14.52	0
LT (min)	1.958	0.229	8.54	0

Temp (°C)*LT (min)	1.857	0.283	6.57	0
H_3PO_4 (mol/L)	1.069	0.231	4.63	0.001
H_3PO_4 (mol/L)*Temp (°C)	0.734	0.285	2.58	0.026

Table 6-6. Statistically significant factors and interactions identified for K

K				
Factors	Coef	SE Coef	T-Value	P-Value
PolyP (mol/L)	6.397	0.146	43.74	0
Temp (°C)	2.28	0.15	15.17	0
PolyP (mol/L)*PolyP (mol/L)	1.226	0.134	9.13	0
Temp (°C)*Temp (°C)	1.026	0.133	7.71	0
Temp (°C)*LT (min)	1.298	0.184	7.05	0
L/S	1.033	0.15	6.88	0
L/S*PolyP (mol/L)	0.834	0.177	4.73	0.001
H_3PO_4 (mol/L)*L/S	0.852	0.184	4.64	0.001
LT (min)	0.566	0.149	3.79	0.003
H_3PO_4 (mol/L)	0.397	0.15	2.64	0.023
H_3PO_4 (mol/L)*LT (min)	0.472	0.182	2.59	0.025
L/S*L/S	0.302	0.136	2.22	0.048

Factors with a P-value lower than 0.05 are significant. The T-value indicates the magnitude and of the relationship (positive or negative) between the main factor and the response. The factor coefficient represents the magnitude of the factor "importance". It signifies the degree of influence on the response [88, 97].

Leaching time has a positive impact on Fe, Al, and K. This could be due to the slow kinetics of dissolution. Temperature and phosphoric acid concentration are significant factors for all impurity element responses. In all cases, temperature positively influenced the response. This could be explained by the high temperature enhancing the leaching kinetics [85] and chemical activity. H_3PO_4 concentration positively influenced the response of all cations, but it had a negative influence on Si. Si as SiO_4^{4-} (the silicate impurities), may require protonation to dissolve; at high phosphoric acid concentration, the protonation of phosphate ions at low pH may reduce Si dissolution as soluble silicic acid ($Si(OH)_4$ or H_4SiO_4) [92, 131, 160, 161].

The concentration of polyphosphate had different effects on impurity dissolution. K dissolution was enhanced with increasing polyphosphate concentration. K is a soluble ion, but its relationship with dissolved polyphosphate is not known. Trivalent Al and Fe concentrations were unchanged (Al) or reduced (Fe) with increasing polyphosphate concentration. It is possible that this response was due to excessive chelation by polyphosphate, which would decrease the free ion concentration

that can be detected with MP-AES and enhance dissolution. Previous studies showed that increasing concentration of the ligands oxalate ($C_2O_4^{2-}$) and salicylate ($C_7H_5O_3^-$) promoted Al and Si dissolution [92, 131, 132]. However, their ligand concentrations were significantly lower (mM range) and pHs were higher ([2 – 6] pH range). Also, spontaneous hydrolytic polyphosphate degradation could create orthophosphate that would also form ion pairs with Al and Fe, concealing these cations from MP-AES detection.

Si dissolution response to increasing polyphosphate was negative. Some possible mechanisms for this reduced response include the increasing sodium concentration with increasing polyphosphate concentration, as polyphosphate is added as the soluble sodium salt. Sodium may compete with protons and therefore the formation of soluble silicic acid from silicate solids. In addition, high polyphosphate concentrations could have reduced the free proton concentration in the acidic leaching conditions [108].

6.1.5 Contour plot results

Contour plots (Figure 6-4) were generated to verify if polyphosphate paired with phosphoric acid had a synergetic effect on the impurity extraction. The contour plot for Al extraction (Figure 6-4 A) shows a maximum response at the highest polyphosphate and phosphoric concentrations. This conclusion aligns with the previous findings on the ligands promoting Al dissolution [92, 131, 132]. The contour plots in Figure 6-4 B and C confirm that increasing polyphosphate concentration decreased the response of Si and Fe extractions.

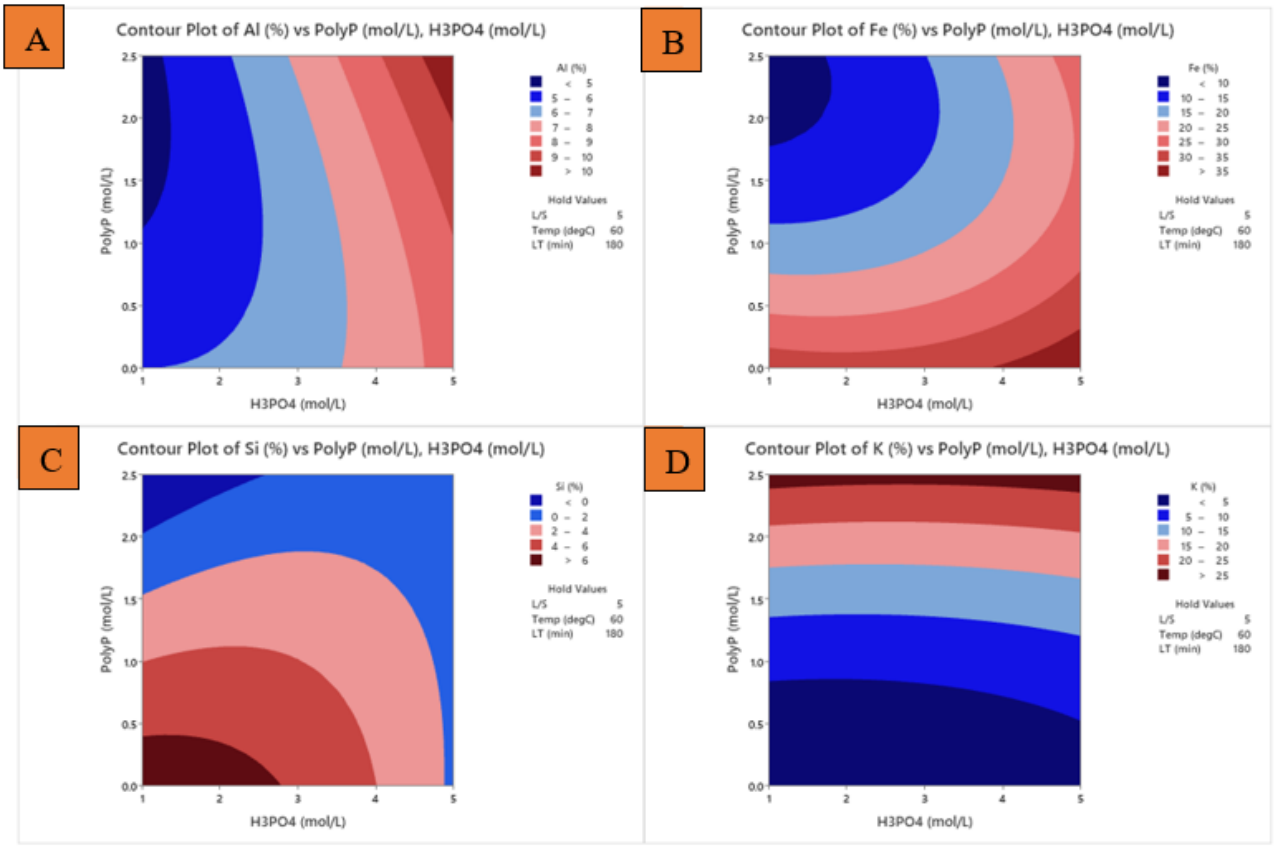

Figure 6-4. Contour plots of % extraction of A) Al, B) Fe, C) Si, and D) K as a function of H_3PO_4 and polyP concentrations.

6.2 Conclusions

32 leaching conditions generated by the DoE central composite design were conducted and examined to build an impurity element leaching model for each impurity (Fe, Si, Al, and K). Increasing temperature promoted impurity dissolution for all elements. Increasing H_3PO_4 concentration enhances dissolved cation concentrations, while reduced the Si dissolution. Increasing polyP concentration did not increase on the leached, measured Al or Fe concentrations. It is not known if the dissolution was reduced, and/or if the concentrations were under-measured because of polyphosphate concealment of these cations. In Chapter 7, the leaching operating variables will be optimized using the response optimizer mathematical models. The model predictions were challenged with another set of leaching experiments.

7 Optimization of the Operating Parameters using Mathematical Models and Prediction Validation Resulting in a Two-Step Leaching Proposal

In Chapter 6, 32 DOE results for graphite leaching conditions between the boundaries identified in Chapter 0 were presented and analyzed. The effect of each operating variable on each impurity element (Si, Fe, Al, and K) dissolution response were briefly discussed. Mathematical models were built with the results of the 32 DoE center composite design experiments to optimize the impurity extractions responses. It was noted that the effect of polyphosphate on element leaching differed for different elements. This chapter presents the model predictions to optimize the leaching conditions for each impurity, and for impurity pairs (Fe-Si, Fe-Al, Si-Al) and Si-Fe-Al. K was not included because of its straightforward increase in solubility with increasing lixiviant phosphoric acid or polyphosphate concentration. The optimized leaching conditions were undertaken, to validate the predicted model results.

Different leaching conditions favored different elements. Therefore, a two-stage leaching process was proposed to allow for two different leaching conditions to optimize Al or Si dissolution. The effect of the sequential order of the two steps was tested.

Table 7-1. Author Statement

Conceptualization, Writing (Review & Editing)	Hak Jun Oh Associate Professor Sidney Omelon
Investigation, Writing (Original Draft)	Hak Jun Oh
Methodology	Hak Jun Oh Ozan Kökkılıç (Research Associate) Associate Professor Sidney Omelon

7.1 Goal

The goal is to validate the optimized impurity leaching conditions with the mathematical models generated by the response optimizer function of Minitab (Minitab20, Minitab, LLC). The pregnant leaching solutions were analyzed using MP-AES to study the degree of precision between the predicted and experimental element dissolution responses.

7.2 Methods

The complex responses of different elements to the different leaching conditions were not well represented by 2D plots. Therefore, the response optimizer function (Minitab20) was used to

optimize the leaching process conditions and predict the % extraction responses for each target impurity Fe, Al and Si, pairs (Fe-Al, Fe-Si, Al-Si), and Fe-Al-Si. K was not studied due to its increasing % extraction with increasing phosphoric acid or polyP concentration. A summary of the predicted extractions using the greatest Al extraction, 33.95% in Chapter 6, is provided.

Table 7-2. Example response optimizer prediction of leaching conditions for a target of 33.95% Al extracted.

Case	[H_3PO_4] (mol/L)	L/S	Temp (°C)	LT (min)	PolyP (mol/L)	Al% extracted	Desirability
1	5	7	100	300	3	60.2	1.00
2	1	7	100	300	3	42.3	1.00
3	5	3	100	300	3	57.6	1.00
4	1	3	100	300	3	47.6	1.00
5	5	7	100	300	0	52.6	1.00
6	1	7	100	300	0	38.4	1.00
7	5	3	100	300	0	53.9	1.00
8	1	3	100	300	0	47.5	1.00
9	5	4	80	300	3	33.9	1.00
10	3	5	85	300	3	33.9	1.00
11	4	4	85	300	0	33.9	1.00
12	5	3	100	60	0	33.6	0.99
13	3	7	92	224	3	33.1	0.97
14	5	3	100	61	3	32.4	0.95
15	5	7	100	63	3	31.4	0.92
16	1	3	100	62	0	31.3	0.92
17	5	7	100	65	0	29.0	0.85
18	1	3	98	73	2	26.7	0.78
19	1	7	100	73	0	19.7	0.57
20	1	7	100	78	3	19.4	0.56
21	1	3	19	60	0	15.5	0.44
22	1	3	19	108	0	11.9	0.33
23	1	7	19	60	0	9.5	0.26
24	1	3	19	60	2	9.3	0.25

The optimized responses for each element and element combination from the model were validated by comparing them with new experimental results generated by the optimized leaching process conditions. Each element or element combination optimization has four leaching process conditions (target case). The definition characteristics of the four runs are:

1) The first run is the first optimized case with the highest extraction of target impurity.
2) The second run is the average of all runs with desirability greater than 0.98. Desirability is defined by the closeness of a response to its ideal value, a target value initially set to maximize in this case.
3) The third run is randomly chosen among the optimized cases with +0.98 desirability. If the phosphoric acid concentration was 1 M in the first case, the optimized conditions are identical to run 1 with the phosphoric acid lowered to 0.5 M.
4) The fourth run is the average of three optimized cases with the yield close to the target. Target is the maximum extracted value of the impurity in the result of DOE in part 1.

Table 7-3. Minitab response optimizer element or element combination leaching conditions

Target case	Run #	H_3PO_4 (mol/L)	L/S	Temp (°C)	LT (min)	polyP (mol/L)
Al	1	5.0	7	100	300	2.5
	2	3.4	5	100	280	1.3
	3	5.0	3	100	300	2.5
	4	4.0	4	100	300	1.7
Si	1	1.0	7	100	300	0.0
	2	2.2	5	100	183	0.3
	3	0.5	7	100	300	0.0
	4	5.0	7	100	247	0.2
Fe-Al	1	1.0	3	100	280	2.3
	2	3.0	5	100	235	2.1
	3	0.5	3	100	280	2.3
	4	3.5	6	100	180	1.4
Fe-Si	1	1.0	7	90	215	0.0
	2	2.5	5	90	180	0.1
	3	0.5	7	90	220	0.0
	4	3.7	6	90	200	0.0
Al-Si	1	1.0	7	100	300	0.0
	2	2.1	4	100	250	0.0
	3	0.5	7	100	300	0.0
	4	4.4	3	100	140	0.0
Fe-Al-Si	1	1.0	7	100	286	1.8
	2	1.0	6	100	249	1.6
	3	0.5	7	100	286	1.8
	4	1.0	4	100	174	1.2

After leaching, solid-liquid separation via vacuum filtration in a Buchner funnel and sample washing with RO water were performed after leaching. High PLS element concentrations required that the PLS was diluted 100x instead of 20x (Section 4.7.1.4) before analyzed for element concentration with MP-AES, and the % extraction calculated.

The relative deviations between the model and experimental results were calculated (Eq. 52).

$$Relative\ Deviation\ (\%) = \frac{Predicted\ extraction\ (\%) - Measured\ extraction\ (\%)}{Predicted\ extraction\ (\%)} \times 100 \quad (52)$$

A leaching sample preparation and experimental method procedure is described in Section 6.3.

The results from the element and element combinations suggested that two separated, sequential leaching processes could optimize the extraction of Al and Si. Three replicates of optimal Al leaching, solids separation and sample washing with RO water, then optimal Si leaching, and three replicates of optimal Si, solids separation, the optimal Al leaching were undertaken with the leaching conditions presented in Table 7-4 and Table 7-5

Table 7-4. Leaching conditions for Al-Si two-stage leaching

Stage #	Target impurity	H_3PO_4 (mol/L)	L/S	Temp (°C)	LT (min)	PolyP (mol/L)
1	Al	5.0	7	100	300	2.5
2	Si	1.0	7	100	300	0.0

Table 7-5. Leaching conditions for Si-Al two-stage leaching

Stage #	Target impurity	H_3PO_4 (mol/L)	L/S	Temp (°C)	LT (min)	PolyP (mol/L)
1	Si	1.0	7	100	300	0.0
2	Al	5.0	7	100	300	2.5

The graphite loss after each leaching step was accounted for in the compositional mass balance of the remaining impurities. The 1st stage extraction percentages for each impurity element (Fe, Si, and Al) were calculated by subtracting the leached impurity contents from the initial impurity contents. Same calculation was repeated for the 2nd stage cumulative extraction percentages with the adjusted impurity contents in the graphite concentrate that underwent 1st stage leaching.

7.3 Results and Discussion

This section presents the comparison between the predicted and experimental extraction values. Leaching graphite impurities with two lixiviants and in two steps is presented and discussed.

7.3.1 Model prediction validation

Table 7-6 compares the predicted and experimental model responses.

Table 7-6. Predicted responses and experimental results, and their deviations

Target impurity	Run #	Predicted extraction (%)			Measured extraction (%)			**Deviation (%)**		
		Si	Al	Fe	Si	Al	Fe	**Si**	**Al**	**Fe**
Al	1	2.6	60.2	100.0	3.8	54.8	97.8	**-43.7**	**8.9**	**2.2**
	2	9.9	47.3	100.0	8.7	30.2	85.3	**12.5**	**36.2**	**14.7**
	3	0.0	57.6	100.0	1.1	57.9	98.8	**N/A**	**-0.6**	**1.2**
	4	5.6	52.5	100.0	4.9	47.0	102.9	**12.2**	**10.4**	**-2.9**
Si	1	25.0	38.4	100.0	19.0	10.5	41.1	**24.3**	**72.5**	**58.9**
	2	17.7	33.4	100.0	15.3	16.3	57.4	**13.4**	**51.2**	**42.6**
	3	25.8	37.0	100.0	13.6	8.9	28.9	**47.1**	**75.8**	**71.1**
	4	12.2	46.4	100.0	6.7	36.7	68.6	**44.9**	**21.0**	**31.4**
Fe-Al	1	4.2	45.5	99.9	9.4	17.1	59.3	**-121.8**	**62.4**	**40.6**
	2	6.3	40.6	94.4	10.9	28.3	83.5	**-73.5**	**30.4**	**11.5**
	3	4.2	44.6	96.7	10.0	13.9	49.5	**-135.6**	**68.9**	**48.8**
	4	9.2	36.4	97.7	14.9	27.3	82.7	**-62.8**	**25.0**	**15.3**
Fe-Si	1	18.9	21.4	95.1	12.3	9.5	42.6	**34.6**	**55.4**	**55.1**
	2	15.3	24.3	95.1	12.7	18.7	71.4	**17.2**	**22.8**	**24.9**
	3	19.3	20.3	93.9	8.9	4.7	20.2	**53.9**	**76.7**	**78.5**
	4	12.5	28.1	100.0	8.7	18.9	65.0	**30.5**	**32.9**	**35.0**
Al-Si	1	25.0	38.4	100.0	19.0	10.3	42.1	**23.9**	**73.1**	**57.9**
	2	19.3	40.5	100.0	14.1	16.4	58.6	**26.9**	**59.4**	**41.4**
	3	25.8	37.0	100.0	15.4	7.0	30.2	**40.5**	**81.0**	**69.8**
	4	11.8	37.6	100.0	4.3	26.8	72.0	**63.4**	**28.9**	**28.0**
Fe-Al-Si	1	11.8	39.2	99.9	20.5	15.3	59.9	**-74.0**	**61.1**	**40.1**
	2	12.0	36.0	92.1	18.4	13.3	53.0	**-52.8**	**63.2**	**42.4**
	3	11.8	37.5	96.6	14.2	9.3	38.4	**-20.6**	**75.1**	**60.2**
	4	13.5	34.0	93.1	16.8	17.5	79.4	**-24.7**	**48.5**	**14.7**

The smallest deviations were observed for the 1st runs that optimized Al or Si (highlighted in yellow). The leaching conditions that optimized Al (highest phosphoric acid and polyphosphate

concentrations) and Si (lowest phosphoric acid and no polyphosphate) were very different. It was decided to compare two sequential two-step leaching processes to maximize these different impurity extractions. Solid-liquid separation and washing was completed between each leaching step. The importance of the leaching sequence was not known. Therefore, both sequences were tested.

7.3.2 Spiking results

Spiking was completed (Figure 7-1). More spiking results were outside of the 25% acceptable tolerance. In general, the spiking concentrations were undermeasured. This undermeasurement could be explained by the formation of low volatile compounds that conceal the elements of interest [89]. The measurement technique should be improved for future work.

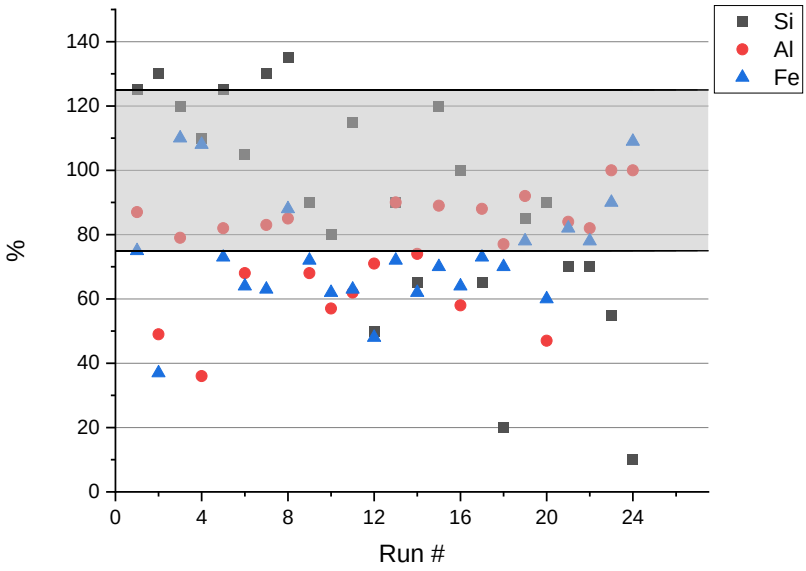

Figure 7-1. Overview of the spiking recovery rate (25% tolerance range)

7.3.3 Comparative study of two-stage Al-Si leaching processes

Two-stage leaching was hypothesized to maximize Al dissolution and Si dissolution independently, as they were determined to be optimized with different lixiviant compositions. The cumulative extraction percent values for Stage 1 optimized for Al extraction and Stage 2 optimized for Si extraction are shown in Figure 7-2.

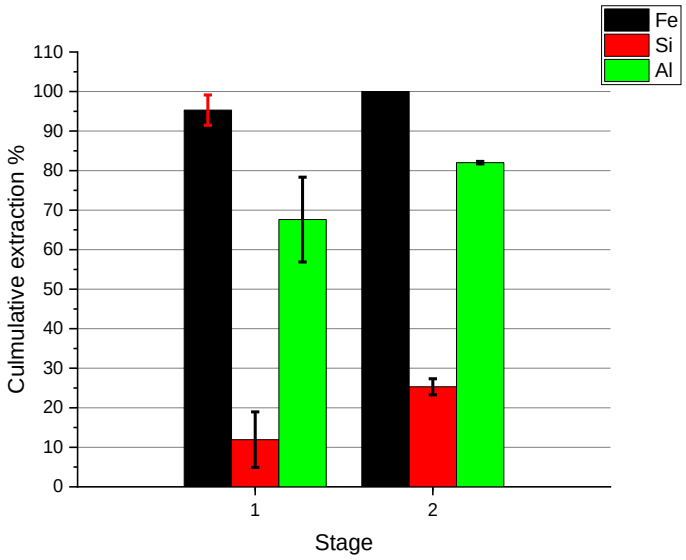

Figure 7-2. Cumulative extraction % of Fe, Al, and Si after two-stage leaching. The first stage optimizes Al leaching. The second stage optimizes Si leaching. n=3

Fe dissolution was complete (95% after the first stage, and 100% after the second stage). Al extraction was not increased significantly from 68% to 82% by the second stage (Student's t-test, $p = 0.1$). Si extraction was significantly increased from 12% to 25% in the second stage (Student's t-test, $p = 0.0004$)

The results of leaching in two stages to optimize for Si extraction first, followed by Al leaching optimization, are shown in Figure 7-3

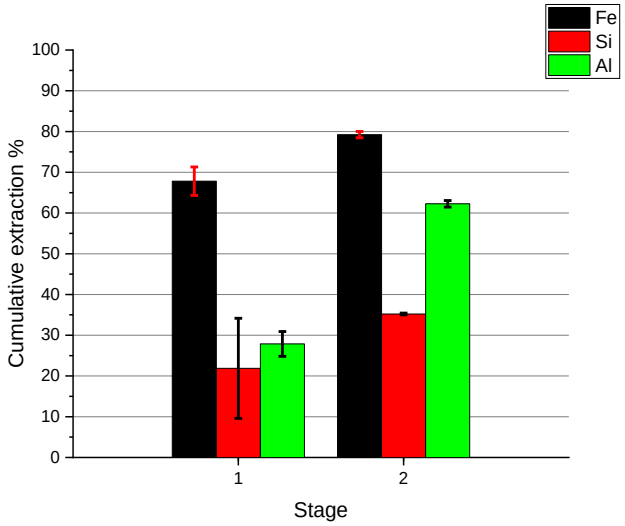

Figure 7-3. Cumulative extraction % of Fe, Al, and Si after two-stage leaching. The first stage optimizes Si leaching. The second stage optimizes Al leaching. n=3

The Fe extraction percent increased from 68% to 80% with the two-staged leaching process. The Si extraction increased from 22% (with large errors) to 35% after the second ($p = 0.02$). Al is increased from 28% to 62%, with $p = 7x10^{-5}$

Al-Si two-stage leaching was more successful than Si-Al two-stage leaching because of the larger cumulative extraction % of Fe and Al after two stages. The Si extraction % nearly doubled for the Al-Si two-stage leaching. This increase may be due to Al-layer removal that accelerates the Si-layer dissolution in the kaolinite as discussed in Chapter 50. An overall larger extraction % of Si was observed for Si-Al two-step leaching.

7.4 Conclusion

Optimized impurity leaching conditions for single element and element combinations were found using the response optimizer function of Minitab. These leaching condition model results were validated by assessing the extraction percentage predictions of the six optimized cases (Al, Si, Al-Si, Al-Fe, Si-Fe, Si-Al-Fe) with the extraction percentage response. The smallest deviations between the modeled and measured percent extraction results were for single Si (8.9%) and Al (24.3%) extractions. The optimized lixiviant phosphoric acid and polyphosphate concentrations were of the lowest values for optimal Si and highest for optimal Al leaching processes. In light of this, two two-stage leaching processes, separated by a solids separation and washing step, were studied. Optimization of Al extraction in the first stage, followed by optimization of Si extraction in the second stage, extracted 100 % of the Fe, the highest cumulative Al (~82%) and Si (~25%) extraction percent values. In the next chapter, the Al-optimized, followed by the Si-optimized, two-step leaching process was repeated with mechanical stirring, with the goal of enhancing the leaching kinetics. Both the PLS and leached graphite solid were characterized.

8 Two-stage leaching, optimizing for Al then Si, with agitation.

In Chapter 7, two leaching stages with different phosphoric and polyphosphate concentrations were proposed and tested to optimize Al (or Si) leaching, followed by leaching conditions to optimize Si (or Al) leaching. The PLS and the product solids were analyzed to confirm the leaching extent. In Chapter 7, the effect if agitation was measured for the Al - optimized, followed by the Si - optimized leaching process.

Table 8-1. Author Statement

Conceptualization, Writing (Reviewing & Editing)	Hak Jun Oh Associate Professor Sidney Omelon
Investigation	Hak Jun Oh Tian Zhao (Ph.D. Candidate)
Methodology	Hak Jun Oh Ozan Kökkılıç (Research Associate) Associate Professor Sidney Omelon
Writing – Original Draft	Hak Jun Oh

8.1 Goal

The goal is to study the effect of agitation on the two-stage (Al - Si) optimized leaching process.

8.2 Theory – Agitation Effect

Agitation is a mixing operation to homogenize a heterogeneous system, or to enhance mass and/or energy transfer. In the case of leaching, a suspension of the solids in liquid is desired to maximize the contact between the bulk solution composition and the solid surface area for the chemical reactions occurs [162, 163]. Forced liquid convection increases chemical reaction kinetics if the surface layer diffusion is the rate limiting step [162, 163]. Agitation is expected to improve the impurity extraction percentages.

8.3 Methods

One sample of natural graphite concentrate (1 ± 0.01) g was added to 15 mL Teflon tubes with caps (VWR). For the first leaching stage, 2.5 mol/L of sodium polyphosphate was dissolved in 5 mol/L phosphoric acid (H_3PO_4). After the complete dissolution of sodium polyphosphate, the lixiviant was added with a magnetic stir bar to the Teflon tube. The slurry was vortexed to generate a homogenous suspension. The Teflon tube was suspended in a 100 mL beaker filled with water with a heat-resistant foam ring. The beaker was placed on a heating plate to achieve a 100 °C

leaching temperature. The leaching conditions are described in Section 7.3.3. The experimental setup is shown in Figure 8-1.

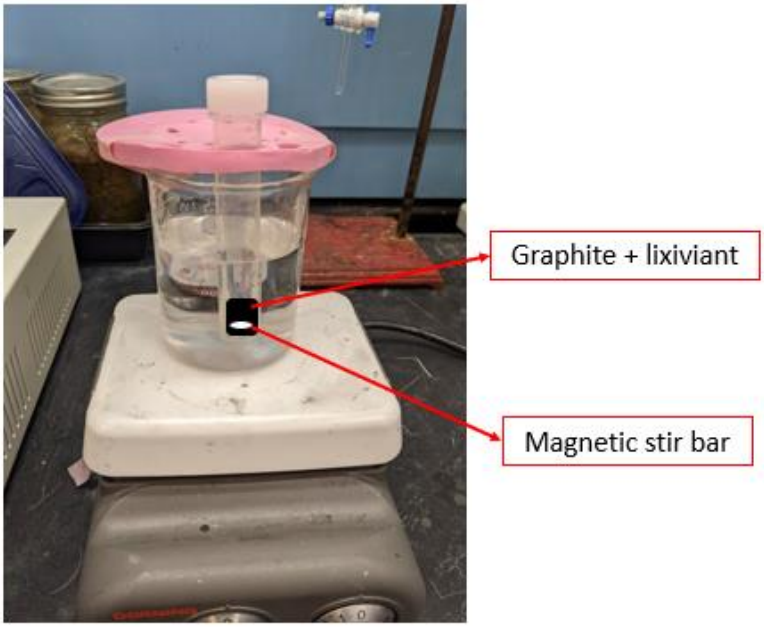

Figure 8-1. Experimental setup for the two-step leaching process.

After leaching, vacuum filtration (Buchner funnel with Grade GF/F 0.7 um, 41.5 mm diameter filter paper) separated the leached solids from the PLS. The PLS was collected into a second Teflon tube. The leached graphite solid was triple rinsed with RO water. The leached and rinsed graphite was dried for 20 minutes before mass measurement. The graphite was then placed into a new Teflon tube. The residual filter paper was weighted again to determine the total mass of graphite solid transferred to the tube. The graphite loss was accounted for in the component mass balance to calculate the extracted % of impurities. This same procedure was repeated for the second leaching step. All error bars denote ± 1 standard deviation.

8.4 Results and Discussion

Characterization of the PLS composition, and leached graphite XRD, SEM, and EDS results are discussed.

8.4.1 Pregnant leaching solution composition

The Fe, Si, and Al concentrations in the PLS are shown in Figure 8-2.

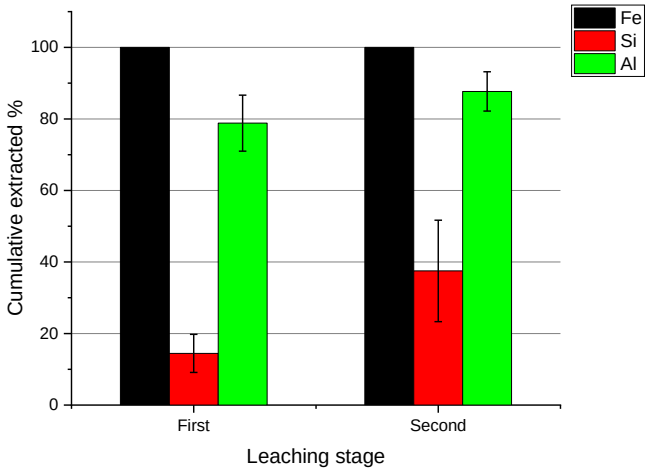

Figure 8-2. Cumulative extraction percent of Fe, Al, and Si after an agitated two-stage leaching process that prioritized Al leaching in the first stage, and Si extraction in the second stage n = 4.

Agitation increased the extraction percent of Al and Si compared to the similar but quiescent two stage leaching process presented in Section 7.3.3. Approximately 85 ± 5.5% of Al and 38 ± 14% of Si was extracted after the second leaching stage. Compared to the extraction percent results in Section 7.3.3, agitation improved the extraction % by approximately 5% for Al and 10% for Si.

8.5 Leached graphite solid characterization

The full powder XRD pattern (from 5 to 60 °2θ) is shown in Figure 8-3. The d_{002} spacing shifted from 0.333 nm to 0.336 nm after leaching.

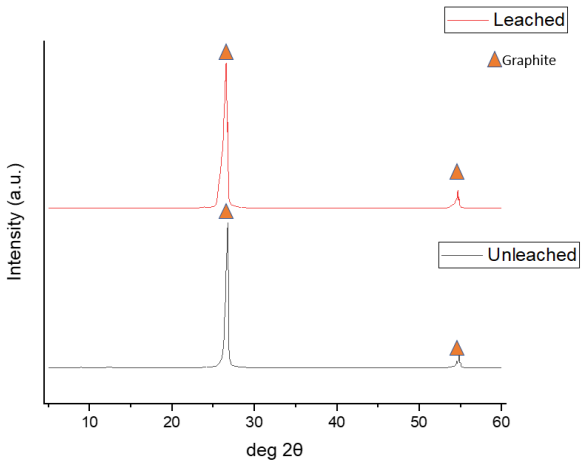

Figure 8-3. Powder XRD results of the initial (black) and two-stage leached (red) graphite. Major graphite peaks are labeled with a triangle.

From Figure 8-3, the graphite peak at 27 °2θ shifted to the left slightly after leaching. This peak shift may be caused by reduction of crystallinity – a process called "de-graphitization" [164, 165].

Figure 8-4 presents the XRD diffraction data between 6 and 24 °2θ. This range includes major peaks for kaolinite and muscovite.

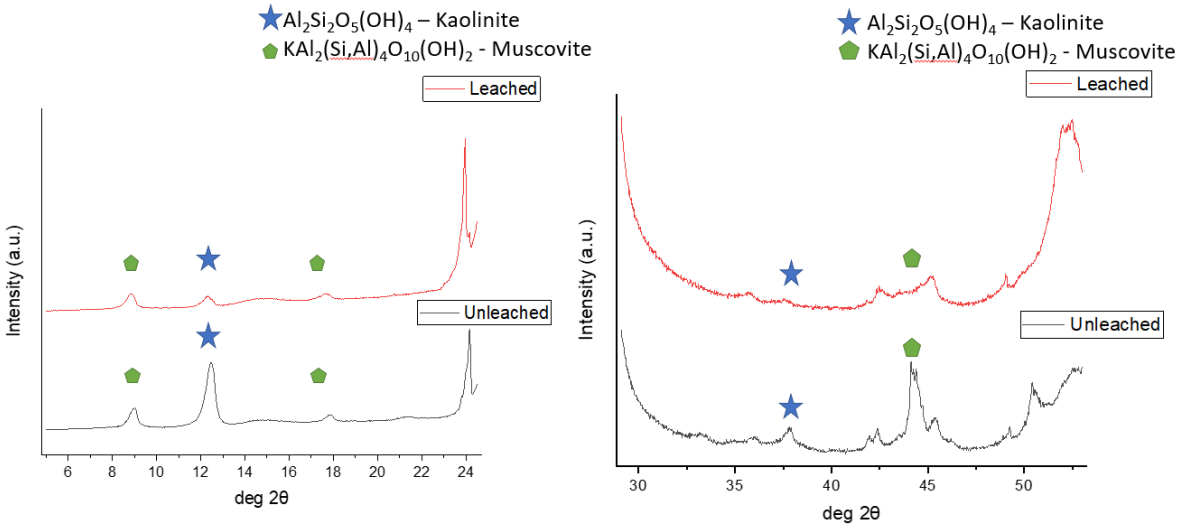

Figure 8-4. Powder XRD results of the impurity peaks, excluding graphite peaks Kaolinite peaks are marked with a star, and muscovite peaks are marked with a pentagon.

The intensities of the kaolinite peak at 12.5 and 37.6 °2θ, and the muscovite peak at 44.5 °2θ are reduced by two-stage leaching. This result confirms the detection of Si and Al in the PLS.

SEM images of the initial graphite concentrate (Figure 8-5 a) and the graphite concentrate after two-stage leaching (Figure 8-5 b) show the approximate flake size and shape.

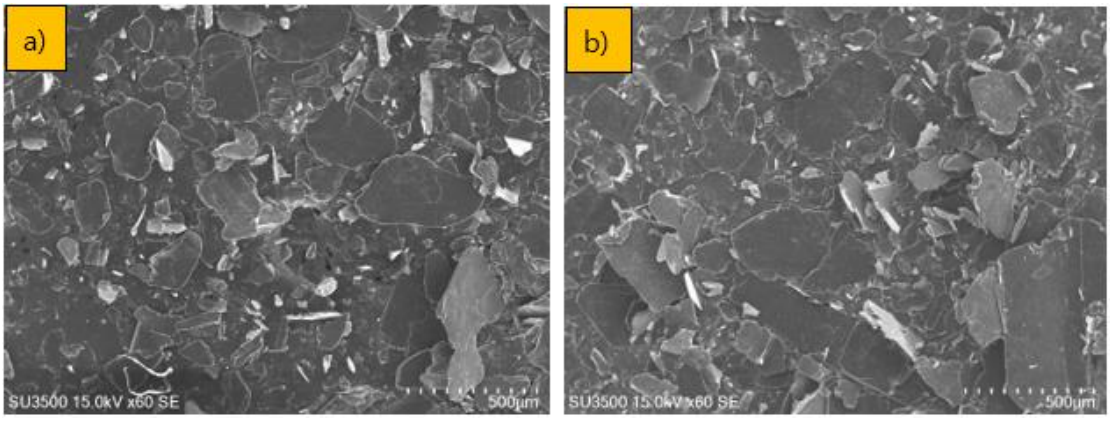

Figure 8-5. Higher resolution secondary electron images of graphite concentrate a) initial b) after agitated two-stage leaching

EDS maps of Fe, Al, C, and Si of initial graphite concentrate (Figure 8-6a) and the two-stage leached graphite product (Figure 8-6b) support the PLS and XRD results. The Fe (turquoise), Al (green), and Si(yellow) fractions in the images are reduced by agitated two-stage leaching.

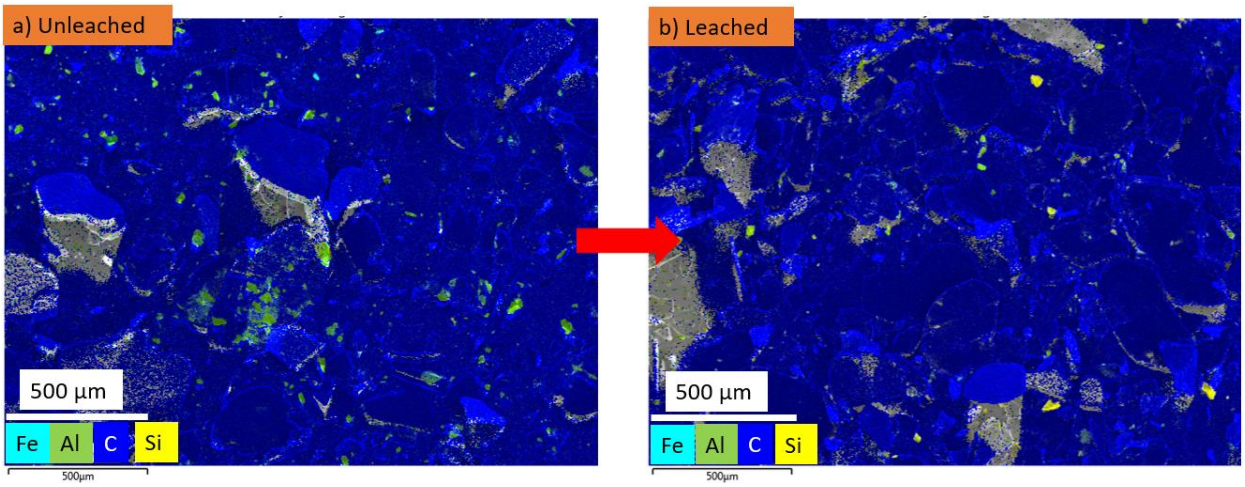

Figure 8-6. Energy Dispersive Spectroscopy (EDS) maps of Fe, Al, C, and Si of a) initial graphite concentrate and b) graphite concentrate after agitated two-stage leaching.

8.6 Conclusions

The agitated, two-step leaching process, with the first stage optimizing Al leaching, and the second stage optimizing Si leaching was undertaken. The impurity concentrations in the PLS were used to estimate the extraction percent of Fe, Al, and Si. After agitation and a two-stage leaching, Fe extraction was 100%, Al extraction was 95%, and Si extraction was 43%. Agitation improved Al and Si extraction % by approximately 20%. The leached graphite showed evidence of silicate leaching by powder XRD, and Fe, Si, and Al reduction by EDS.

9 Investigation of Al chelation by polyphosphate

In Chapter 50, Al leaching by polyphosphate was proposed to be caused by a chelation mechanism. The alumina layer of kaolinite was proposed to interact with polyphosphate, which enhanced aluminum ion dissolution. Both polyphosphate and phosphate ions are presumed to promote kaolinite dissolution by ligand exchange. Stable and soluble bidentate ligands between polyphosphate or phosphate and Al may enhance Al dissolution.

To support this proposed mechanism, ^{31}P nuclear magnetic resonance (^{31}P NMR) was used with a natural kaolinite sample to study the change in the chemical environment in the phosphate-polyphosphate-aluminum containing lixiviant.

Table 9-1. Author Statement

Conceptualization, Writing (Review & Editing)	Hak Jun Oh Associate Professor Sidney Omelon
Investigation	Hak Jun Oh Dr. Robin Stein (NMR Facility Manager)
Writing (Original Draft)	Hak Jun Oh
Methodology	Hak Jun Oh Dr. Robin Stein (NMR Facility Manager) Sidney Omelon

9.1 Goal

The goal is to study the ^{31}P NMR spectral ranges corresponding to the Al-polyphosphate/phosphate interactions and identify the types of chemical groups and bonding environments. Natural kaolinite and a lixiviant with phosphoric acid and polyphosphate were used in this study to identify the interactions of the phosphorus compounds with kaolinite surfaces.

9.2 Theory

Nuclear magnetic resonance (NMR) is a powerful analytical technique used for the structure determination in a broad spectrum of research fields including chemical and physical sciences [166]. Due to the high sensitivity of NMR, nearly all elements and matrices could be studied by NMR spectroscopy [166]. The principle behind NMR lies within nuclei with electron spins and their electrically charged characteristic [167]. When an external magnetic field (at a radio frequency) is applied, there is an excitation of nuclear spin energy levels from an equilibrium state to an excited state due to energy transfer. Once the excited spin returns to equilibrium, the absorbed

energy is reemitted at the same frequency, and this is processed and converted to a signal in the NMR spectrum [167].

There are spectral regions on the ^{31}P spectrum that will be useful for the identification of the Al-polyphosphate/phosphate interactions. The regions have been summarized in the study by de Oliveira Lima et al. [151]:

Chemical shift (ppm)	Assignment (reference or rationale for the assignment)
0.63 to 0.66	Free orthophosphate (9–13)
−6.0 to −8.0	Bound orthophosphate (also observed in aluminum orthophosphate solutions, not shown)
−10.0 to −11.5	Free chain end-groups, including pyrophosphate (10–12)
−13.0 to −15.0	Bidentate bound end-groups (based on the assignment of free end-groups and on the shift introduced by deshielding, analogous to orthophosphate)
−16.0 to −17.0	Bridging (bound to 2 Al ions) pyrophosphate (also observed in Al pyrophosphate solutions, not shown)
−18.0 to −22.0	Monodentate bound end-groups (Al ions should have a stronger deshielding effect on monodentate end-groups than on bidentate groups)
−21.0 to −22.0	Free cyclic metaphosphates (13)
−23.0 to −24.0	Free middle-chain groups (9–12)
−23.0 to −28.0	Bidentate bound middle-chain groups and free middle-chain groups neighbors to Al-bound groups (both refer to middle-chain groups deshielded by Al ions, but to a lesser extent than monodentate groups)
−30.0 to −36.0	Bound monodentate middle-chain groups (strongly deshielded by Al ions)

Figure 9-1. Peak assignments in ^{31}P-NMR of aluminum-polyphosphate solutions in acidic condition [151]

9.3 Methods

Different mixtures of Al, polyphosphate, and phosphate, including a lixiviant of 2 M phosphoric acid and 1.9 M ($NaPO_3$) polyphosphate and natural kaolinite (Sigma-Aldrich), and a 3 mL of lixiviant was used for all samples. The following five samples were analyzed with ^{31}P NMR and conditions:

1. Blank control: lixiviant (2 M phosphoric acid and 1.9 M $NaPO_3$ of sodium polyphosphate)
2. Negative control: 0.1 g of silicon powder (crystalline, -325 mesh, 99.999% purity from Fisher Scientific, CAS: 7440-21-3) and lixiviant.
3. Positive control: Aluminum nitrate (1000 ppm, or 1000 mg/L) dissolved in the lixiviant.
4. Heated leaching of Kaolinite: 0.5 g of kaolinite powder (pulverized natural kaolinite, Sigma-Aldrich CAS: 1318-74-7) leached at 80 ^oC for 2 hours.
5. Room temperature leaching of Kaolinite: 0.5 g of kaolinite powder (pulverized natural kaolinite, CAS: 1318-74-7) leached at room temperature (~20 ^oC) for 2 hours.
6. Heated Positive control: Aluminum nitrate (1000 ppm, or 1000 mg/L) dissolved in the lixiviant.

The PLS was vacuum filtered The PLS samples were mixed with deuterium water (DW) at a volume ratio of 9 to 1 (0.9 mL of PLS with 0.1 mL of DW) in a microcentrifuge tube. The solutions were vortexed and pipetted into NMR tubes.

9.4 Results and Discussion

Each of the five ^{31}P NMR spectra will be studied to understand the chemical environments of phosphorus in each solution.

Figure 9-2 shows two example spectra, and labels the chemical shift ranges with the attributed chemical environments. Free orthophosphates are used to denote the 0 ppm chemical shift baseline. As the chemical shift values decrease, the next P-group is orthophosphates bound to another moiety (~-6 to -8 ppm). The chain-terminating, or “end” P-groups of polyphosphates are attributed to chemical shifts from -10 to -12 ppm. End P-groups associated with a monodentate bond are attributed to chemical shifts from -21.5 to -22.5 ppm. -23 to -24.5 ppm shifts are associated with free or bidentate-bound polyphosphate mid-chain P.

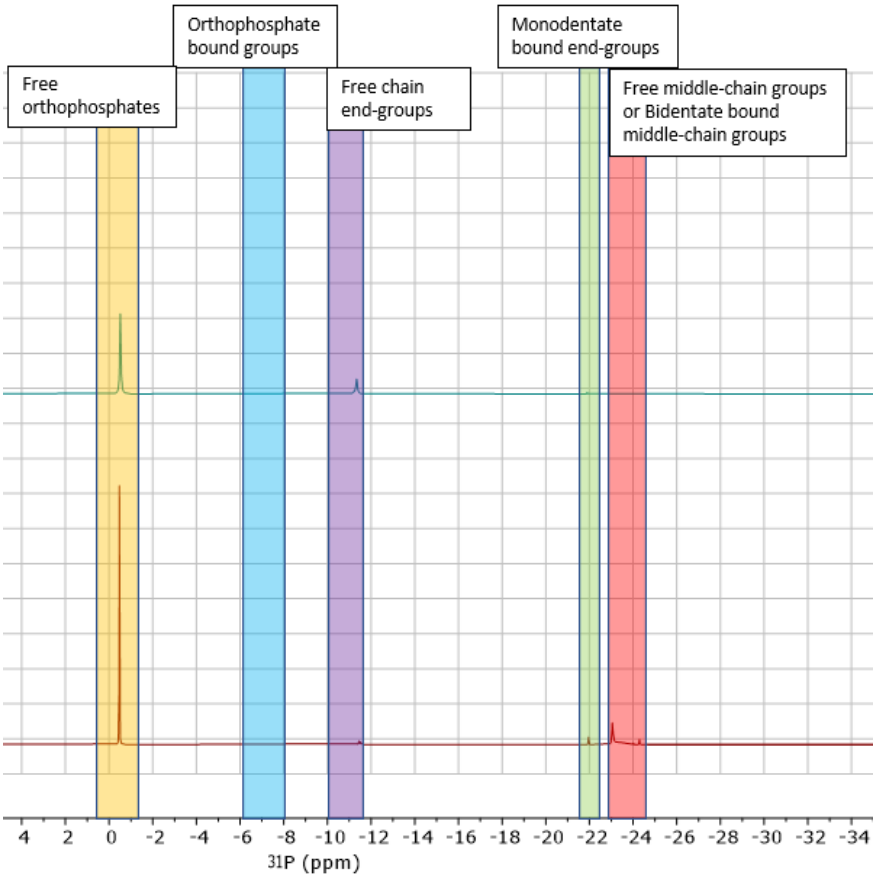

Figure 9-2. Summary of selected spectral ranges and attributions for ^{31}P NMR

Figure 9-3 shows the ^{31}P NMR results for the blank (1: lixiviant), positive control (2: aluminum nitrate in the lixiviant), and negative control (3: silicon powder in the lixiviant). Four distinctive peaks were observed These corresponds to free orthophosphates (~ - 0.5 ppm), free chain end group and pyrophosphates (- 11.2 ppm), monodentate bound end-groups of polyphosphates (-21.9 ppm), and bidentate bound middle-chain groups (- [23.0 – 28.0] ppm). The spectral region for free orthophosphate (~ - 0.5 ppm) is different from what was suggested in the previous study by Lima (~ + [0.63 – 0.66] ppm) [151]. However, a chemical shift could have been induced due to acidic matrix of the analyte, hence -0.5 ppm is assumed to be corresponding to the free orthophosphate [168].

In Figure 9-3 and Figure 9-4, the NMR results of the blank control, positive control, and negative control are presented.

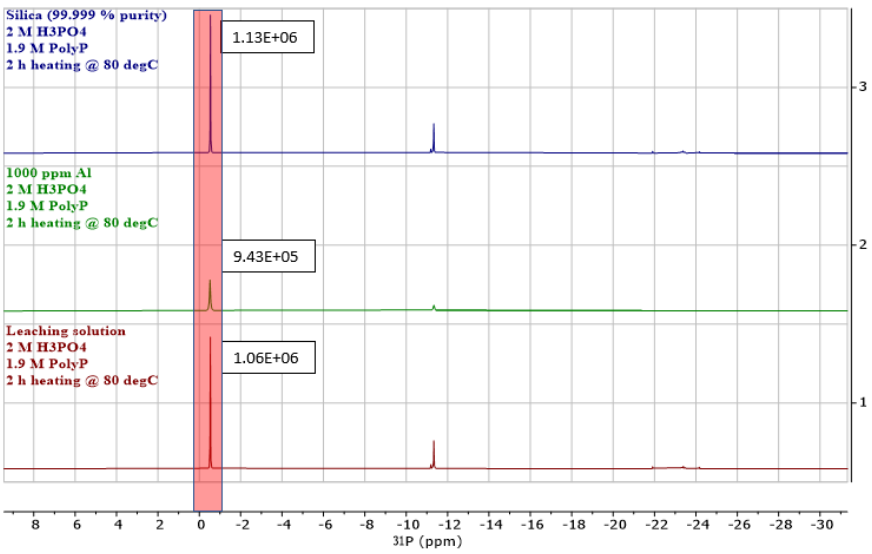

Figure 9-3. Overview of the NMR results of blank (1), positive control (2), and negative control (3), and with areas under the curve calculated for peaks corresponding to free orthophosphates

Figure 9-4 shows the same spectra from -5 to -25 ppm, zoomed in on the y-axis. The peak areas are also presented. These peak areas can be correlated with concentration. The polyphosphate peaks are generally less intense than the largest orthophosphate peak. The orthophosphate peak intensity was reduced by addition of 1000 ppm Al^{3+}. The multivalent Al ion is capable of associating with multiple orthophosphate and/or polyphosphate molecules. [169]. Al ions principally bind to middle-chain groups with long polyphosphate chains [170].

The intensities of the ^{31}P NMR peaks for the positive control were generally less intense than the negative and blank controls. The free orthophosphate peak at – 0.5 ppm of the aluminum ion containing positive control has less intensity than the other two controls. This result could suggest orthophosphate dentate formation. The peaks at - [23.0 – 28.0] ppm for the positive control should be greater than blank and negative control due to bidentate formation. However, the contrary was observed, and this could be due to the greater concentration of the free mid-chain PO_3^- groups. The Al^{3+} concentration is 1000x lower than the concentration of phosphorus in the lixiviant, meaning the NMR signals of the formed dentates could be relatively small.

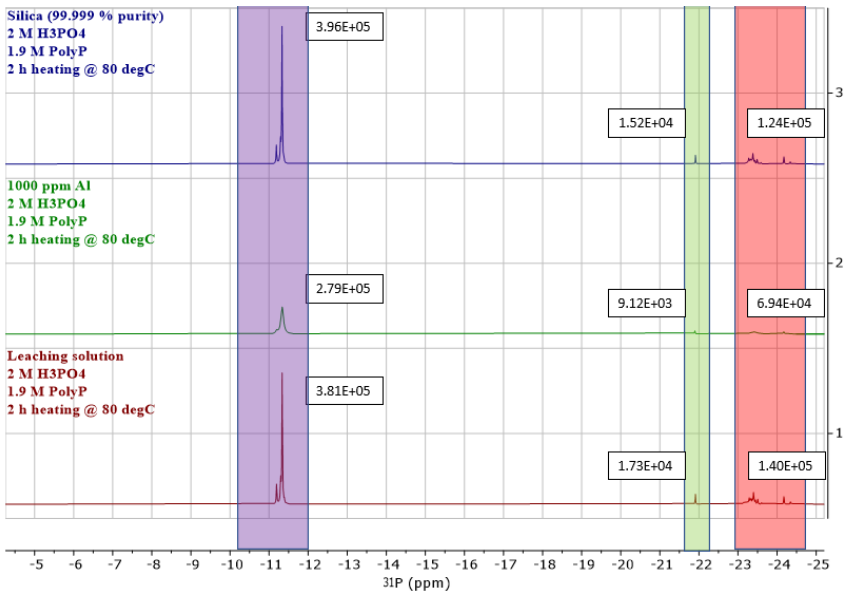

Figure 9-4. Vertically magnified ^{31}P NMR results for blank (1), positive control (2), and negative control (3). Areas under the curve are calculated for free end-group polyphosphates (-[10.0 - 11.5]) and monodentate end-group bound (–[18.0 – 22.0] ppm) & bidentate forming middle-chain groups or free middle-chain groups (-[23.0 – 28.0] ppm)

The x-axis (-2.5 to -10.5 ppm) and y-axis zoom in Figure 9-5 show the chemical shifts in the orthophosphate-bound spectral region (- [6 - 8] ppm). The identification of a chemical shift peak for the positive control proves the presence of Al-orthophosphate dentate bonds. A strong presence of bidentate end-group (- [13.0 – 15.0] ppm) was observed for the positive control, while the negative and blank controls did not show any presence of Al-bidentate end-group presence. The results shown in Figure 9-5 suggest that phosphates form complexes with Al. The working concentrations of phosphoric acids used for the DOE runs are non-negligible, thus it is likely that phosphates are partially or fully protonated as discussed in Chapter 4.

Figure 9-6 x-axis zoom from -12 to -15.7 ppm explores the chemical shifts of the bidentate end-groups of polyphosphate (-[13.0 – 15.0] ppm). This shift is observed only for the aluminum-containing positive control group.

The complexation of aluminum with phosphate could be described as partially protonated phosphates complexing with free Al ions. The remaining valence electrons of aluminum ion is compensated by the surrounding water molecules. In Chapter 4, protons were mentioned as charge neutralizers, and other free counter ions, such as Na^{+}, Al^{3+}, and Ca^{2+}, may compete for the binding sites on either polyphosphate or phosphate ions.

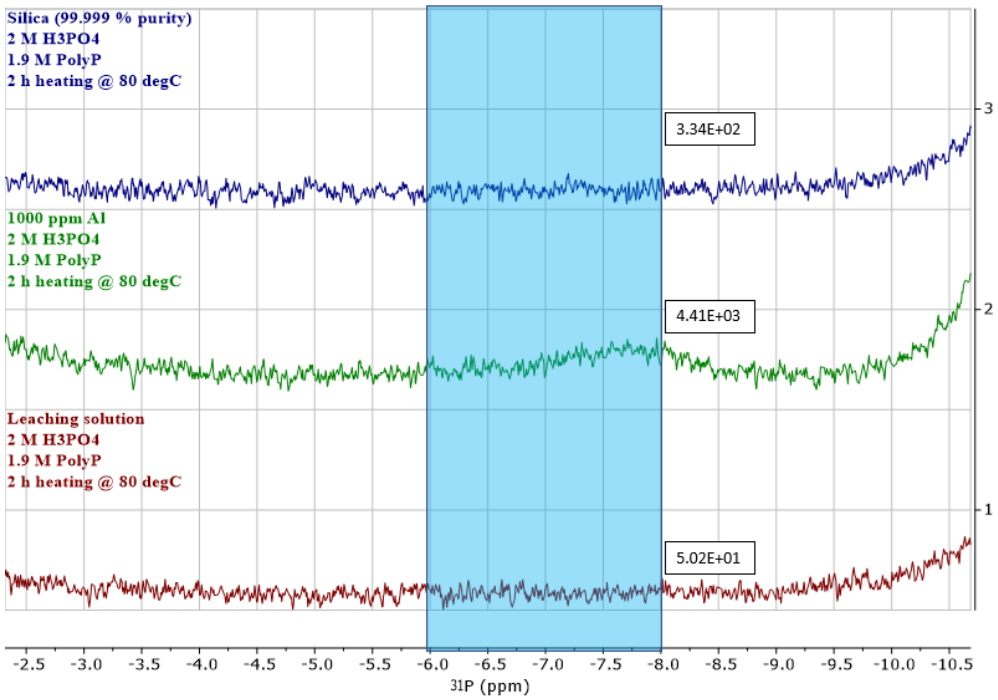

Figure 9-5. NMR result a spectral range – 6.0 to – 8.0 vertically magnified for negative (3), positive (2), and blank (1) controls with areas under the curve calculated for bound orthophosphates (-[6.0 – 8.0] ppm)

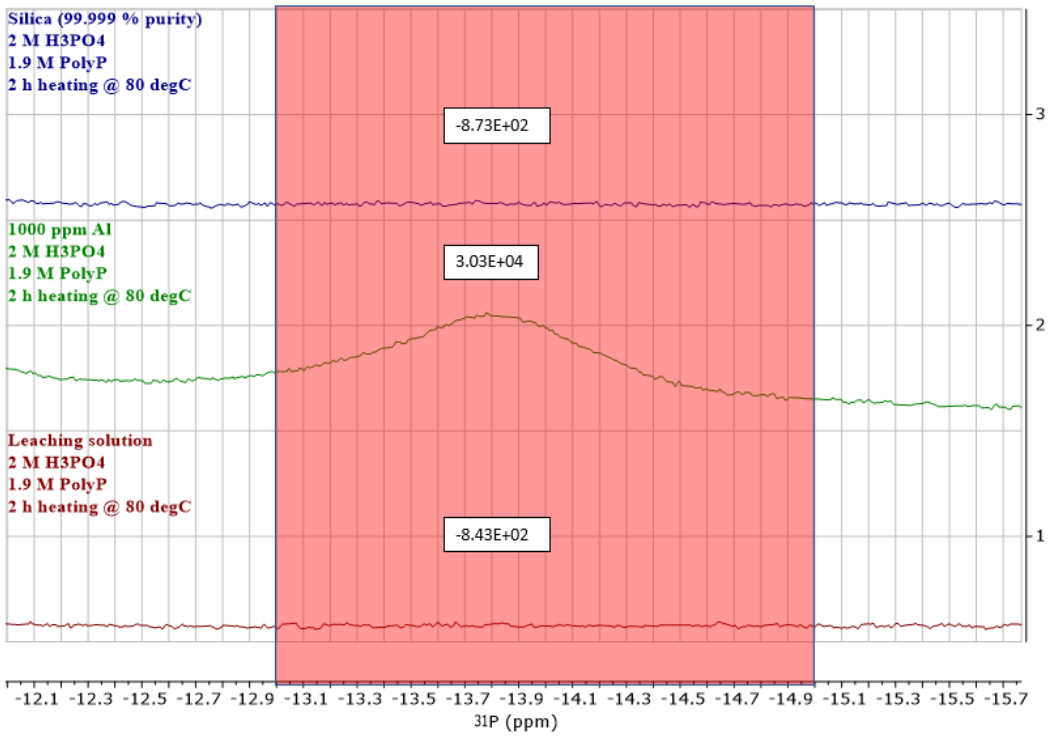

Figure 9-6. NMR results of spectral ranges – 13.0 to – 15.0 vertically magnified for negative (3), positive (2), and blank (1) controls with areas under the curve calculated for bidentate end-groups of polyphosphate (-[13.0 – 15.0] ppm)

Figure 9-7 shows the possible mono-, di- and tri-dentate species of Al-phosphate at low pH.

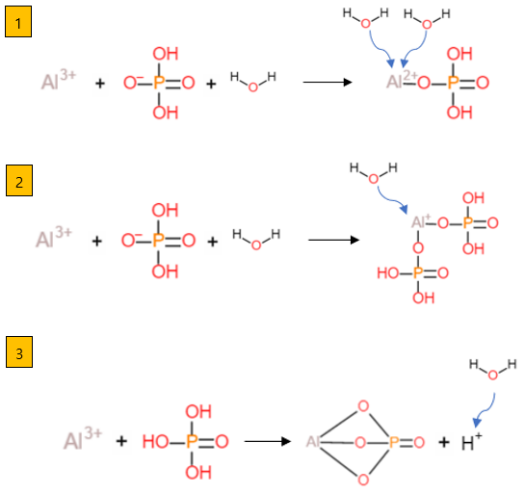

Figure 9-7. Possibilities of Al-phosphate complexation at low pH range (< pH 2). Three cases presented: 1) Al-$H_2PO_4^{2+}$, 2) Al-$(H_2PO_4)_2^{+}$, and 3) $AlPO_4$

The presented cases of aluminum ion complexation with phosphate ion are supported by the study by Akitt et al. [171]. The author proposed that in cases where the free Al concentration is high, Case 3 in Figure 9-7 is the dominant case. When all of the free Al ions are complexed, Case 1 and Case 2 species are possible due to competition for Al^{3+}. The complex speciation between orthophosphate, polyphosphate, and aluminum ions as a function of phosphoric acid concentration is summarized in Figure 9-8.

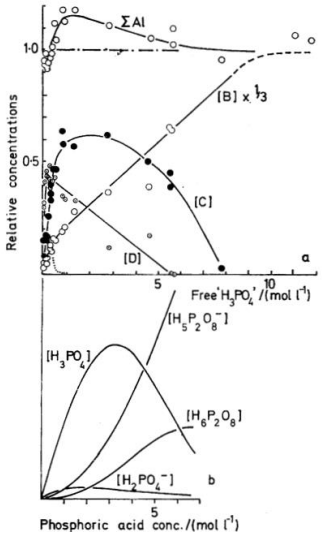

Figure 9-8. Complex speciation according to the free H_3PO_4 concentration. [B] is Al-polyphosphate, [C] is $AlH_2PO_4^{2+}$ and $Al(H_2PO_4)^{2+}$, and [D] is $AlPO_4$ [171]

The ^{31}P NMR results from Samples 3 & 6 (80 °C and room temperature positive control with aluminum ion, Figure 9-9. ^{31}P NMR result of the temperature effect on the positive control with curve areas. 1) Positive control (sample 3) at room temp. 2) Heated positive control (sample 6) 80 ºC, 2Figure 9-9) and 4 & 5 (80 °C and room temperature kaolinite leach, Figure 9-9. ^{31}P NMR result of the temperature effect on the positive control with curve areas. 1) Positive control (sample 3) at room temp. 2) Heated positive control (sample 6) 80 ºC, 2Figure 9-9) are presented.

The NMR results presented Figure 9-9 (room temperature and heated positive control samples) and Figure 9-10 (room temperature and heated kaolinite samples), both with x-axis zooms from -16 to -34 ppm agree confirm that elevated temperature increases the polyphosphate chain hydrolysis rate [111]. This is concluded from the increases in the area under the curve for the free orthophosphate peak at - 0.5 ppm and the free chain end-group including pyrophosphate at -11 ppm relative to the decreases in the area under the curve for the monodentate bound end-groups at - 21.9 ppm and a bidentate bound middle-chain groups between - [23.0 – 28.0].

The breakdown of polyphosphates into phosphate ions could have led to greater probability to form Al-phosphate complexes as seen by the increase in the area under the curve in the spectral region between - [6 – 8] ppm. The peak at - 11.5 ppm corresponds to free chain end-groups including pyrophosphate [151]. It is seen that this area under the curve increases after the heat cycle. This may be explained by the structural stability that the bidentate Al ion with the polyphosphate offers, which would favor the hydrolysis of the stable symmetrical structure of pyrophosphate [46].

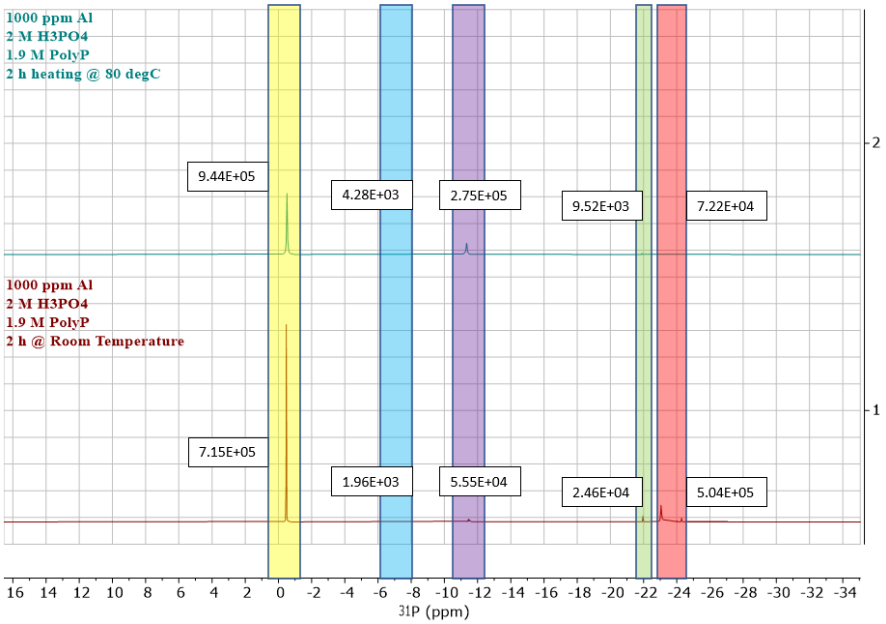

Figure 9-9. ^{31}P NMR result of the temperature effect on the positive control with curve areas. 1) Positive control (sample 3) at room temp. 2) Heated positive control (sample 6) 80 ºC, 2 h.

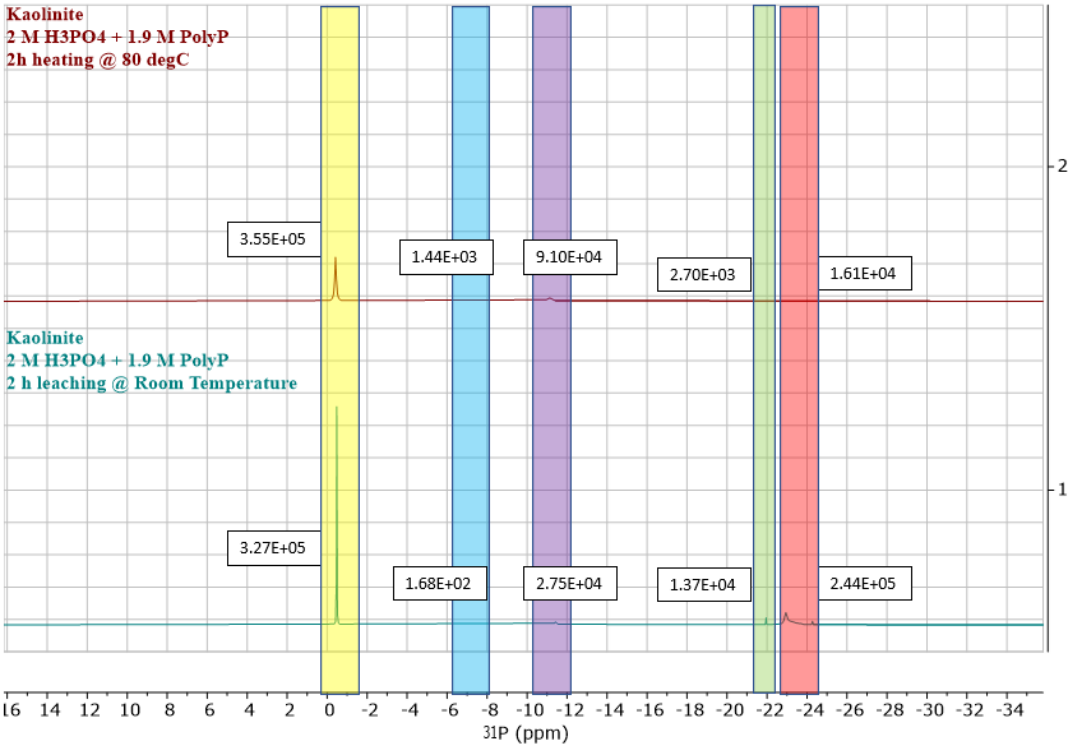

Figure 9-10. ^{31}P NMR result of the temperature effect on kaolinite leaching with the curve areas values. 1) Kaolinite leaching at room temperature 2) Kaolinite leaching for 2 h at 80 ºC

Figure 9-11 shows The formation of Al-pyrophosphate as an Al-polyP hydrolytic degradation product. After the breakdown of the bidentate polyphosphate, the Al ion enters competition with

other dissolved ions for the binding sites, and Al ion may dissociate from the pyrophosphate. For the simplicity, the – 11.5 ppm peak is assumed to be only for free pyrophosphates.

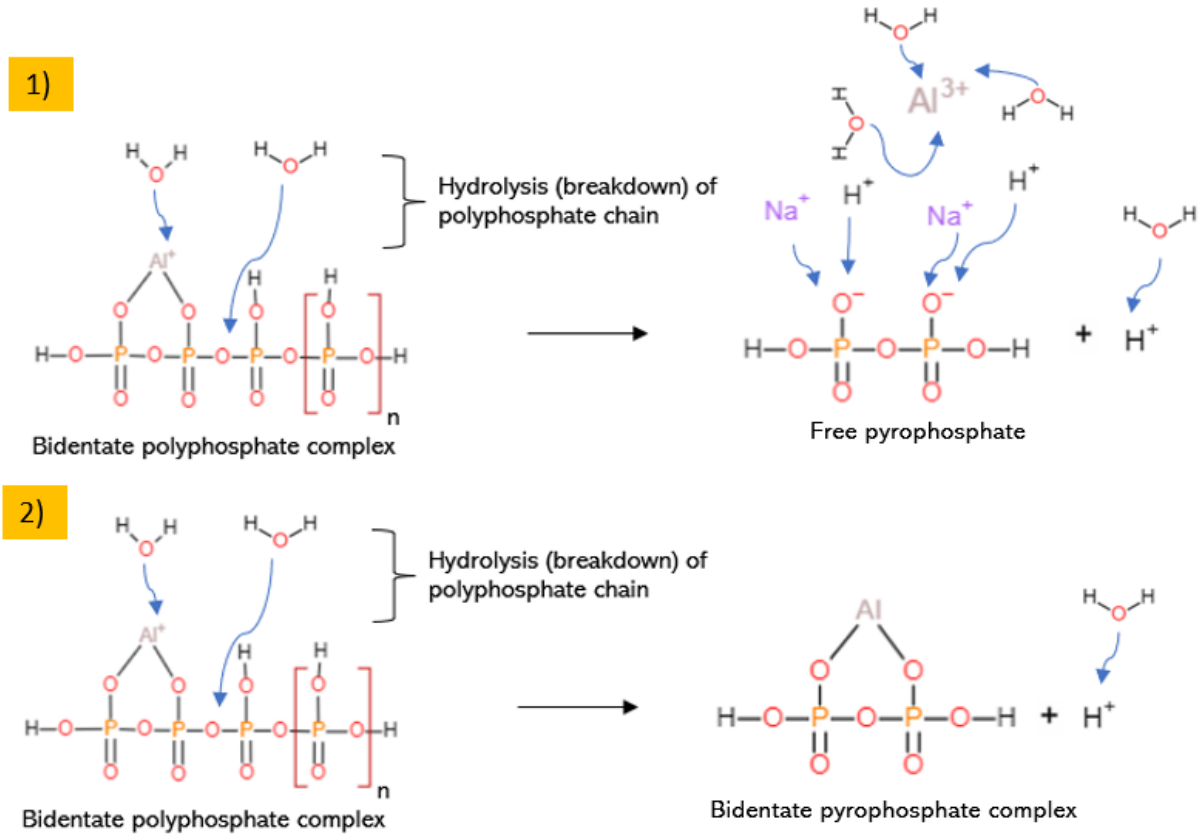

Figure 9-11. Two proposed cases for the free and bidentate pyrophosphate formations.

The bidentate pyrophosphate complex with Al should not be discounted as a hydrolytic degradation product as described by the second case in Figure 9-11. Evidence for an ion-paired pyrophosphate was verified by the vertical magnification of the spectral regions between – [13.0 – 15.0] ppm in Figure 9-12.

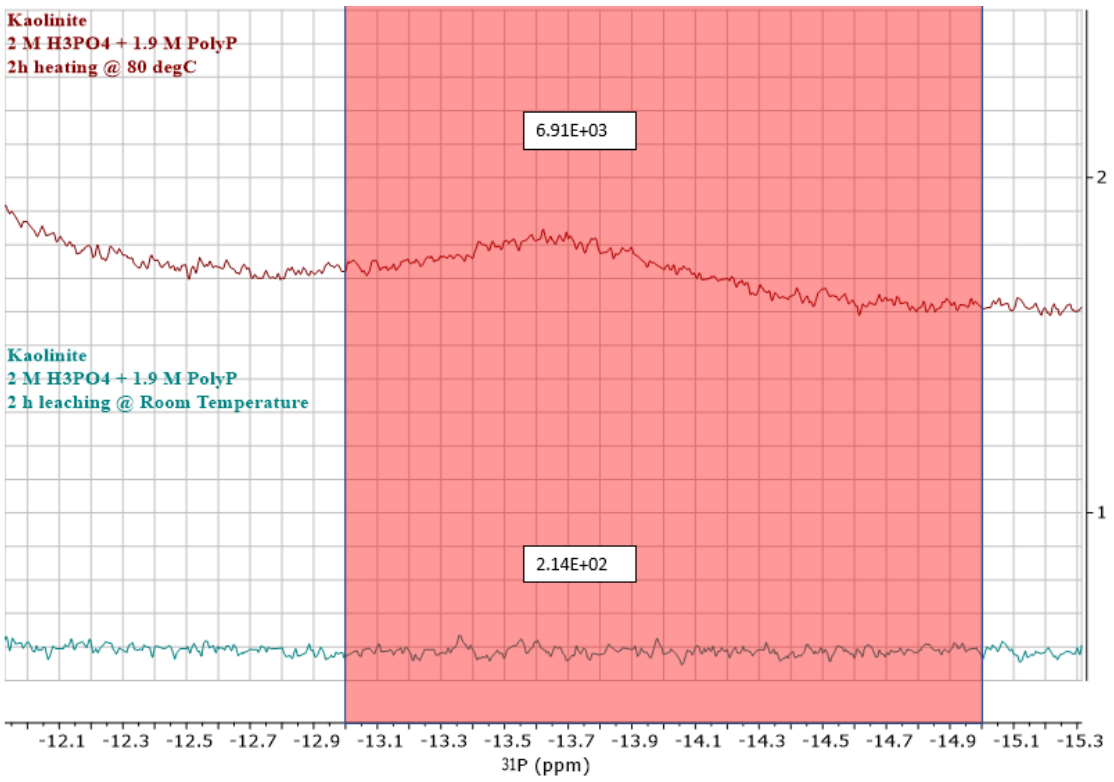

Figure 9-12. NMR result a spectral range – 13.0 to – 15.0 vertically magnified for kaolinite with/without the heat cycle with areas under the curve calculated for bidentate end-groups of pyrophosphate (- [13.0 – 15.0] ppm)

9.5 Conclusions

^{31}P-Nuclear magnetic resonance analysis was performed to study the chemical shifts corresponding to Al-polyphosphate, pyrophosphate, and phosphate interactions. The results provide evidence of the presence of Al-orthophosphate bound groups and Al-bidentate bound middle-chain groups in the kaolinite leached solution. The positive control included orthophosphate-bound group and bidentate end-group shifts with generally less available free phosphate groups to form dentates. ^{31}P NMR results after heating the sample to 80 °C for 2 h confirmed that elevated temperature increases the polyphosphate hydrolysis into smaller chains and/or orthophosphate molecules. Two scenarios were proposed to explain the increased presence of free pyrophosphates and bidentate end-groups. Liquid ^{29}Si NMR measurement was not attempted due to isotope rarity of ^{29}Si (less than 5% is measurable). Iron NMR measurement is impossible due to its magnetic property.

10 Conclusions and Future Work

10.1 Conclusions

Natural graphite concentrate can be leached by aqueous phosphorus chemistry. DoE was conducted to optimize the process parameters of graphite leaching. Kaolinite ($Al_2Si_2O_5(OH)_4$) and sulphidic iron (FeS_x) were considered to be the main impurities of the graphite concentrate that was the subject of this study. With agitated two-stage leaching that first prioritized aluminum leaching, then silicate leaching, up to 100% of iron extraction, 85 ± 5.5% of aluminum extraction, and 38 ± 14% % of silicon (as silicate) extraction were achieved in 5 h with a S:L of 7 at 100 °C using 5 M and 1 M H_3PO_4. Slurry agitation during leaching enhanced extraction of Al by 5% and Si by 10%. The initial purity of natural graphite concentrate was 96%. The final purity needs to be further investigated with ash analysis. The d_{002} spacing shifted from 0.333 nm to 0.336 nm after leaching. The results of a ^{31}P solution NMR study confirmed the hypothesis that Al-phosphate bidentate ion pairs form in solution, and that polyphosphate hydrolyses into smaller subunits.

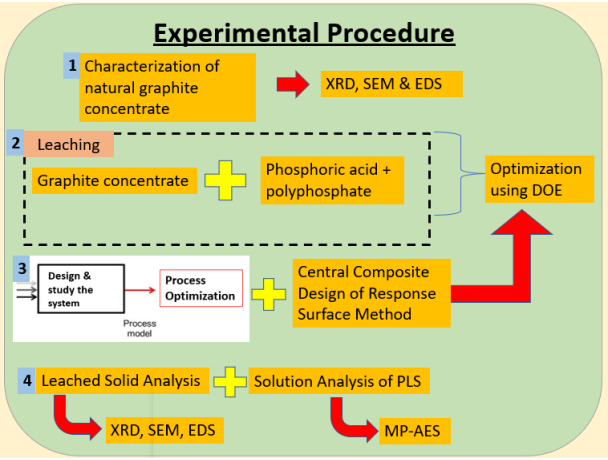

Figure 10-1. Flowchart of the workflow that identified the proposed graphite purification process

10.2 Future work

For future work, the study of Raman spectroscopy of the agitated two-staged leached graphite concentrate could verify the quality of the graphite (presence of defects) after chemical treatment. In-depth investigation of the kaolinite dissolution mechanism with ^{31}P-NMR analysis would be helpful for the understanding of phosphorus chemistry-aluminosilicate interaction. Moreover, revisiting DoE with stirring effect could be a possibility to further optimize the graphite leaching process. Lastly, graphite leaching study with other chelating agents to encourage impurity dissolution such as EDTA could lead to other sustainable approaches to purify natural graphite.

11 References

[1] C. J. Mitchell, "Industrial Minerals Laboratory Manural: Flake Graphite," Overseas Development Administration under the ODA/BGS Technology Development and Research Programme, 1993.

[2] A. D. Jara, A. Betemariam, G. Woldetinsae, and J. Y. Kim, *International Journal of Mining Science and Technology,* vol. 29, no. 5, pp. 671-689, 2019, doi: 10.1016/j.ijmst.2019.04.003.

[3] H. Wang, Q. Feng, K. Liu, K. Zuo, and X. Tang, *Separation Science and Technology,* vol. 53, no. 6, pp. 982-989, 2018.

[4] S. Chehreh Chelgani, M. Rudolph, R. Kratzsch, D. Sandmann, and J. Gutzmer, *Mineral Processing and Extractive Metallurgy Review,* vol. 37, no. 1, pp. 58-68, 2015, doi: 10.1080/08827508.2015.1115992.

[5] A. D. Jara and J. Y. Kim, *Materials Today Communications,* vol. 25, 2020, doi: 10.1016/j.mtcomm.2020.101437.

[6] A. Kozbial, F. Zhou, Z. Li, H. Liu, and L. Li, *Accounts of Chemical Research,* vol. 49, no. 12, pp. 2765-2773, 2016/12/20 2016, doi: 10.1021/acs.accounts.6b00447.

[7] Entegris. *Properties and characteristics of graphite*. (2013). [Online]. Available: https://www.entegris.com/content/dam/web/resources/brochures/brochure-properties-and-characteristics-of-graphite-7329.pdf

[8] S. Natarajan and V. Aravindan, *Advanced Energy Materials,* vol. 10, no. 37, p. 2002238, 2020.

[9] T. Qiu, J.-G. Yang, X.-J. Bai, and Y.-L. Wang, *RSC advances,* vol. 9, no. 22, pp. 12737-12746, 2019.

[10] P. Ouzilleau, A. E. Gheribi, P. Chartrand, G. Soucy, and M. Monthioux, *Carbon,* vol. 149, pp. 419-435, 2019.

[11] X. Wang, G.-S. Gai, Y.-F. Yang, and W.-C. Shen, *Powder Technology,* vol. 181, no. 1, pp. 51-56, 2008/01/30/ 2008, doi: https://doi.org/10.1016/j.powtec.2007.06.025.

[12] H. Wang, Q. Feng, X. Tang, and K. Liu, *Separation Science and Technology,* vol. 51, no. 14, pp. 2465-2472, 2016/09/21 2016, doi: 10.1080/01496395.2016.1206933.

[13] S. M. Bulatovic, *Handbook of Flotation Reagents: Chemistry, Theory and Practice: Volume 3: Flotation of Industrial Minerals*. Elsevier, 2014.

[14] R. Bhima Rao and N. Patnaik, *Scandinavian Journal of Metallurgy,* vol. 33, no. 5, pp. 257-260, 2004, doi: https://doi.org/10.1111/j.1600-0692.2004.00697.x.

[15] W. Xie *et al.*, *International Journal of Mineral Processing,* vol. 155, pp. 45-54, 2016.

[16] S. Zhou *et al.*, *Minerals Engineering,* vol. 158, p. 106592, 2020.

[17] B. G. Kim, S. K. Choi, C. L. Park, H. S. Chung, and H. S. Jeon, *Particulate Science and Technology,* vol. 21, no. 4, pp. 341-351, 2003, doi: 10.1080/716100574.

[18] N. Aslan, F. Cifci, and D. Yan, *Separation and Purification Technology,* vol. 59, no. 1, pp. 9-16, 2008, doi: 10.1016/j.seppur.2007.05.022.

[19] R. J. Pugh, *Minerals Engineering,* vol. 13, no. 2, pp. 151-162, 2000.

[20] X. J. Lu and E. Forssberg, *Minerals Engineering,* vol. 15, no. 10, pp. 755-757, 2002/10/01/ 2002, doi: https://doi.org/10.1016/S0892-6875(02)00172-3.

[21] J. Kirkpatrick, D. Enion, and D. Burd, *Burns,* vol. 21, no. 7, pp. 483-493, 1995.

[22] Ö. Kaya and M. Canbazoğlu, *Mining, Metallurgy & Exploration,* vol. 26, no. 3, pp. 158-162, 2009.

[23] D. Aquilano, F. Otálora, L. Pastero, and J. M. García-Ruiz, *Progress in Crystal Growth and Characterization of Materials,* vol. 62, no. 2, pp. 227-251, 2016/06/01/ 2016, doi: https://doi.org/10.1016/j.pcrysgrow.2016.04.012.

[24] Z. Wu and K. M. Steel, *Fuel,* vol. 86, no. 14, pp. 2194-2200, 2007.

[25] H. T. Thi and N. Hong, *World Journal of Research and Review,* vol. 5, no. 1, p. 262781, 2017.

[26] E. Bolat, S. Sağlam, and S. Pişkin, *Fuel Processing Technology,* vol. 57, no. 2, pp. 93-99, 1998.

[27] C. Xu, W. Yang, W. Liu, H. Sun, C. Jiao, and A.-j. Lin, *Journal of Environmental Sciences,* vol. 67, pp. 14-22, 2018.

[28] A. C. Dorenfeld, "Process for purifying graphite," U.S., 1957. [Online]. Available: https://patents.google.com/patent/US2787528A/en

[29] N. Xiaoxia, C. Xiuju, Z. Jun, and W. Lifang, *Chinese Journal of Environmental Engineering,* vol. 1, no. 7, pp. 136-140, 2007.

[30] K. S. Rao, J. Senthilnathan, Y.-F. Liu, and M. Yoshimura, *Scientific reports,* vol. 4, no. 1, pp. 1-6, 2014.

[31] X. Ma, M. Chen, B. Chen, Z. Meng, and Y. Wang, *ACS Sustainable Chemistry & Engineering,* vol. 7, no. 24, pp. 19732-19738, 2019.

[32] Y. Yang, G. Huang, S. Xu, Y. He, and X. Liu, *Hydrometallurgy,* vol. 165, pp. 390-396, 2016/10/01/ 2016, doi: https://doi.org/10.1016/j.hydromet.2015.09.025.

[33] S.-g. Zhu, W.-z. He, G.-m. Li, X. Zhou, X.-j. Zhang, and J.-w. Huang, *Transactions of Nonferrous Metals Society of China,* vol. 22, no. 9, pp. 2274-2281, 2012/09/01/ 2012, doi: https://doi.org/10.1016/S1003-6326(11)61460-X.

[34] A. Asghar, A. A. Abdul Raman, and W. M. A. Wan Daud, *Journal of Cleaner Production,* vol. 87, pp. 826-838, 2015/01/15/ 2015, doi: https://doi.org/10.1016/j.jclepro.2014.09.010.

[35] N. Patnaik, M. Patil, and R. Bhima Rao, 1997.

[36] W. H. Waggaman, *Soil Science,* vol. 74, no. 4, 1952. [Online]. Available: https://journals.lww.com/soilsci/Fulltext/1952/10000/Phosphoric_Acid,_Phosphates,_and_Phosphatic.20.aspx.

[37] R. Gilmour, *Phosphoric acid: purification, uses, technology, and economics*. CRC Press, 2013.

[38] T. Murahashi, "FUEL CELLS – PHOSPHORIC ACID FUEL CELLS | Electrolytes," in *Encyclopedia of Electrochemical Power Sources*, J. Garche Ed. Amsterdam: Elsevier, 2009, pp. 564-567.

[39] B. Campus. [Online]. Available: https://opentextbc.ca/chemistry/chapter/14-5-polyprotic-acids/?fbclid=IwAR3EzNgD6mpoeiw6SYI6IPN1CtePBA18on5qtx9TXtNN04u3QhUs5xAT-t0.

[40] D. R. Lide, *CRC handbook of chemistry and physics*. CRC press, 2004.

[41] R. Zeitoun and A. Biswas, *Journal of The Electrochemical Society,* vol. 167, no. 12, p. 127507, 2020.

[42] M. Jagtoyen, M. Thwaites, J. Stencel, B. McEnaney, and F. Derbyshire, *Carbon,* vol. 30, no. 7, pp. 1089-1096, 1992.

[43] X. Chen, H. Ma, C. Luo, and T. Zhou, *Journal of Hazardous Materials,* vol. 326, pp. 77-86, 2017.

[44] Z. Hu and L. Qi, "15.5 - Sample Digestion Methods," in *Treatise on Geochemistry (Second Edition)*, H. D. Holland and K. K. Turekian Eds. Oxford: Elsevier, 2014, pp. 87-109.

[45] P. Powell, *The Chemistry of the Non-metals*. Springer Science & Business Media, 2013.

[46] A.-L. Huhti and P. A. Gartaganis, *Canadian Journal of Chemistry,* vol. 34, no. 6, pp. 785-797, 1956, doi: 10.1139/v56-102.

[47] R. A. Krueger, L. Vilčiauskas, J.-P. Melchior, G. Bester, and K.-D. Kreuer, *The Journal of Physical Chemistry B,* vol. 119, no. 52, pp. 15866-15875, 2015/12/31 2015, doi: 10.1021/acs.jpcb.5b09684.

[48] R. Barret, "2 - Importance and Evaluation of the pKa," in *Therapeutical Chemistry*, R. Barret Ed.: Elsevier, 2018, pp. 21-51.

[49] S. S. Zumdahl and S. A. Zumdahl, *Chemistry*, 5th ed., instructor's annotated ed. / ed. Boston: Houghton Mifflin (in English), 2000.

[50] P. Hannaker and H. Qing-Lie, *Talanta,* vol. 31, no. 12, pp. 1153-1157, 1984.

[51] T. Mizoguchi and H. Ishii, *Talanta,* vol. 27, no. 6, pp. 525-528, 1980.

[52] S. Nagashima, M. Yoshida, and T. Ozawa, *Bulletin of the Chemical Society of Japan,* vol. 45, no. 11, pp. 3446-3451, 1972.

[53] C. Varadachari, *Industrial & engineering chemistry research,* vol. 31, no. 1, pp. 357-364, 1992.

[54] T. Mizoguchi and H. Ishii, *Talanta,* vol. 25, no. 6, pp. 311-316, 1978.

[55] D. C. Young, "Anhydrous liquid phosphoric acid," United States of America, 1960. [Online]. Available: https://patents.google.com/patent/US3192013A/en

[56] T. Mizoguchi and H. Ishii, *Talanta,* vol. 26, no. 1, pp. 33-39, 1979.

[57] B. E. Warren, *X-ray Diffraction*. Courier Corporation, 1990.

[58] D. A. Long, *New York,* pp. 1-12, 1977.

[59] S. Swapp, ed.

[60] B. DUTROW and C. CLARK, ed, 2019.

[61] P. Saini, R. Sharma, and N. Chadha, *Indian Journal of Pure & Applied Physics (IJPAP),* vol. 55, no. 9, pp. 625-629, 2017.

[62] R. Siburian, D. Sari, J. Gultom, H. Sihotang, S. Raja, and M. Supeno, "Performance of graphite and graphene as electrodes in primary cell battery," in *Journal of Physics: Conference Series*, 2018, vol. 1116, no. 4: IOP Publishing, p. 042034.

[63] Y. Gao *et al.*, *ACS Sustainable Chemistry & Engineering,* vol. 8, no. 25, pp. 9447-9455, 2020/06/29 2020, doi: 10.1021/acssuschemeng.0c02321.

[64] M. B. Vazquez-Santos, E. Geissler, K. Laszlo, J.-N. Rouzaud, A. Martinez-Alonso, and J. M. Tascón, *The Journal of Physical Chemistry C,* vol. 116, no. 1, pp. 257-268, 2012.

[65] K. Vernon-Parry, *III-Vs Review,* vol. 13, no. 4, pp. 40-44, 2000.

[66] H. Leamy, *Journal of Applied Physics,* vol. 53, no. 6, pp. R51-R80, 1982.

[67] J. C. Russ, *Fundamentals of energy dispersive X-ray analysis: Butterworths monographs in materials*. Butterworth-Heinemann, 2013.

[68] E.-S. Reichert, "Purification of Graphite Tailings via Alkaline or Acid Leaching Process," McGill University, Co-Op Report, August 2020.

[69] G. E. Lloyd, *Mineralogical Magazine,* vol. 51, no. 359, pp. 3-19, 1987, doi: 10.1180/minmag.1987.051.359.02.

[70] P. F. Kerr *et al.*, *Preliminary Reports: Reference Clay Minerals*. Columbia University, 1951.

[71] J. R. Craig and F. M. Vokes, *Mineralogical Magazine,* vol. 57, no. 386, pp. 3-18, 1993.

[72] M. D. R. Cruz, *Crystal structure of clay minerals and their X-ray identification,* pp. 41-52, 1980.

[73] K. Marumo, *Geochimica et Cosmochimica Acta,* vol. 53, no. 11, pp. 2915-2924, 1989/11/01/ 1989, doi: https://doi.org/10.1016/0016-7037(89)90168-3.

[74] J. W. Anthony, R. A. Bideaux, K. W. Bladh, and M. C. Nichols, *Handbook of mineralogy*. Mineral Data Publ., 2001.

[75] K. K. Neuendorf, *Glossary of geology*. Springer Science & Business Media, 2005.

[76] V. R. Troll and H.-U. Schmincke, *Journal of Petrology,* vol. 43, no. 2, pp. 243-270, 2002.

[77] D. Tunega, M. H. Gerzabek, and H. Lischka, *The Journal of Physical Chemistry B,* vol. 108, no. 19, pp. 5930-5936, 2004.

[78] X. Liu, X. Lu, M. Sprik, J. Cheng, E. J. Meijer, and R. Wang, *Geochimica et Cosmochimica Acta,* vol. 117, pp. 180-190, 2013.

[79] J. Środoń, *Encyclopedia of Earth Science,* pp. 597-601, 1999.

[80] C. Shang and L. W. Zelazny, *Methods of Soil Analysis: Mineralogical methods. Part 5,* vol. 9, p. 33, 2008.

[81] M. K. Matthiessen, F. J. Larney, L. Brent Selinger, and A. F. Olson, *Communications in soil science and plant analysis,* vol. 36, no. 17-18, pp. 2561-2573, 2005.

[82] Agilent, January 2021 ed.: Agilent, 2021.

[83] C. Bascomb, *Journal of Soil Science,* vol. 19, no. 2, pp. 251-268, 1968.

[84] M. Arshad, R. St. Arnaud, and P. Huang, *Canadian Journal of Soil Science,* vol. 52, no. 1, pp. 19-26, 1972.

[85] F. Crundwell, *Hydrometallurgy,* vol. 149, pp. 71-81, 2014.

[86] K. Kaiser and W. Zech, *Soil Science,* vol. 161, no. 7, 1996. [Online]. Available: https://journals.lww.com/soilsci/Fulltext/1996/07000/DEFECTS_IN_ESTIMATION_OF_ALUMINUM_IN_HUMUS.5.aspx.

[87] J. McGilvery and J. P. Crowther, *Canadian Journal of Chemistry,* vol. 32, no. 2, pp. 174-185, 1954.

[88] D. C. Montgomery and G. C. Runger, *Applied statistics and probability for engineers*. John wiley & sons, 2010.

[89] V. Balaram, *Microchemical Journal,* vol. 159, p. 105483, 2020.

[90] F. Crundwell, *Hydrometallurgy,* vol. 149, pp. 265-275, 2014.

[91] J. N. Laura Poirier, Greg Gilleland, Steve Wall, Lidia Berhane, and Francisco LopezLinares, "Determination of Metals in Petroleum

Fractions using MP-AES," Agilent.

[92] P.-K. F. Chin and G. L. Mills, *Chemical Geology,* vol. 90, no. 3, pp. 307-317, 1991/06/25/ 1991, doi: https://doi.org/10.1016/0009-2541(91)90106-2.

[93] N. A. Milne *et al.*, *Water research,* vol. 65, pp. 107-133, 2014.

[94] D. J. Belton, O. Deschaume, and C. C. Perry, *The FEBS journal,* vol. 279, no. 10, pp. 1710-1720, 2012.

[95] R. Y. Ning, *Desalination,* vol. 151, no. 1, pp. 67-73, 2003.

[96] W. H. Casey and C. Ludwig, *Chemical weathering rates of silicate minerals,* pp. 87-118, 2018.

[97] D. Montgomery, ed: John Wiley & Sons, Inc., Hoboken, 2019.

[98] D. Pavlov, *Lead-Acid Batteries: Science and Technology,* pp. 117-148, 2011.

[99] Avantor. https://www.avantorsciences.com/site/ (accessed Nov. 15, 2021).

[100] F. Scientific. https://www.fishersci.ca/ca/en/home.html (accessed Nov. 15, 2021).

[101] Sigma-Aldrich. https://www.sigmaaldrich.com/CA/en (accessed Nov. 15, 2021).

[102] J. R. V. Wazer and D. A. Campanella, *Journal of the American Chemical Society,* vol. 72, no. 2, pp. 655-663, 1950.

[103] S. J. Omelon and M. D. Grynpas, *Chemical Reviews,* vol. 108, no. 11, pp. 4694-4715, 2008/11/12 2008, doi: 10.1021/cr0782527.

[104] S. Omelon *et al.*, *PLoS One,* vol. 4, no. 5, p. e5634, 2009.

[105] K. S. Booksh and B. R. Kowalski, *Analytical Chemistry,* vol. 66, no. 15, pp. 782A-791A, 1994.

[106] J. R. Van Wazer and C. F. Callis, *Chemical Reviews,* vol. 58, no. 6, pp. 1011-1046, 1958.

[107] J. C. B. Pereira *et al.*, *Colloids and Surfaces A: Physicochemical and Engineering Aspects,* vol. 558, pp. 242-249, 2018/12/05/ 2018, doi: https://doi.org/10.1016/j.colsurfa.2018.08.058.

[108] A. Momeni and M. J. Filiaggi, *Langmuir,* vol. 30, no. 18, pp. 5256-5266, 2014.

[109] R. Irani and C. Callis, *The Journal of Physical Chemistry,* vol. 64, no. 10, pp. 1398-1407, 1960.

[110] B. Wu, J. Wan, Y. Zhang, B. Pan, and I. M. Lo, *Environmental science & technology,* vol. 54, no. 1, pp. 50-66, 2019.

[111] C. Schwartz and C. Munter, *Industrial & Engineering Chemistry,* vol. 34, no. 1, pp. 32-40, 1942.

[112] T. P. J. Linsinger, *TrAC Trends in Analytical Chemistry,* vol. 27, no. 10, pp. 916-923, 2008/11/01/ 2008, doi: https://doi.org/10.1016/j.trac.2008.08.013.

[113] S. S. Nielsen, *Food analysis*. Springer, 1998.

[114] A. W. Boorn and R. F. Browner, *Analytical Chemistry,* vol. 54, no. 8, pp. 1402-1410, 1982.

[115] J.-L. Todolí and J.-M. Mermet, *Spectrochimica Acta Part B: Atomic Spectroscopy,* vol. 54, no. 6, pp. 895-929, 1999.

[116] D. Hradil and J. Hostomský, *Catena,* vol. 49, no. 1-2, pp. 171-181, 2002.

[117] W. Polzer and J. Hem, *Journal of Geophysical Research,* vol. 70, no. 24, pp. 6233-6240, 1965.

[118] H. M. May, D. Kinniburgh, P. A. Helmke, and M. Jackson, *Geochimica et Cosmochimica Acta,* vol. 50, no. 8, pp. 1667-1677, 1986.

[119] D. F. Franco *et al.*, *Journal of Sol-Gel Science and Technology,* vol. 94, no. 3, pp. 531-543, 2020.

[120] R. D. Irani and C. F. Callis, *Journal of the American Oil Chemists Society,* vol. 39, no. 3, pp. 156-159, 1962.

[121] L. Karni and M. Avron, *Plant and cell physiology,* vol. 29, no. 8, pp. 1311-1314, 1988.

[122] J. J. Christ, S. Willbold, and L. M. Blank, ed: ACS Publications, 2020.

[123] C. Chang and G. Racz, *Canadian Journal of Soil Science,* vol. 57, no. 3, pp. 271-278, 1977.

[124] J. P. Crowther and A. Westman, *Canadian Journal of Chemistry,* vol. 32, no. 1, pp. 42-48, 1954.

[125] D. Canadell, S. Bru, J. Clotet, and J. Ariño, *Bio-protocol,* vol. 6, no. 14, pp. e1874-e1874, 2016.

[126] R. E. Grim, *Science,* vol. 135, no. 3507, pp. 890-898, 1962.

[127] M. Tschapek, L. Tcheichvili, and C. Wasowski, *Clay Minerals,* vol. 10, no. 4, pp. 219-229, 1974.

[128] P. O'Day, G. Parks, and G. Brown, *Clays and Clay Minerals - CLAYS CLAY MINER,* vol. 42, pp. 337-355, 06/01 1994, doi: 10.1346/CCMN.1994.0420312.

[129] R. C. Walton, K. N. White, F. Livens, and C. R. McCrohan, *Biometals,* vol. 23, no. 2, pp. 221-230, 2010.

[130] S. A. Carroll-Webb and J. V. Walther, *Geochimica et Cosmochimica Acta,* vol. 52, no. 11, pp. 2609-2623, 1988.

[131] E. Wieland and W. Stumm, *Geochimica et Cosmochimica Acta,* vol. 56, no. 9, pp. 3339-3355, 1992.

[132] G. Furrer and W. Stumm, *Geochimica et Cosmochimica Acta,* vol. 50, no. 9, pp. 1847-1860, 1986.

[133] G. A. Parks, "Aqueous Surface Chemistry of Oxides and Complex Oxide Minerals," in *Equilibrium Concepts in Natural Water Systems*, vol. 67, (Advances in Chemistry, no. 67): AMERICAN CHEMICAL SOCIETY, 1967, ch. 6, pp. 121-160.

[134] M. D. Bolland, A. M. Posner, and J. P. Quirk, *Clays and Clay minerals,* vol. 28, no. 6, pp. 412-418, 1980.

[135] D. Egirani, M. T. Latif, N. Wessey, N. R. Poyi, and S. Acharjee, *Applied Water Science,* vol. 9, no. 4, pp. 1-10, 2019.

[136] T. Zuyi and C. Taiwei, *Adsorption Science & Technology,* vol. 21, no. 6, pp. 607-616, 2003.

[137] H. Xu, B. Allard, and A. Grimvall, *Water, Air, and Soil Pollution,* vol. 40, no. 3, pp. 293-305, 1988.

[138] N. Fiol and I. Villaescusa, *Environmental chemistry letters,* vol. 7, no. 1, pp. 79-84, 2009.

[139] Z. Zhou and W. Gunter, "The Nature of the Surface Charge on Kaolinite: Constraint of Surface Charge Density," in *Clay Minerals Society 28th Annual Meeting*, 1991, vol. 773, p. 183.

[140] K. Khawmee, A. Suddhiprakarn, I. Kheoruenromne, and B. Singh, *Geoderma,* vol. 192, pp. 120-131, 2013/01/01/ 2013, doi: https://doi.org/10.1016/j.geoderma.2012.07.010.

[141] Y.-h. Hu, H. Jiang, and D.-z. Wang, *Minerals Engineering,* vol. 16, no. 11, pp. 1221-1223, 2003.

[142] J. Singh, P. Huang, U. Hammer, and W. Liaw, *Clays and Clay Minerals,* vol. 44, no. 1, pp. 41-48, 1996.

[143] E. Rosenbrand, I. L. Fabricius, and H. Yuan, "Thermally induced permeability reduction due to particle migration in sandstones: the effect of temperature on kaolinite mobilisation

and aggregation," in *Proceedings of the Thirty-Seventh Workshop on Geothermal Reservoir Engineering*, 2012.

[144] E. Tombácz and M. Szekeres, *Applied Clay Science,* vol. 34, no. 1-4, pp. 105-124, 2006.

[145] C.-P. Huang and W. Stumm, *Journal of Colloid and Interface Science,* vol. 43, no. 2, pp. 409-420, 1973.

[146] Y. A. Lainer, I. Gorichev, A. Tuzhilin, and E. Gololobova, *Russian Metallurgy (Metally),* vol. 2008, no. 4, pp. 294-300, 2008.

[147] E. Wieland, B. Wehrli, and W. Stumm, *Geochimica et Cosmochimica Acta,* vol. 52, no. 8, pp. 1969-1981, 1988.

[148] S. Qiu *et al.*, *Colloids and Surfaces A: Physicochemical and Engineering Aspects,* vol. 642, p. 128596, 2022.

[149] M. Li, J. Liu, Y. Xu, and G. Qian, *Environmental Reviews,* vol. 24, no. 3, pp. 319-332, 2016.

[150] U. P. Strauss and T. L. Treitler, *Journal of the American Chemical Society,* vol. 78, no. 15, pp. 3553-3557, 1956.

[151] E. C. de Oliveira Lima, J. M. Moita Neto, F. Y. Fujiwara, and F. Galembeck, *Journal of Colloid and Interface Science,* vol. 176, no. 2, pp. 388-396, 1995/12/15/ 1995, doi: https://doi.org/10.1006/jcis.1995.9953.

[152] K. Gayer, L. Thompson, and O. Zajicek, *Canadian Journal of Chemistry,* vol. 36, no. 9, pp. 1268-1271, 1958.

[153] A. Michaels, *Industrial & Engineering Chemistry,* vol. 50, no. 6, pp. 951-958, 1958.

[154] Y. I. Tarasevich and G. Klimova, *Applied Clay Science,* vol. 19, no. 1-6, pp. 95-101, 2001.

[155] J. Bidwell, W. Jepson, and G. Toms, *Clay Minerals,* vol. 8, no. 4, pp. 445-459, 1970.

[156] J. Lyons, *Journal of Colloid Science,* vol. 19, no. 5, pp. 399-412, 1964.

[157] J. Yuan, W. L. Garforth, and R. J. Pruett, *Applied Clay Science,* vol. 13, no. 2, pp. 137-147, 1998.

[158] F. Andreola, E. Castellini, T. Manfredini, and M. Romagnoli, *Journal of the European Ceramic society,* vol. 24, no. 7, pp. 2113-2124, 2004.

[159] N. Y. Acelas, B. D. Martin, D. López, and B. Jefferson, *Chemosphere,* vol. 119, pp. 1353-1360, 2015.

[160] R. C. Ropp, "Chapter 5 - Group 14 (C, Si, Ge, Sn, and Pb) Alkaline Earth Compounds," in *Encyclopedia of the Alkaline Earth Compounds*, R. C. Ropp Ed. Amsterdam: Elsevier, 2013, pp. 351-480.

[161] G. B. Alexander, W. Heston, and R. K. Iler, *The Journal of Physical Chemistry,* vol. 58, no. 6, pp. 453-455, 1954.

[162] E. Jackson, *Hydrometallurgical extraction and reclamation*. Ellis Horwood, 1986.

[163] M. Zlokarnik, *Stirring: Theory and practice*. John Wiley & Sons, 2008.

[164] K. Kakaei, M. D. Esrafili, and A. Ehsani, *Graphene surfaces: particles and catalysts*. Academic Press, 2018.

[165] N. Iwashita, C. R. Park, H. Fujimoto, M. Shiraishi, and M. Inagaki, *Carbon,* vol. 42, no. 4, pp. 701-714, 2004.

[166] A. J. Simpson, M. J. Simpson, and R. Soong, *Environmental Science & Technology,* vol. 46, no. 21, pp. 11488-11496, 2012/11/06 2012, doi: 10.1021/es302154w.

[167] F. A. Bovey, P. A. Mirau, and H. Gutowsky, *Nuclear magnetic resonance spectroscopy*. Elsevier, 1988.

[168] J. MacDonald and M. Mazurek, *Journal of Magnetic Resonance (1969),* vol. 72, no. 1, pp. 48-60, 1987.

[169] R. KAKEHASHI and T. MIYAJIMA, *Phosphorus Research Bulletin,* vol. 3, pp. 43-48, 1993.

[170] L. Montagne, G. Palavit, and M. Draoui, *Journal of non-crystalline solids,* vol. 155, no. 2, pp. 115-121, 1993.

[171] J. W. Akitt, N. Greenwood, and G. Lester, *Journal of the Chemical Society A: Inorganic, Physical, Theoretical,* pp. 2450-2457, 1971.

12 Appendices

Appendix A: One-Way ANOVA Results of Section 3.6.2.1

ANOVA

Source of Variation	*SS*	*df*	*MS*	*F*	*P-value*	*F crit*
Between Groups	104.5009056	5	20.90018111	70.30073642	6.5037E-21	2.408514119
Within Groups	14.27024444	48	0.297296759			
Total	118.77115	53				
Total	118.77115	53				

Appendix A 1. One-way ANOVA leaching results at 20 °C, 95% confidence interval

Appendix B: Two-Way ANOVA Results of Section 3.6.2.1

Fe

ANOVA

Source of Variation	*SS*	*df*	*MS*	*F*	*P-value*	*F crit*
Sample	3543.203	1	3543.203	138.3061	2.5E-06	5.317655
Columns	417.956	1	417.956	16.31458	0.00374	5.317655
Interaction	380.3628	1	380.3628	14.84715	0.004855	5.317655
Within	204.9485	8	25.61857			
Total	4546.471	11				

Si

ANOVA

Source of Variation	*SS*	*df*	*MS*	*F*	*P-value*	*F crit*
Sample	1440.363	1	1440.363408	266.2114014	2.00451E-07	5.317655072
Columns	32.96768	1	32.967675	6.093164344	0.038805105	5.317655072
Interaction	36.78501	1	36.78500833	6.798692998	0.03125484	5.317655072
Within	43.2848	8	5.4106			
Total	1553.401	11				

Al

ANOVA

Source of Variation	*SS*	*df*	*MS*	*F*	*P-value*	*F crit*
Sample	2852.392	1	2852.392	103.6986	7.41E-06	5.317655
Columns	321.0571	1	321.0571	11.67202	0.009136	5.317655
Interaction	300.9007	1	300.9007	10.93924	0.010739	5.317655
Within	220.0524	8	27.50655			
Total	3694.402	11				

Ca

ANOVA

Source of Variation	*SS*	*df*	*MS*	*F*	*P-value*	*F crit*
Sample	0.1323	1	0.1323	0.380884	0.554285	5.317655
Columns	1.104133333	1	1.104133333	3.178734	0.112452	5.317655
Interaction	3.808133333	1	3.808133333	10.96339	0.010681	5.317655
Within	2.7788	8	0.34735			
Total	7.823366667	11				

Na

ANOVA

Source of Variation	*SS*	*df*	*MS*	*F*	*P-value*	*F crit*
Sample	0.091875	1	0.091875	2.543839	0.149392	5.317655
Columns	0.238008	1	0.238008	6.589986	0.033278	5.317655
Interaction	0.238008	1	0.238008	6.589986	0.033278	5.317655
Within	0.288933	8	0.036117			
Total	0.856825	11				

K

ANOVA

Source of Variation	*SS*	*df*	*MS*	*F*	*P-value*	*F crit*
Sample	0.935208	1	0.935208	87.74433	1.38E-05	5.317655
Columns	0.003675	1	0.003675	0.344801	0.573266	5.317655
Interaction	0.039675	1	0.039675	3.722439	0.089809	5.317655
Within	0.085267	8	0.010658			
Total	1.063825	11				

Appendix B 1. Two-way ANOVA results of leaching results with temperature and concentration varying. 95% confidence interval

Appendix C: Pairwise Tukey Results of Section 3.6.2.1

Fe

Phosphoric acid Conc. (mol/L)	N	Mean	Grouping
1.0	3	2.5333	A
0.5	3	1.9900	B
0.1	3	1.0033	C

Si

Phosphoric acid Conc. (mol/L)	N	Mean	Grouping
0.5	3	0.8233	A
1.0	3	0.6367	B
0.1	3	0.2100	C

Al

Phosphoric acid Conc. (mol/L)	N	Mean	Grouping
1.0	3	2.4700	A
0.5	3	2.1400	B
0.1	3	1.4233	C

Ca

Phosphoric acid Conc. (mol/L)	N	Mean	Grouping
0.5	3	5.533	A
0.1	3	4.297	A B
1.0	3	3.800	B

Na

Phosphoric acid Conc. (mol/L)	N	Mean	Grouping
0.5	3	2.007	A
1.0	3	1.4433	B
0.1	3	1.3600	B

K

Phosphoric acid Conc. (mol/L)	N	Mean	Grouping
0.1	3	0.2933	A
0.5	3	0.2433	A
1.0	3	0.16333	B

Appendix C 1. Pairwise Tukey results of one-way ANOVA for all impurities at 95% confidence level (leaching at 20 °C)

Fe

Temp_Fe*Conc_Fe	N	Mean	Grouping
100 1	3	48.1600	A
20 1	3	25.0967	B
100 0.5	3	3.7233	C
20 0.5	3	2.5333	C
100 0.1	3	1.9900	C
20 0.1	3	1.0033	C

Si

'Temp_Si'*'Conc._Si'	N	Mean	Grouping
100 1	3	26.0500	A
100 0.5	3	19.2333	B
100 0.1	3	6.3633	C
20 0.5	3	0.8233	D
20 1	3	0.6367	D
20 0.1	3	0.2100	D

Al

Temp_Al*Conc_Al	N	Mean	Grouping
100 1	3	43.3200	A
20 1	3	22.9600	B
100 0.5	3	6.9433	C
20 0.5	3	2.4700	C
100 0.1	3	2.1400	C
20 0.1	3	1.4233	C

Ca

Temp_Ca*Conc_Ca	N	Mean	Grouping
100 0.1	3	5.53333	A
100 1	3	5.13667	A
20 1	3	4.61667	A
100 0.5	3	4.60000	A
20 0.1	3	4.29667	A
20 0.5	3	3.80000	A

Na

Temp_Na*Conc_Na	N	Mean	Grouping
100 0.1	3	2.00667	A
20 1	3	1.92333	A
100 1	3	1.90000	A
20 0.5	3	1.44333	B
20 0.1	3	1.36000	B
100 0.5	3	1.29000	B

K

Temp_K*Conc_K	N	Mean	Grouping
100 1	3	0.836667	A
20 1	3	0.686667	A
100 0.5	3	0.380000	B
20 0.1	3	0.293333	B
100 0.1	3	0.243333	B
20 0.5	3	0.163333	B

Appendix C 2. Pairwise Tukey Results of Two-way ANOVA for interactions (temperature vs concentration) at 95% confidence level

Appendix D: One-Way ANOVA Results of Section 3.6.2.3

ANOVA

Source of Variation	*SS*	*df*	*MS*	*F*	*P-value*	*F crit*
Between Groups	60.0428	5	12.00856	13.66157	2.66893E-08	2.408514119
Within Groups	42.19213333	48	0.879003			
Total	102.2349333	53				

Appendix D 1. One-way ANOVA leaching results of 0.1 M lixiviants (H_3PO_4, PyroP, and PolyP), 95% confidence interval

Appendix E: Two-Way ANOVA Results of Section 3.6.2.3

Fe

ANOVA

Source of Variation	*SS*	*df*	*MS*	*F*	*P-value*	*F crit*
Sample	2.253333333	1	2.253333	80.93385	1.85869E-05	5.317655072
Columns	1.4283	1	1.4283	51.30081	9.59118E-05	5.317655072
Interaction	0.790533333	1	0.790533	28.39389	0.000703721	5.317655072
Within	0.222733333	8	0.027842			
Total	4.6949	11				

Si

ANOVA

Source of Variation	*SS*	*df*	*MS*	*F*	*P-value*	*F crit*
Sample	8.036033333	1	8.036033	23.73253	0.001237	5.317655072
Columns	64.12563333	1	64.12563	189.38	7.5E-07	5.317655072
Interaction	1.068033333	1	1.068033	3.154185	0.113641	5.317655072
Within	2.708866667	8	0.338608			
Total	75.93856667	11				

Al

ANOVA

Source of Variation	*SS*	*df*	*MS*	*F*	*P-value*	*F crit*
Sample	3.445408	1	3.445408	339.1706	7.78E-08	5.317655
Columns	0.205408	1	0.205408	20.22067	0.002011	5.317655
Interaction	0.078408	1	0.078408	7.718622	0.02399	5.317655
Within	0.081267	8	0.010158			
Total	3.810492	11				

Ca

ANOVA

Source of Variation	*SS*	*df*	*MS*	*F*	*P-value*	*F crit*
Sample	0.853333	1	0.853333	39.2638	0.000241	5.317655072
Columns	0.070533	1	0.070533	3.245399	0.109302	5.317655072
Interaction	0.124033	1	0.124033	5.707055	0.043928	5.317655072
Within	0.173867	8	0.021733			
Total	1.221767	11				

K

ANOVA

Source of Variation	*SS*	*df*	*MS*	*F*	*P-value*	*F crit*
Sample	0.021675	1	0.021675	3.25125	0.109031	5.317655072
Columns	0.081675	1	0.081675	12.25125	0.008077	5.317655072
Interaction	0.007008	1	0.007008	1.05125	0.33522	5.317655072
Within	0.053333	8	0.006667			
Total	0.163692	11				

Appendix E 1. Two-way ANOVA leaching results of 0.1 M lixiviants (H_3PO_4, pyroP, and polyP) and varying temperature (20 °C & 100 °C), 95% confidence interval

Appendix F: Pairwise Tukey Results of Section 3.6.2.3

Si

Solution Label	N	Mean	Grouping		
0.1 M PyroP	3	3.733	A		
0.1 M H3PO4	3	0.2100		B	
0.1 M PolyP	3	-0.2933		B	

Al

Solution Label	N	Mean	Grouping		
0.1 M H3PO4	3	1.4233	A		
0.1 M PolyP	3	0.4433		B	
0.1 M PyroP	3	0.3433		B	

Fe

Solution Label	N	Mean	Grouping		
0.1 M H3PO4	3	1.0033	A		
0.1 M PolyP	3	0.2600		B	
0.1 M PyroP	3	0.0833			C

Ca

Solution Label	N	Mean	Grouping		
0.1 M H3PO4	3	4.297	A		
0.1 M PolyP	3	3.1433		B	
0.1 M PyroP	3	2.7867		B	

K

Solution Label	N	Mean	Grouping	
0.1 M PyroP	3	0.7133	A	
0.1 M PolyP	3	0.5000	A	B
0.1 M H3PO4	3	0.2933		B

Appendix F 1. Pairwise tukey results of one-way ANOVA for 0.1 M lixiviants (H_3PO_4, PyroP, and PolyP) at 95% confidence level (leaching at 20 ˚C)

Si

Temperature*Lixiviant type	N	Mean	Grouping			
100 1	3	6.36333	A			
100 2	3	5.96667	A			
20 2	3	3.73333		B		
100 3	3	0.74667			C	
20 1	3	0.21000			C	
20 3	3	-0.29333			C	

Al

Temperature*Lixiviant type	N	Mean	Grouping			
100 1	3	6.94333	A			
100 3	3	1.67667		B		
20 1	3	1.42333		B	C	
100 2	3	1.25333			C	
20 3	3	0.44333				D
20 2	3	0.34333				D

Fe

Temperature*Lixiviant type	N	Mean	Grouping			
100 1	3	3.72333	A			
100 3	3	1.64000		B		
20 1	3	1.00333			C	
100 2	3	0.43667				D
20 3	3	0.26000				D
20 2	3	0.08333				D

Ca

Temperature*Lixiviant type	N	Mean	Grouping		
100 1	3	4.60000	A		
20 1	3	4.29667	A	B	
100 2	3	3.52333	A	B	
100 3	3	3.47333	A	B	
20 3	3	3.14333	A	B	
20 2	3	2.78667		B	

K

Temperature*Lixiviant type	N	Mean	Grouping			
100 2	3	0.750000	A			
20 2	3	0.713333	A			
100 3	3	0.633333	A	B		
20 3	3	0.500000		B	C	
100 1	3	0.380000			C	D
20 1	3	0.293333				D

Appendix F 2. Pairwise Tukey results of two-way ANOVA for 0.1 M lixiviants (H_3PO_4, pyroP and polyP) at 95% confidence level (leaching at 20 ˚C and 100 ˚C)

Appendix G: Raw Data for Section 3.7

Appendix G 1. Pregnant solutions of graphite leaching done at 20 °C analyzed by MP - AES

Leaching temperature: 20 °C						
Sample	Quantity of impurities in 12 mL of pregnant solution (mg)					
	Si	Al	Ca	Fe	Na	K
RO/DI water (control)	0.0	0.0	0.1	0.0	0.0	0.0
H_3PO_4 (1.0 M)	0.0	0.1	0.2	0.2	0.1	0.0
H_3PO_4 (0.1 M)	0.0	0.1	0.3	0.1	0.1	0.0
PyroP (0.1M)	0.2	0.0	0.2	0.0	N/A	0.0
Poly P (0.1 M)	0.0	0.0	0.2	0.0	N/A	0.0

Appendix G 2. Pregnant leaching solutions of graphite leaching done 100 oC analyzed by MP - AES

Leaching temperature: 100 °C						
Sample	Quantity of impurities in 12 mL of pregnant solution (mg)					
	Si	Al	Ca	Fe	Na	K
RO/DI water (control)	0.0	0.0	0.1	0.0	0.1	0.0
H_3PO_4 (1.0 M)	1.6	2.6	0.3	2.9	0.1	0.1
H_3PO_4 (0.1 M)	0.4	0.4	0.3	0.2	0.1	0.0
Pyrophosphate (0.1 M)	0.4	0.1	0.2	0.0	N/A	0.0
Polyphosphate (0.1 M)	0.0	0.1	0.2	0.1	N/A	0.0

Appendix H: Raw Data for Section 3.7

Appendix H 1. Extracted impurity (wt%) from 20 °C leaching

Sample	Extracted impurity (wt%)					
	Si	Al	Ca	Fe	Na	K
RO/DI water (control)	0.0	0.0	33.6	0.00	64.3	0.2
H_3PO_4 (1.0 M)	0.3	1.1	112.9	2.7	144.3	0.5
H_3PO_4 (0.1 M)	0.1	0.6	128.9	1.1	81.6	0.9
pyrophosphate (0.1 M)	1.5	0.1	82.8	0.1	N/A	2.1
polyphosphate (0.1 M $NaPO_3$)	0.0	0.2	93.4	0.3	N/A	1.5

Appendix H 2. Extracted impurity (wt%) from 100 °C leaching

Sample	Extracted impurity (wt%)					
	Si	Al	Ca	Fe	Na	K
RO/DI water (control)	0.0	0.0	37.0	0.0	117.3	0.3
H_3PO_4 (1.0 M)	10.6	18.6	152.6	51.5	190.0	2.5
H_3PO_4 (0.1 M)	2.6	3.0	138.0	4.0	77.4	1.1
pyrophosphate (0.1 M)	2.4	0.5	104.7	0.5	N/A	2.2
polyphosphate (0.1 M $NaPO_3$)	0.3	0.7	103.2	1.8	N/A	1.9

Appendix I: Raw Data for Section 4.7.1.4

Appendix I 1. Summary of impurity concentrations with no digestion

polyp concentration (g/L)	Si (ppm) 251.611 nm	Ca (ppm) 396.847 nm	Fe (ppm) 385.991 nm	Al (ppm) 396.152 nm	K (ppm) 769.897 nm
50 (unspiked)	5.5	29.5	5.5	9.5	3.9
100 (unspiked)	4.7	22.9	5.2	9.5	6.3
200 (unspiked)	3.3	21.6	5.9	11.9	14.2
250 (unspiked)	3	20.8	5.4	10.8	13.9
50 (20 ppm spiked)	23.9	44.3	21.6	26.5	17.5
100 (20 ppm spiked)	21.5	36.2	23.1	26.7	22.3
200 (20 ppm spiked)	14.8	34.2	24.8	29.1	33.4
250 (20 ppm spiked)	13.2	34.6	25.1	29.4	37

Appendix I 2. Spiking recovery rate of the impurity concentrations with no digestion

Si (ppm) 251.611 nm	Ca (ppm) 396.847 nm	Fe (ppm) 385.991 nm	Al (ppm) 396.152 nm	K (ppm) 769.897 nm
92	74	80.5	85	68
84	66.5	89.5	86	80
57.5	63	94.5	86	96
51	69	98.5	93	115.5

Appendix I 3. Summary of impurity concentrations with digestion for an hour

polyp concentration (g/L)	Si (ppm) 251.611 nm	Ca (ppm) 396.847 nm	Fe (ppm) 385.991 nm	Al (ppm) 396.152 nm	K (ppm) 769.897 nm
50 (unspiked)	9.2	36	11.9	16.2	6.7
100 (unspiked)	8.4	30.5	9.3	13.4	9.6
200 (unspiked)	3.5	33	12.1	17.8	21.2
250 (unspiked)	2.7	22.8	11.1	15.9	21.5
50 (spiked 20 ppm)	28.3	49.1	28.1	30.6	21.4
100 (spiked 20 ppm)	24.6	43.6	27.1	31	25.9
200 (spiked 20 ppm)	14.3	41.8	31.1	35.6	41.4
250 (spiked 20 ppm)	11.4	34.8	30.4	34.7	45.4

Appendix I 4. Spiking recovery rate of the impurity concentrations with digestion for an hour

Si (ppm) 251.611 nm	Ca (ppm) 396.847 nm	Fe (ppm) 385.991 nm	Al (ppm) 396.152 nm	K (ppm) 769.897 nm
95.5	65.5	81	72	73.5
81	65.5	89	88	81.5
54	44	95	89	101
43.5	60	96.5	94	119.5

Appendix J: Raw Data for Section 4.7.1.4

Appendix J 1. A) Measured impurity concentrations in the PLS from leached graphite concentrate without digestion. The matrix of the samples contains polyphosphate and 1 M phosphoric acid. B) Measured impurity concentrations in the PLS from leached graphite concentrate after PLS digestion. The matrix of the samples contains polyphosphate and 1 M phosphoric acid. C) Measured impurity concentrations in the PLS from leached graphite concentrate from Chapter 3 liquid to solid ratio 6:1 (v:w), room temperature, 180 minutes. No digestion was performed for this experiment. All samples were diluted with 2% v/v HNO_3

A

polyp concentration (g/L)	Si (ppm) 250.690 nm	Si (ppm) 251.611 nm	Si (ppm) 288.158 nm	Ca (ppm) 393.366 nm	Ca (ppm) 396.847 nm	Ca (ppm) 422.673 nm	Fe (ppm) 371.993 nm	Fe (ppm) 373.486 nm	Fe (ppm) 385.991 nm	Al (ppm) 309.271 nm	Al (ppm) 394.401 nm	Al (ppm) 396.152 nm	K (ppm) 766.491 nm	K (ppm) 769.897 nm
50 (unspiked)	4.6	5.5	5.6	Uncal	29.5	Uncal	5.9	5.2	5.5	9.1	9.4	9.5	Uncal	3.9
100 (unspiked)	3.7	4.7	4.5	Uncal	22.9	Uncal	5.3	4.6	5.2	8.6	9.5	9.5	Uncal	6.3
200 (unspiked)	1.8	3.3	2.9	Uncal	21.6	Uncal	5.1	4.9	5.9	9.7	11.8	11.9	Uncal	14.2
250 (unspiked)	1.5	3	2.5	Uncal	20.8	Uncal	4.8	4.6	5.4	8.8	10.6	10.8	Uncal	13.9
50 (20 ppm spiked)	23.5	23.9	23.9	Uncal	44.3	Uncal	22	21.4	21.6	26.6	25.7	26.5	Uncal	17.5
100 (20 ppm spiked)	20.7	21.5	21	Uncal	36.2	Uncal	23.9	22.8	23.1	25.7	26.1	26.7	Uncal	22.3
200 (20 ppm spiked)	13.6	14.8	14.3	Uncal	34.2	Uncal	22.2	23	24.8	26.8	29.5	29.1	Uncal	33.4
250 (20 ppm spiked)	11.6	13.2	12.6	Uncal	34.6	Uncal	21.7	23.6	25.1	27.5	29.9	29.4	Uncal	37

B

polyp concentration (g/L)	Si (ppm) 250.690 nm	Si (ppm) 251.611 nm	Si (ppm) 288.158 nm	Ca (ppm) 393.366 nm	Ca (ppm) 396.847 nm	Ca (ppm) 422.673 nm	Fe (ppm) 371.993 nm	Fe (ppm) 373.486 nm	Fe (ppm) 385.991 nm	Al (ppm) 309.271 nm	Al (ppm) 394.401 nm	Al (ppm) 396.152 nm	K (ppm) 766.491 nm	K (ppm) 769.897 nm
50 (unspiked)	8.1	9.2	9	Uncal	36	Uncal	12.4	11.6	11.9	15.4	16	16.2	Uncal	6.7
100 (unspiked)	7.3	8.4	8	Uncal	30.5	Uncal	9.4	8.9	9.3	12	13.4	13.4	Uncal	9.6
200 (unspiked)	1.7	3.5	3.2	Uncal	33	Uncal	9.4	10.8	12.1	14.8	17.2	17.8	Uncal	21.2
250 (unspiked)	0.9	2.7	2.2	Uncal	22.8	Uncal	8.3	9.8	11.1	13.3	15.9	15.9	Uncal	21.5
50 (spiked 20 ppm)	27.7	28.3	28.2	Uncal	49.1	Uncal	28.6	28.2	28.1	30.2	30.3	30.6	Uncal	21.4
100 (spiked 20 ppm)	23.8	24.6	24.2	Uncal	43.6	Uncal	27.7	27.3	27.1	29.8	30.3	31	Uncal	25.9
200 (spiked 20 ppm)	12.5	14.3	13.6	Uncal	41.8	Uncal	25.9	29.3	31.1	32.5	35.5	35.6	Uncal	41.4
250 (spiked 20 ppm)	9	11.4	10.5	Uncal	34.8	Uncal	24.2	28.7	30.4	31.5	34.8	34.7	Uncal	45.4

C

Solution Label	Si (ppm) 250.690 nm	Si (ppm) 251.611 nm	Si (ppm) 288.158 nm	Ca (ppm) 393.366 nm	Ca (ppm) 396.847 nm	Ca (ppm) 422.673 nm	Fe (ppm) 371.993 nm	Fe (ppm) 373.486 nm	Fe (ppm) 385.991 nm	Al (ppm) 309.271 nm	Al (ppm) 394.401 nm	Al (ppm) 396.152 nm	K (ppm) 766.491 nm	K (ppm) 769.897 nm
polyp (0.1 M) + RO water (repeat #1)	17.5	16.4	15.5	30.9	21	31.6	1.7	1.1	1.5	1.7	2.3	Uncal	4.3	4.1
polyp (0.1 M) + RO water (repeat #2)	17.8	16.7	15.8	30.8	20.4	30.4	2.2	1.6	1.8	1.6	2.2	Uncal	3.7	3.5
H3PO4 (1 M) (repeat #1)	22.3	21.8	20.9	31.9	29.9	29.4	15.3	15.1	14.5	13.8	13.8	Uncal	1.9	1.9
H3PO4 (1 M) (repeat #2)	22.6	22	21.1	25.6	22.9	23	14.3	13.8	13.2	12.6	13.2	Uncal	1.5	1.4

Appendix K: Raw Data Points of Section 6.4.2.

Appendix K 3. Measured concentrations of extracted impurities after two-step leaching. First step (_1) and second step (_2)

Solution Label	Si (ppm) 251.611 nm	Fe (ppm) 371.993 nm	Al (ppm) 396.152 nm
Al_Si_1	0.56	3.29	5.32
Al_Si_1	0.42	2.54	4.10
Al_Si_1	0.42	2.65	4.29
Si_Al_1	1.55	1.75	1.56
Si_Al_1	1.10	1.92	1.71
Si_Al_1	1.10	1.87	1.60
Al_Si_2	0.54	0.01	0.22
Al_Si_2	0.48	0.01	0.18
Al_Si_2	0.44	0.01	0.22
Si_Al_2	0.41	0.40	2.24
Si_Al_2	0.39	0.36	2.33
Si_Al_2	0.40	0.36	2.29

Appendix K 4. Average impurity extraction percentages of the two different prioritization cases

Extracted amount On average:			
Solution Label	Si (ppm) 251.611 nm	Fe (ppm) 371.993 nm	Al (ppm) 396.152 nm
Al_Si_1	0.47	2.83	4.57
Si_Al_1	1.25	1.85	1.62
Al_Si_2	0.49	0.01	0.20
Si_Al_2	0.40	0.37	2.29

Appendix K 5. Relative standard deviation calculated for the average impurity extraction percentages.

Extracted amount relative std-dev:			
Solution Label	Si (ppm) 251.611 nm	Fe (ppm) 371.993 nm	Al (ppm) 396.152 nm
Al_Si_1	14.14	11.66	11.76
Si_Al_1	16.92	3.82	3.87
Al_Si_2	8.35	17.68	9.75
Si_Al_2	1.43	4.92	1.63

*The relative standard deviation was calculated by multiplying the standard deviation by 100 then dividing the product by the average